UNIVERSIDADE DO ESTADO DE SANTA CATARINA
CENTRO DE CIÊNCIAS TECNOLÓGICAS
DEPARTAMENTO DE ENGENHARIA ELÉTRICA
PÓS-GRADUAÇÃO EM ENGENHARIA ELÉTRICA

KAUE FELIPE MORCELLES

# REAL-TIME MONITORING DEVICE FOR 4D BIOPRINTING BASED ON ELECTRICAL IMPEDANCE TOMOGRAPHY

JOINVILLE

2021

**KAUE FELIPE MORCELLES**

# REAL-TIME MONITORING DEVICE FOR 4D BIOPRINTING BASED ON ELECTRICAL IMPEDANCE TOMOGRAPHY

Dissertação submetida ao Curso de Pós-Graduação em Engenharia Elétrica, do Centro de Ciências Tecnológicas da Universidade do Estado de Santa Catarina, para a obtenção do Grau de Mestre em Engenharia Elétrica.

**Orientador**: Prof. Dr. Pedro Bertemes Filho

**JOINVILLE**

**2021**

**Ficha catalográfica elaborada pelo programa de geração automática da**

**Biblioteca Setorial do CCT/UDESC,**

**com os dados fornecidos pelo(a) autor(a)**

Morcelles, Kaue Felipe
Real-Time Monitoring Device For 4d Bioprinting Based On Electrical Impedance Tomography / Kaue Felipe Morcelles. -- 2022.
129 p.

Orientador: Pedro Bertemes Filho
Dissertação (mestrado) -- Universidade do Estado de Santa Catarina, Centro de Ciências Tecnológicas, Programa de Pós-Graduação em Engenharia Elétrica, Joinville, 2022.

1. bioimpressão 4D,. 2. EIT. 3. bioengenharia. 4. bioimpedância. I. Bertemes Filho, Pedro. II. Universidade do Estado de Santa Catarina, Centro de Ciências Tecnológicas, Programa de Pós-Graduação em Engenharia Elétrica. III. Título.

# AGRADECIMENTOS

Agradeço à minha família, em especial meus pais Alessandro e Viviane e minha namorada Daiane, por todo o apoio, compreensão e amor. Aos meus amigos por todos os bons momentos que tornaram esta trajetória mais leve. Ao professor Pedro Bertemes pela orientação e apoio, essenciais para esta dissertação. Ao professor Frederico Ferreira, pelo estágio que foi o pontapé inicial para idealizaçao deste trabalho. Agradeço também ao professor Abel Candido Recco pelo acesso à máquina de *sputtering*, ao professor David Marcondes pelo auxílio na confecção de placas e peças, ao Tiago Vignola pelo auxílio no laboratório de química, e à UDESC pela infraestrutura e recursos. Por fim, agradeço à banca e ao leitor pela atenção e tempo dedicados na leitura deste trabalho.

*The attraction and drawback of EIT is that it doesn't clearly work, so we can reap the fruits of its images, or not work, so we can change direction; it usually almost works, which is an incitement to redouble our efforts (Dr. David Holder)*

# ABSTRACT

Human tissue bioprinting is one of the most exciting fields in tissue engineering and regenerative medicine. It consists in the automatic manufacture of three-dimensional biological structures, which can then be applied in patient specific tissue replacement, drug development and more reliable *in vitro* biological models. One limitation of tissue bioprinting is the lack of non-destructive, real-time and remote methods to monitor the evolution of cells and tissue during the maturation process. This thesis describes the development of a non-invasive and remote sensor to evaluate bioprinted tissue evolution in real-time using EIT. The prototype consists of an electrode sensor, an analog front-end and a digital unit. The electrode sensor is made of 16 gold-surface signal electrodes arranged in a circular configuration, with a ground electrode at the center, and a polypropylene cylinder fixed around the array to act as a culture well. The analog front-end is composed of three stages: the commutation module, the excitation circuit and the voltage sensor circuit. The commutation module is based on the AD75019 cross-point switch, allowing arbitrary selection of electrodes for excitation and sensing via serial control. The excitation circuit consists of a Differential Howland Current Source with a transconductance of 150 $\mu S$, optimized for low output common-mode operation. The source operates with square-wave signals at 10 and 100 kHz. The voltage sensing circuit is composed of two input buffers, a differential VGA and a fourth-order antialiasing filter, based on the differential multiple-feedback topology. The sensing circuit provides selectable gain from 0 to 80 dB with cut-off frequency of 1 MHz. The STM32F303ZE microcontroller was the core of the digital unit, providing analog-to-digital conversion, gain control, channel selection, data preprocessing and communication with the host via UART protocol. To validate the prototype, EIT experiments were performed with biological and bioprinted phantoms. Carrots and apples were used as primary biological materials, and a saline solution with 1.5 S/m was used as background media. A dedicated bioprinter was develop to print the hydrogel phantoms, using an alginate-gelatin bioink. To collect the boundary voltages, the adjacent measurement protocol was used, with injection currents of approximately 310 $\mu A$ at 10 and 100 kHz. Both TDEIT and FDEIT were tested. A MATLAB interface was developed to control the prototype and reconstruct the images, using the Iterative Total Variation Regularization algorithm. Both interface and reconstruction algorithms were developed on top of the EIDORS library. The proposed system was capable of reconstructing the EIT images for all the phantom structures. From the TDEIT images, information about the position, size and orientation of the phantom could be obtained. Moreover, it was possible to differentiate the biological tissue from the bioprinted hydrogel structure using FDEIT, which is fundamental to track the cell growth inside the scaffold. However, the use of a 2D EIT limited the performance of the device, resulting in poor shape identification capabilities, and the use of static vegetable phantoms is not optimal to represent tissue growth *in vitro*. Therefore, future works will focus on developing 3D EIT algorithms and testing the device with bioprinted human tissue.

**Keywords:** 4D bioprinting, EIT, bioengineering, bioimpedance

# RESUMO

A bioimpressão de tecidos consiste na fabricação automática de estruturas biológicas tridimensionais com células humanas, que podem ser aplicadas na regeneração de tecidos, desenvolvimento de medicamentos e modelos biológicos *in vitro* mais confiáveis. Uma das limitações da bioimpressão é a falta de métodos de sensoriamento remoto, não-invasivos e em tempo real, para monitorar a evolução dos tecidos. Este trabalho propõe um dispositivo para monitoramento não-invasivo da evolução do tecido bioimpresso em tempo real, utilizando tomografia por impedância elétrica (TIE). O protótipo consiste em uma matriz de eletrodos, uma *interface* analógica e um módulo digital. A matriz de eletrodos é composta por 16 eletrodos de ouro dispostos em uma configuração circular, e um eletrodo central de aterramento. Um cilindro de polipropileno foi fixado ao redor da matriz, para atuar como um poço de cultura. A interface analógica é composta pelo módulo de comutação, pelo circuito de excitação e pelo circuito medidor de tensão. O módulo de comutação é baseado no integrado AD75019, permitindo a seleção arbitrária de eletrodos. O circuito de excitação consiste em uma fonte de corrente Howland diferencial com transcondutância de 150 $\mu S$, otimizada para redução de modo-comum. A fonte opera com sinais de onda quadrada de 10 e 100 kHz. O circuito de detecção de tensão é composto por dois *buffers* na entrada, um amplificador diferencial com ganho controlado e um filtro *anti-aliasing* de quarta ordem, baseado na topologia de realimentação múltipla diferencial. O circuito de detecção fornece ganho selecionável de 0 a 80 dB, com frequência de corte de 1 MHz. O microcontrolador STM32F303ZE foi utilizado como módulo digital, fornecendo conversão analógico-digital, controle de ganho, seleção de canal, pré-processamento de dados e comunicação com o computador via UART. Para validação do protótipo, experimentos de TIE foram realizados com fantomas biológicos e bioimpressos. Cenouras e maçãs foram usadas como materiais biológicos primários, e uma solução salina com 1,5 S/m foi utilizada para representar o meio de cultura. Uma bioimpressora foi desenvolvida para imprimir os fantomas de hidrogel, utilizando uma biotinta de alginato e gelatina. Para coletar as tensões ao redor da amostra, o protocolo de medição adjacente foi utilizado, com correntes de injeção de aproximadamente 310 $\mu A$ em 10 e 100 kHz. TIE por diferença no tempo (TIE-DT) e TIE por diferença na frequência (TIE-DF) foram utilizadas. Uma interface foi desenvolvida em MATLAB para controlar o protótipo e reconstruir as imagens, utilizando o algoritmo de Regularização Iterativa de Variação Total. Ambos os algoritmos de interface e reconstrução foram desenvolvidos com a biblioteca EIDORS. O sistema proposto foi capaz de reconstruir as imagens de TIE para todos os fantomas. A partir das imagens TIE-DT, foram obtidas informações sobre a posição, tamanho e orientação do objeto testado. Além disso, foi possível diferenciar o tecido biológico da estrutura do hidrogel bioimpresso utilizando TIE-DF, o que é fundamental para acompanhar o crescimento celular dentro do *scaffold*. No entanto, a utilização de métodos 2D limitou o desempenho do dispositivo em termos de recontrução de forma. Além disso, o uso de fantomas vegetais não é ideal para representar o crescimento de tecidos *in vitro*. Portanto, trabalhos futuros visarão o desenvolvimento de algoritmos TIE 3D e testes com tecido humano bioimpresso.

**Palavras-chave:** bioimpressão 4D, EIT, bioengenharia, bioimpedância

## LIST OF FIGURES

# LIST OF ABBREVIATIONS

| | |
|---|---|
| EIT | Electrical Impedance Tomography |
| AV | Additive Manufacturing |
| CT | Computed Tomography |
| MR | Magnetic Resonance |
| CAD | Computer-Aided Design |
| CNC | Computer Numeric Control |
| RE | Robotic Extrusion |
| IJ | Ink-Jet |
| LAP | Laser Assisted Printing |
| CE | Cell Electrospinning |
| UV | Ultraviolet |
| ECM | Extracelular Matrix |
| CEM | Complete Electrode Model |
| FP | Forward Problem |
| IP | Inverse Problem |
| PLA | Polylactic Acid |
| RepRap | Replicating Rapid prototyper |
| w/w | weight/weight proportion |
| FFT | Fast Fourier Transform |
| FEM | Finite Elements Model |
| BIA | Bioimpedance Analysis |
| CMRR | Common-Mode Rejection Ratio |
| ADC | analog-to-digital converter |

| | |
|---|---|
| VGA | Variable Gain Amplifier |
| FET | Field Effect Transistor |
| DAC | Digital-to-Analog Converter |
| IC | Integrated Circuit |
| FFC | Flat Flexible Cables |
| EMI | Electromagnetic Interference |
| TDEIT | Time-Difference Electrical Impedance Tomography |
| FDEIT | Frequency-Difference Electrical Impedance Tomography |
| MCU | Microcontroller Unit |
| DMA | Direct Memory Access |
| PWM | Pulse Width Modulation |
| UART | Universal Asynchrounous Receiver/Transmite |
| USB | Universal Serial Bus |
| IDE | Integrated Development Environment |
| SM | State Machine |
| CPU | Central Processing Unit |
| SRAM | Static Random Acess Memory |
| CSV | Comma-Separated Values |
| ABS | Acrylonitrile Butadiene Styrene |
| PWL | Piece-Wise Linear |
| PSD | Power Spectrum Density |
| fps | frames-per-second |

# CONTENTS

# 1 INTRODUCTION

Tissue bioprinting is the most proeminent method of biofabrication. It applies the additive manufacturing techniques from conventional 3D printers to tissue engineering (MOROUÇO, 2017). In 3D bioprinting, the cells are placed automatically in predetermined locations, forming a multi-layer cell construct that can be designed to function as a tissue. Hydrogels are used to carry the cells during the printing process and to provide mechanical stability during maturation, acting as a scaffold (DABABNEH; OZBOLAT, 2014; MOROUÇO, 2017). The fabricated tissue can then be applied in several biomedical applications, such as biological models, stem cell manufacturing and differentiation, tissue engineering for regenerative medicine and bio-syncretic robots (KALLOS; SEN; BEHIE, 2003; HELGASON; MILLER, 2005; FRESHNEY, 2005; CANALI et al., 2015). Although 3D bioprinting provides a high level of control and flexibility over cell position and tissue structure, it does not consider the control and conditions necessary for proper tissue maturation. In this scenario, the "4D bioprinting" term emerged. This technique considers time as the fourth printing dimension, where control takes place in the form of automated and dedicated bioreactors (GAO et al., 2016). These bioreactors can act in several different ways, including media replacement, mechanical and electrical stimulation, inoculation of biological factors and drug delivery (HELGASON; MILLER, 2005; DARLING; ATHANASIOU, 2003; JIMBO; KAWANA, 1992). Each process should happen at specific periods of the maturation, and failing to provide the correct action at the correct time may result in an unexpected outcome. Therefore, it is crucial to monitor the tissue evolution in real-time.

Cell cultures can be either 2D or 3D (HAYCOCK, 2011), and bioprinted tissues *in vitro* fall into the three-dimensional category. The literature suggests several culture evaluation protocols to obtain important information about the culture, such as cell adhesion, viability and proliferation (HELGASON; MILLER, 2005). For instance, LIVE/DEAD assessments can measure cell viability using fluorescent dyes; immunohistochemistry applies antigen staining to identify abnormal cells (BUCHWALOW; BÖCKER, 2010); and hemocytomers and flow cytometers are applied in cell counting (HAUGLAND; MACCOUBREY; MOORE, 1994; ABSHER, 1973). However, conventional protocols are typically invasive and destructive to the culture, which results in the end of the experiment and extra laboratory work (RISS et al., 2016). Moreover, most assessment protocols are designed to operate with cell monolayers, which are not compatible with three-dimensional structures. For instance, the light penetration of optical microscopy techniques are limited to a few micrometers (PAMPALONI; REYNAUD;

STELZER, 2007). Therefore, there is a lack of non-invasive, real-time and automatic monitoring techniques optimized for 3D structures, which are fundamental in 4D bioprinting.

Moreover, due to the complex nature of bioprinted constructs, monitoring techniques should also provide spatial information about the culture. Therefore, biochemical sensors, such as Bio-FETs (POGHOSSIAN et al., 2009; CURTO et al., 2017) are not enough to obtain the complete state of the tissue, because it cannot observe the spatial distribution of processes inside the culture (LEÓN; PUPOVAC; MCARTHUR, 2020). To obtain spatial-wise information, imaging techniques are required, which can infer internal properties of the tissue from the boundary information with sufficient spatial resolution. Electrical Impedance Tomography (EIT) is an imaging technique able to generate 2D and 3D images of the sample's electrical conductivity distribution (HOLDER, 2004; MARTINSEN; GRIMNES, 2011). The method consists of exciting the object with a current and reconstructing the internal conductivity distribution using the boundary voltages, that are measured through multiple electrodes (BAYFORD, 2006).

EIT-based imaging can be applied in industrial processes (WANG et al., 2016; HALLAJI; SEPPÄNEN; POUR-GHAZ, 2014) and biomedical applications, such as brain function monitoring, lung ventilation and gesture recognition (ARISTOVICH et al., 2016; PULLETZ et al., 2012). Compared to other imaging methods, such as X-ray and magnetic resonance, EIT has the advantages of being portable, less costly, non-invasive, safer, easily automated, fast and providing high throughput (BAYFORD, 2006; LIONHEART, 2004; MARTINSEN; GRIMNES, 2011). However, image reconstruction is a severely ill-posed problem, which makes it difficult to obtain unique and stable solutions from noisy measurements (SEO et al., 2008; BAYFORD, 2006; MUELLER; SILTANEN; ISAACSON, 2002; JIN; KHAN; MAASS, 2012). Moreover, low spatial resolution and electrode contact problems are major drawbacks that limit the applicability range of the technology. Although EIT is often applied in the centimeters/meters range, microscopic EIT is also possible, being firstly demonstrated by Griffiths *et al* (GRIFFITHS et al., 1996) and York *et al* (YORK et al., 2004).

The application of bioimpedance in cell culture assessment is not new: Giaever and Keese proposed a system to monitor cells using the electrical impedance measured via bipolar gold electrodes at the bottom of culture wells (GIAEVER; KEESE, 1986). This measurement can be used to evaluate cell proliferation, viability, toxicity, barrier function and differentiation (GIAEVER; KEESE, 1986; XIAO; LUONG, 2003; SZULCEK; BOGAARD; AMERONGEN, 2014; ANGSTMANN et al., 2011; ALEXANDER; PRICE; BHANSALI, 2012). However, bioimpedance measurements are limited in terms of spatial resolution. EIT combines the advantages of bioimpedance with image reconstruction (LINDERHOLM et al., 2007). The electrical conductivity distribution can be correlated with the biological state of the culture because the electrical properties of cells are significantly different from the background media, creating a contrast in the EIT image that depends on the frequency (MARTINSEN; GRIMNES, 2011; BERTEMES-FILHO, 2002). Compared to conventional cell culture protocols, EIT provides portability, lower cost, automated functionality and non-invasive/non-destructive real-time operation (WU, 2020).

In this thesis, a miniature EIT system to monitor bioprinted tissue is proposed. Initially, two literature reviews about 4D bioprinting and EIT were presented, covering the basic concepts, main paradigms and limitations of each technology. The following section discuss the materials and methods used in this work, which includes the description of a dedicated bioprinter developed for system validation, the development tools implemented and the simulation and experimental setups. Section 5 describes the proposed system in detail, including analog front-end, digital unit, firmware, measurement protocol and electrode sensor. Sections 6 and 7 presents simulation and experimental results, respectively, including circuit characterization, bioprinted structures, EIT images of biological phantoms and an integrated simulation framework developed in this thesis.

## 1.1 GENERAL OBJECTIVE

Development of non-invasive, real-time and remote sensor to monitor the evolution of bioprinted tissue using electrical impedance tomography imaging.

## 1.2 SPECIFIC OBJECTIVES

- Design, simulation and implementation of the required hardware, including analog front-end, digital unit and electrode array;
- Development of a firmware for the STM32F303ZE microcontroller, to provide signal generation, gain and channel selection, host communication and interface with the user;
- Development of a MATLAB script for board control and image reconstruction;
- Test and validation of the EIT device using biological and bioprinted phantoms.

# 2 4D BIOPRINTING

4D Bioprinting is an additive manufacturing (AM) technique used to produce living tissue structures able to mimic the biological behavior of its natural counterparts *in vivo*. It implements layer-by-layer construct techniques derived from traditional 3D printing to precisely dispense cell-laden biomaterials, forming structures with controlled geometry (MOROUÇO, 2017). Biological tissues need a period of maturation before application, and therefore "4D" stands for the control of the three spatial dimensions (x, y, z) and time (GAO et al., 2016).

This chapter presents the basic concepts of 4D bioprinting, discussing the image preprocessing steps and main printing paradigms, biomaterials implemented in the literature and technological limitations that still require solution.

## 2.1 IMAGE PREPROCESSING

In order to correctly mimic the biological behaviour *in vivo*, bioprinted constructs should have geometric structure similar to the target tissue or organ. Therefore, the printing process is typically based on an image of its target (PATI; GANTELIUS; SVAHN, 2016; MURPHY; ATALA, 2014). Imaging can be performed by traditional medical methods, such as computed tomography (CT) and magnetic resonance (MR) (MURPHY; ATALA, 2014; PATRA; YOUNG, 2016). This allows personalization of the printed tissue, which is essential in regenerative medicine.

Imaging methods store cross-sectional images (slices) of the organ (MURPHY; ATALA, 2014). The slices of data are then transformed in a 3D surface model of the tissue, using automated CAD tools (MIRONOV; KASYANOV; MARKWALD, 2011; MURPHY; ATALA, 2014). The 3D model can then be further manipulate in post-processing, to simplify the manufacturing process or to exclude unnecessary parts. Before building the tissue, the 3D model must be converted into a sequence of commands that the machine is able to understand. In this step, a slicer software is applied to generate cross-sectional slices of the 3D surface model (MURPHY; ATALA, 2014). Each slice represents a layer to be printed. A tool-path algorithm then calculates the best sequence of movements to be performed by the dispensing head. Finally, the slices, tool-path and predefined printing configurations (such as speed and temperature) are converted into a motion schedule, which is a series of commands that are sent to the bioprinter during the manufacturing process. The language of the commands is usually G-CODE, with machine-specific adaptations that depends on printer type and brand (GOLDSTEIN et al., 2016).

## 2.2 BIOPRINTING PARADIGMS

Both commercial and prototype bioprinters generally consist of three main components: a three-axial positioning system, a material reservoir and a dispensing unit. The first is responsible for controlling the position of the dispenser, and it is implemented using mechanical systems actuated by stepper motors. Cartesian positioning machines (typical in CNCs and 3D printers) are the most commonly implemented in bioprinters, but other architectures from traditional 3D printing may be used, such as the delta configuration. The positioning mechanism usually does not depend on the printing paradigm.

The material reservoir stores the cells and biomaterials to be printed and controls the environment conditions (temperature, humidity, pressure) needed for cell viability and material printability. This component also delivers the material to the dispenser in a controlled way. Although its implementation can vary in some paradigms, such as Laser-Assisted Bioprinting and Stereolithography, it is generally applied using a syringe pump.

The dispensing unit receives the material from the reservoir and released it in a controlled way to the substrate where the part is being printed. This stage have a drastic impact on fundamental bioprinting properties, such as resolution, cell viability, speed, structural and mechanical properties, biomaterial availability and cost effectiveness (MURPHY; ATALA, 2014; PATRA; YOUNG, 2016). Therefore, machines with different dispenser types have different outcomes and target applications. Bioprinting paradigms are then defined as the type of technology implemented in the dispensing unit. Figure 2.1 shows the different bioprinting techniques presented in the literature.

Figure 2.1 – The main bioprinting paradigms.

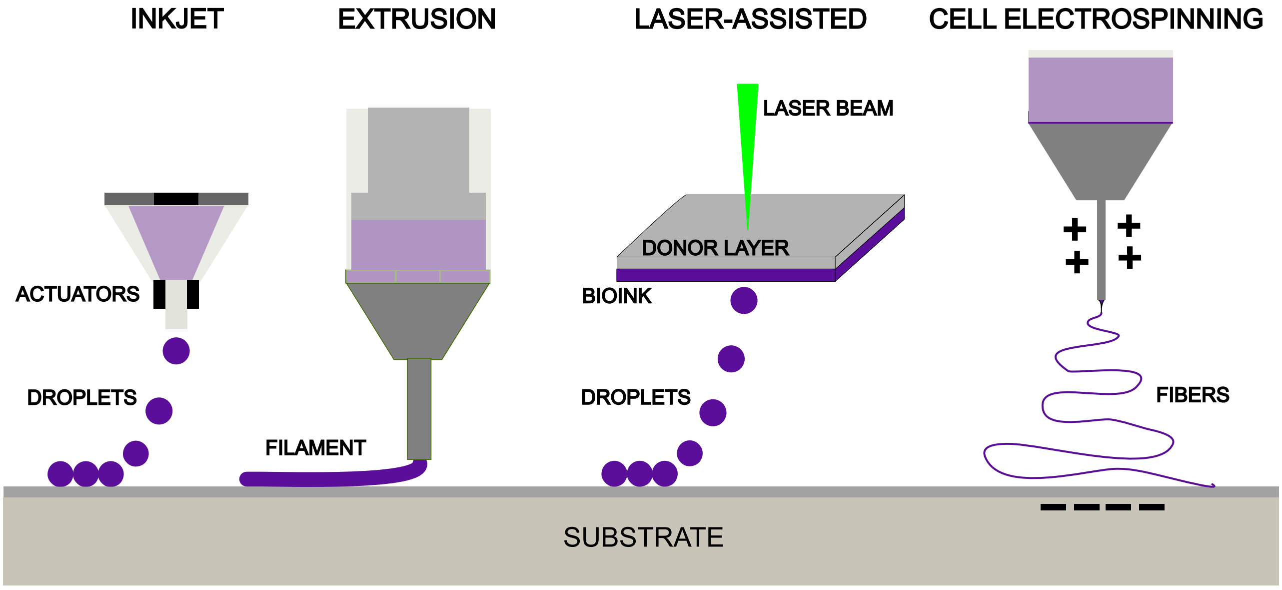

Source: Produced by the Author, 2021.

### 2.2.1 Robotic Extrusion

Robotic Extrusion (RE) is a printing technique that consists on the deposition of viscous biomaterials continuously using a mechanical extruder (HONG et al., 2018; HINTON et al., 2015). This paradigm is similar to the Fused Deposition Modelling (FDM), which is commonly used in domestic 3D printers, where the printing process occurs in two steps: 1) a previously liquid or viscous biomaterial is dispensed layer-by-layer on a plate and 2) the biomaterial is cured to obtain mechanical stability (PATRA; YOUNG, 2016). Step 1 is executed by a nozzle with direct contact with the surface, and multiple heads can be used to print different materials. Step 2 consists in the gelation of the biomaterial, which can be performed by temperature, chemicals or light exposure. Different from most methods, which are droplet based, extrusion delivers a continuous string of material (GILLISPIE et al., 2019), increasing mechanical stability and geometric fidelity.

The extrusion system is composed by a needle nozzle, a syringe and an actuation system to push the material out of the nozzle. There are three types of RE nozzles: pneumatic, screw-driven and piston-driven extruders (CHOUDHURY; ANAND; NAING, 2018; GAO et al., 2016). Pneumatic extruders use gas pressure to push the material out of the nozzle, thus needing only an external compressed air system. The velocity and force of the extrusion can be set using Bernoulli principles, and high viscous biomaterials can be applied (GILLISPIE et al., 2019). The system, however, produces significant hysteresis and lacks retraction capabilities, making it difficult to control the volume of material (DU, 2018). Screw and piston-driven extrusion are more reliable in terms of dispensing control, usually using stepper motors to set the velocity and direction of dispensing. However, the mechanical parts of these systems are more complex (thus prone to malfunctions) and produce lower forces (HONG et al., 2018; GILLISPIE et al., 2019).

The biomaterials implemented in this technique are usually hydrogels embedded with cells, and the cross-linking process can be achieved using temperature (e.g. Matrigel), chemicals (e.g. sodium alginate, collagen) or light (e.g. gelatin-methacryloyl) (GOPINATHAN; NOH, 2018). However, RE can bioprint a wide range of materials, with viscosity ranging from 30 mPa/s to $6x10^7$ mPa/s and embedded with high cell densities. The main limitation of RE nozzles biological applications is the trade-off between resolution and cell viability: the higher the resolution, smaller is the nozzle and, therefore, bigger the shear stress applied to the cells (HONG et al., 2018; DU, 2018). Excessive stress can lead to cell death during the printing process, reducing cell viability. Thus, the maximum resolution is usually limited to 5 - 200 $\mu m$. Moreover, RE bioprinters have limited speed of 10 - 50 $\mu m/s$ (GILLISPIE et al., 2019). Dispensing pressure is more significant to cell viability than the nozzle size, therefore the extruder must be designed and calibrated carefully to avoid cell damage (MOROUÇO, 2017).

### 2.2.2 Inkjet Bioprinting

Inspired by Ink-Jet (IJ) conventional printers, this paradigm was the first one implemented in bioprinting. It consists of a header able to release droplets of biomaterial in a controlled path, layer-by-layer and without contact with the printing surface (MATTIMORE et al., 2010). There are two main mechanisms implemented in this paradigm. The first one uses a heater to locally elevate the temperature of the liquid biomaterial to the point of gasification, forming a bubble with a pressure that overcomes the surface tension at the tip of the nozzle, releasing a droplet of material with controllable size and dispensing rate (GUDAPATI; DEY; OZBOLAT, 2016). One limitation of this approach is that excessive heat needed to form the bubble may increase the cell mortality (HONG et al., 2018). To prevent this issue, a piezoelectric actuator can be used instead, generating pressure mechanically (HONG et al., 2018; GUDAPATI; DEY; OZBOLAT, 2016). However, as the heating pulse generated by the printing head (between 200 and 300 ºC) is typically very short in time (around 2 $\mu s$), the increase in hydrogel temperature is kept below 10 ºC (MURPHY; ATALA, 2014).

Independent of the droplet generating method employed, the basic principle is the same: generate a controlled stream of drops to form layers of biological tissue. To properly create these droplets and avoid clogging, the biomaterial viscosity and cell density cannot be too high, reducing the range of applications (DU, 2018; MATTIMORE et al., 2010). Moreover, low viscosity biomaterials have low mechanical stability, weakening the final structure and degrading geometric fidelity (HONG et al., 2018). On the other hand, IJ systems provide high levels of control over the volume of printed material, by releasing only a predetermined amount of bioink per droplet (MATTIMORE et al., 2010; TEKIN; SMITH; SCHUBERT, 2008; VANDERBURGH et al., 2017). Besides, being able to regulate the size of the droplets allows allows the creation of concentration gradients of cells, which is required in some applications (HONG et al., 2018).

Another advantage of IJ bioprinters is the low manufacturing cost and easy implementation, and can be built on top of conventional paper printers (XU et al., 2005). It also provides high-throughput capability, as multiple cell lines and materials can be easily implemented in a single printing head, with drop-rates as high as 10000 drops/s and drop volumes lower than 1 pL (PATI; GANTELIUS; SVAHN, 2016; DEMIRCI; MONTESANO, 2007).

### 2.2.3 Laser Assisted Bioprinting

Similar to the IJ bioprinting paradigm, Laser Assisted Printing (LAP) delivers a stream of droplets to form the tissue (KERIQUEL et al., 2017; GUILLOTIN et al., 2010). However, the process is so distinct that it is referred as a different paradigm. Instead of thermal or mechanical actuation, LAP uses a high-power laser beam focused on a thin sheet of liquid biomaterial to eject a droplet in a determined position (KERIQUEL et al., 2017; GUILLOTIN et al., 2010). The LAP working mechanism is composed of two main layers: a donor layer and a biomaterial thin sheet (DU, 2018). The liquid (or gel) biomaterial is spread at the bottom surface of the donor layer, that is most commonly made of metal (DU, 2018; HONG et al., 2018; GUILLOTIN et al., 2010). The top surface of the donor layer is attached to a transparent support plate, which provides mechanical foundation without blocking the laser light. The high-power laser beam hits the top surface of the absorbing layer, which converts the luminous energy into local pressure due to partial evaporation of the metal (HONG et al., 2018). This local pressure pushes the biomaterial towards the the printing surface, forming the layers. The donor layer also acts as a shield between the laser and biological material (PATI; GANTELIUS; SVAHN, 2016).

The size of the biomaterial droplets is highly dependent on the laser beam, and very high resolution can be obtained by simply focusing the beam to a smaller area (DU, 2018). Successful single cell droplets have been reported (GILLISPIE et al., 2019). Also, being a nozzle-free technique, the paradigm is immune to clogging issues and can be used with high viscosity bioinks (300 mpA/s) and cell densities ($10^8$ cells/mL) (GILLISPIE et al., 2019). Another advantage is its high cell viability, typically between 90 to 98% (KOCH et al., 2010).

The main limitations of the paradigm are the high manufacturing cost and low throughput, due to the slow process of preparing the ribbon each time a new cell or biomaterial needs to be printed (MURPHY; ATALA, 2014). Besides, the printing process is very dependent on the physical characteristics of the assembly (such as distance between layers, absorbing layer composition and surface tension of the material) and laser properties, which increases significantly the hardware complexity (HONG et al., 2018).

### 2.2.4 Cell Electrospinning

Electrospinning uses electrostatic forces to eject a thin liquid stream of polymer, and it is usually implemented in fibrous scaffolds (GUO et al., 2019). Cell Electrospinning (CE) is a derivation of this technique, embedding living cells inside the biomaterial and precisely positioning the nozzle head to construct different geometries. The cell-laden liquid polymer is contained inside a reservoir (usually a syringe), and it can be eject to the outside through a coaxial needle tip. The coaxial configurations allows the deliver of cells inside the biomaterial fiber (SAMPSON et al., 2014; HONG et al., 2018). In normal conditions, the liquid would remain inside the reservoir by surface tension (HONG et al., 2018). However, the electrospinning process charges the tip to potentials up to the kilovolts range. As the printing plate is grounded, there is a high electrical field between the needle and the plate, which breaks surface tension and ejects a very thin stream of polymer, that solidifies in the air before hitting the printing surface (SAMPSON et al., 2014).

The advantage of this paradigm is the capability of making structures with high porosity, which facilitates nutrient and water distribution during the maturation state (OZBOLAT; MONCAL; GUDAPATI, 2017). The fibers are usually ejected randomly, but can also be placed in oriented fashion, mimicking anisotropic tissues such as neurons and muscles. Also, the fibers have a cross-sectional area of nanometers, allowing extremely high contact area between material and cells, thus improving cell adhesion and behaviour (SAMPSON et al., 2014). However, the nanometric diameter of the fibers can significantly increase the printing time, and parts with thickness higher than few centimeters are impractical. Thus, this technique is usually used as an auxiliary process to another paradigm, increasing mechanical and/or functional properties of the scaffold (GILLISPIE et al., 2019).

### 2.2.5 Stereolithography

The basis of stereolithography is the creation of solid patterns using photocurable liquid materials and a laser beam or light projector (MOROUÇO, 2017; CHOUDHURY; ANAND; NAING, 2018) . With control of the z-axis, a 3D part can be created layer by layer. If a single laser beam is used, a positioning system must be implemented. However, maximum velocity is achieved using a light projector, which instantly cures the layer. In this case, the light is projected at the bottom of a printing platform covered in liquid material, curing the pattern in place (MOROUÇO, 2017). The main advantages of this technique are the nozzle-free operation, which increases material viscosity and cell density range, and the printing speed, because of the instantaneous layer formation.

Conventional photocurable resins are usually not biocompatible, being toxic to the cells and affecting viability (SAYGILI et al., 2019). Therefore, material selection is more limited than other techniques. However, some photocurable biocompatible hydrogels, such as PEG-DMA and GelMA, have been implemented in the literature (GAUVIN et al., 2012; LU et al., 2006). Another drawbacks of the technique include shrinkage effects after printing, lack of mechanical strength, use of UV light and incompatibility with multimaterial bioprinting (MOROUÇO, 2017).

## 2.3 BIOMATERIALS

The bioinks used in 4D bioprinting are typically composed of cell embedded with biomaterials. The final tissue construct should be composed mainly by cells and extracellular matrix (ECM), however during the printing process the cells are applied in suspension (MURPHY; ATALA, 2014). Therefore, support biomaterials are needed to ensure mechanical and geometrical stability, as well as to create an environment that provides adhesion, growth and proliferation of cells during maturation. Two characteristics that are required are biocompatibility and biodegradability (GOPINATHAN; NOH, 2018; MOBARAKI et al., 2020). The first promotes cell viability and function, and the second ensures that the final structure is composed only by cells and ECM. The main biomaterials used as bioinks can be classified as hydrogels and biodegradable polymers.

### 2.3.1 Hydrogels

The water content of the adult human body is typically 60%, and vital organs such as the heart and lungs can be made up of 73% and 83% water, respectively (MITCHELL et al., 1945). Because of this, materials with large water content are desirable in 3D cell cultures. Hydrogel polymers play a fundamental role in bioprinting, not only because of its high percentage of water, but also due to its biocompatibility, printability and tunable mechanical and biochemical properties (VLIERBERGHE; DUBRUEL; SCHACHT, 2011). Another advantage of hydrogels is the wide variety of gelification mechanisms available, which allows its application in different printing paradigms and techniques. Prior to gelification, the hydrogel can be stored and delivered on its liquid form, carrying the cells in is interior. After the gelification process, which can be done using temperature, chemicals or light, the hydrogel becomes a porous solid with large water content, able to keep a stable structure while still capable of nurturing the cells (VLIERBERGHE; DUBRUEL; SCHACHT, 2011). Figure 2.2 shows the gelification, also called crosslinking, process of alginate-based hydrogels. The crosslinking occurs in the presence of calcium ions, that binds to the alginate chains (LI et al., 2018).

### 2.3.2 Biodegradable Polymers

Biodegradable polymers are defined as any polymeric material that can be decomposed in the presence of biological activity (IQBAL et al., 2019). In the cell culture context, a biodegradable scaffold initially serves as a biocompatible environment, preserving cell growth, adhesion, functionality and mechanical stability, so that the biological part can grow in the

Figure 2.2 – Chemical cross-linking of alginate. Initially, the polymeric chains of alginate are dissolved and disconnected from each other (a). The crosslinking process begins with the addition of calcium ions (b). Each calcium ion can binds to two chains, resulting in a grid that is mechanically stable and can hold large amounts of water (c).

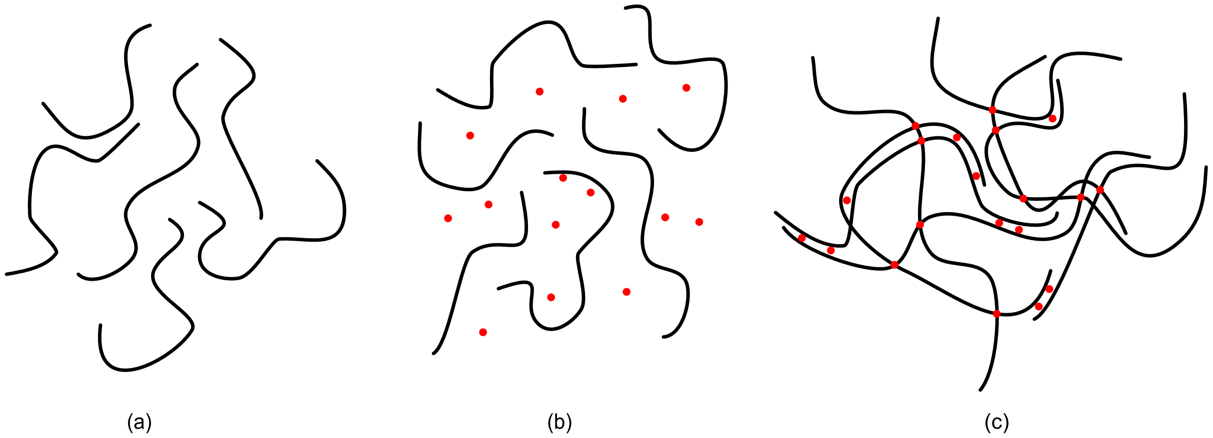

Source: Produced by the Author, 2021.

correct shape. After the degradation period, the polymer is decomposed by water or cell activity, and the extracellular matrix becomes the structural backbone of the part (IQBAL et al., 2019; LEI; WANG, 2016). Biodegradable polymers can be synthetic or natural. Synthetic polymers are easier to synthesize and manipulate, providing more degrees of freedom to tune the mechanical, electrical and chemical properties of the material. Therefore, the printability of synthetic polymers is typically higher than the natural polymers (DONNALOJA et al., 2020; LIU; WANG, 2020). On the other hand, natural polymers are products of the biological activity of living organisms, which makes them significantly more biocompatible than synthetic polymers (DONNALOJA et al., 2020). They provide an environment closer to the actual extracellular matrix, increasing cell viability and functionality. However, their printability is lower because the mechanical properties are more difficult to manipulate. Also, they cannot be directly synthesize in the laboratory, which decreases the availability.

The advantages and limitations of synthetic and natural polymers illustrates one of the most important trade-offs of 4D bioprinting: printability *versus* biocompatibility. When designing a bioink, one should weight the most important aspects of the application, namely (HOSPODIUK et al., 2017; UNAGOLLA; JAYASURIYA, 2020; LEI; WANG, 2016):

- Tissue and cell type, that dictates the type of extracellular matrix to be formed;
- Geometric shape, considering both macroscopic and microscopic structures;
- Mechanical properties, including stability, endurance, elasticity, printability and porosity;
- Degradation rate and the resulting by-products;

- Special features, such as electrical conductivity, drug delivery and magnetic properties;

After carefully examination of the requirements, the designer should define priorities and synthesize the bioink accordingly. One can either select between synthetic and natural polymers, or implement a hybrid material containing both (BELLEGHEM et al., 2020), exploiting the advantages of both types.

## 2.4 LIMITATIONS AND PERSPECTIVES

Although 4D bioprinting has the potential of revolutionizing regenerative medicine, current limitations still prevents its use commercially, particularly for large and complex tissues and organs that contains different cell types and microscopic structures, such as the lungs, liver and heart. This section discuss some of the bottlenecks that must be overcome before moving from *in vitro* models to human applications.

### 2.4.1 Microscopic Scaling

Human tissues are composed by an intricate microscopic morphology, where different cells are organized in a particular shape and structure. One particular example is the lung, where the bronchi structure goes from the macroscopic to the microscopic level, ending on the alveoli (MILLER, 1893). This suggests that a microscopic printing resolution is needed to reproduce the internal lung morphology with all the bronchi and alveoli. However, in 3D printing the printing time grows exponentially with the ratio between part volume and resolution. Considering the macroscopic scale of the whole organ, the printing time becomes unfeasible for living cells if a microscopic resolution is implemented with the available techniques. Therefore, it is difficult to keep cell viability high in large-scale organs with microscopic complexity (MATAI et al., 2020; CORBETT; OLSZEWSKI; STEVENS, 2019). This issue is not limited to lungs. In fact, most organs have complex microscopic morphology, such as the liver, with lobules and acinus, kidney, with nephrons and collecting ducts, and pancreas, with acinus, islets and draining ductiles (POPPER; SCHAFFNER et al., 1957; MOFFAT, 1975; LONGNECKER; GORELICK; THOMPSON, 2018). Self-assembly is an alternate method that can be used in combination with 4D bioprinting to overcome this issue (JAKAB et al., 2010).

### 2.4.2 Vascularization

The scaling problem is also related to another limitation in 4D bioprinting: the lack of vascularization. Vascularization, from main vessels to capillary structures, is responsible for the transportation of fundamental substances to cells, including nutrients, oxygen and toxins (KOLESKY et al., 2016). Therefore, vascularization is fundamental for cell viability in bioprinted structures. However, as discussed in Section 2.2, conventional bioprinting paradigms rely on layer-by-layer deposition of soft hydrogels, which is not optimal for printing small ductile structures (KOLESKY et al., 2016; RICHARDS et al., 2017). Also, capillary networks are microscopically small, conflicting into the scaling limitation discussed previously. Although several possible solutions are presented in the literature (SHAO et al., 2020; KOLESKY et al., 2014; RICHARDS et al., 2017), vascularization remains one of the main technological bottlenecks in 4D bioprinting (GAO et al., 2018).

### 2.4.3 Real-Time Monitoring

Maturation is a fundamental stage of tissue engineering. During this period, cells will grow, adhere to the scaffold, proliferate and begin to develop the actual tissue structure (GAO et al., 2016). In some cases, differentiation and migration of cells also occurs. In order to control the maturation process, as well as obtaining important information of the cell behavior, the 3D culture should be monitored constantly (WU, 2020). Conventional assessment protocols typically require destructive and invasive methods, such as staining, slicing and resuspension. Also, most methods rely on optical microscopy, which is not adequate for 3D constructs, as it cannot penetrate layers deeper than a few micrometers (PAMPALONI; REYNAUD; STELZER, 2007). Figure 2.3 highlights the difference between 2D and 3D culture structure. Therefore, the 4D bioprinting field still lacks a gold-standard, real-time and non-invasive monitoring technique.

Figure 2.3 – 2D cell culture monolayer (a) and 3D cell culture spheroids (b).

(a) (b)

Source: Produced by the Author, 2021.

Near-infrared and visible light sensors can be used to obtain information about the constitution of tissues via the absorption rate of particular wavelengths (WILSON et al.,

2015; CHEONG; PRAHL; WELCH, 1990; SVENSSON et al., 2005). However, light cannot penetrate thick tissues, so the applicability of the technique is limited (PAMPALONI; REYNAUD; STELZER, 2007). Biochemical sensors are also proposed in the literature, using the detection of key substances to indirectly identify the state and activity of the culture (POGHOSSIAN et al., 2009; CURTO et al., 2017). This approach presents two major drawbacks: the sensors are typically disposable, due to the reaction with the detected substances, and they cannot provide spatial-wise information, such as cell distribution and migration.

Spatial-wise information can be obtained using safe and non-invasive imaging techniques. Ultrasound imaging is a popular method, with well known imaging applicability (HUANG; ZENG, 2017), but the difference between the acoustic impedance of single cells and the hydrogel scaffold is too subtle for conventional detectors. The electric impedance, on the other hand, vary significantly. Cells are considered electrical insulators, due to the double-layer membrane, whereas hydrogels embedded in a electrolyte can be considered a conductor, due to the free ions (GRIMNES; MARTINSEN, 2011). Therefore, bioimpedance measurements can be used to detect the presence and density of cells within a hydrogel scaffold. Moreover, bioimpedance can be used to obtain an image of the conductivity through EIT (BAYFORD, 2006; LIONHEART, 2004; GRIMNES; MARTINSEN, 2011). Using the distribution of electrical conductivity within a culture well, one can obtain the spatial distribution of cells, which can then be correlated with cell viability, proliferation and adhesion.

# 3 EIT FOR CELL CULTURES

Electrical Impedance Tomography is a powerful imaging tool, capable of providing an image of the electrical conductivity distribution of a sample in a non-invasive, non-destructive and biocompatible fashion (BAYFORD, 2006). Moreover, EIT can be applied in real-time, continuously analysing tissue during maturation (WU, 2020). EIT devices are also cheaper, smaller and more portable than other imaging techniques, such as CT, MRI, and ultrasound (BAYFORD, 2006; BERA, 2018; WU, 2020). This chapter discusses the principles of bioimpedance and EIT, presents a hardware review focusing on three-dimensional cell cultures and discusses the main technology limitations.

## 3.1 BIOIMPEDANCE: BASIC CONCEPTS

Impedance can be defined as the passive electrical response of a material for a given electrical stimulation. Bioimpedance is the impedance of living things, such as organs, tissues and whole organisms. Therefore, the bioimpedance models passive electrical properties of living tissues, and can be described in terms of conductivity and permittivity (GRIMNES; MARTINSEN, 2011). Because the electrical properties are closely related to the material properties, such as geometry and constitution, the measurement of bioimpedance can be used to infer physical information about the sample. For instance, bioimpedance can be applied in body fat analysis, as the fat percentage of a body segment can be estimated from the dielectric properties of the tissue (LORENZO et al., 1997).

Cell cultures can also be measured using bioimpedance: in this case, the cell membranes behave as electrical insulators, possessing dielectric properties that are well defined in the literature, whereas the background culture media and scaffold act as electrolyte conductors (GRIMNES; MARTINSEN, 2011). Therefore, as the cell culture grows, the value of the impedance of a certain frequency changes, and this can be correlated with tissue properties, such as cell growth, viability and proliferation (GIAEVER; KEESE, 1986). Also, the electric properties are frequency dependent, so measuring in different frequencies provides more information about the constitution of the material (BERTEMES-FILHO, 2002). For instance, the insulating properties of cell membrane prevents low frequency currents to enter the cells, whereas high frequencies are able to pass through (Figure 3.1). Thus, low frequency bioimpedance can be used to infer the ECM content, high frequency data can infer internal properties of cells, and the ratio between both can be used to estimate cell number. Moreover, the electrical permittivity of biological tissues also depends on the frequency, which translates into dielectric dispersion (GRIMNES; MARTINSEN, 2011). The dispersion domains in living tissues ($\alpha$, $\beta$ and $\gamma$) depends on the physical constitution of the sample. Different tissues present different electrical dispersion characteristics, which results in a particular bioimpedance curve in frequency that conveys information about the sample. This technique is called bioimpedance spectroscopy, and can be used to detect differentiation, adhesion, distinguish between tissues, obtain mathematical models of the sample and validate measurements (GRIMNES; MARTINSEN, 2011; GIAEVER; KEESE, 1986; BERTEMES-FILHO, 2002).

Figure 3.1 – Electrical current passing through a cell agglomeration. Frequency $f_1$ is lower than $f_2$.

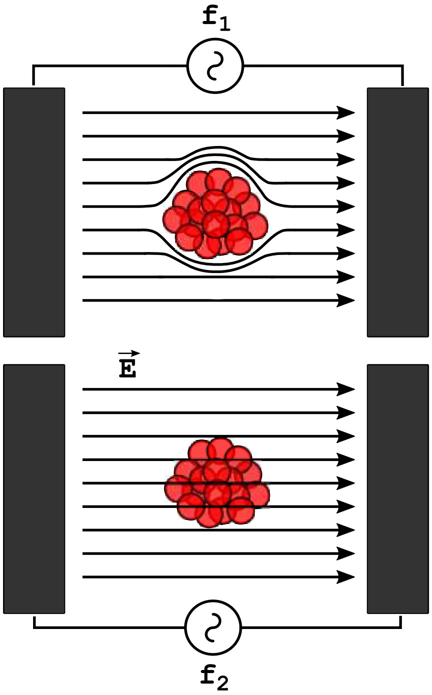

Source: Produced by the Author, 2021.

Bioimpedance is typically measured using three basic circuits: the excitation module, that injects an electrical signal into the sample, the sensing module, that measures the signal response of the tissue, and the processing unit, which controls and process the impedance values. The interface between circuit and tissue is performed through electrodes, that should be designed to provide a low impedance path to the sample while maintaining biocompatibility, sensitivity and stability.

## 3.2 EIT MATHEMATICAL BACKGROUND

The EIT technique consists of placing several electrodes at the boundaries of a sample, exciting a pair of electrodes and measuring the resulting voltage from one or more pairs, with different combinations (HOLDER, 2004; BERA, 2018). For each excitation mode, the conductivity distribution of the sample will affect the potential measured at all the electrode pairs, and the combination of all disturbances can be used to reconstruct an image of the conductivity distribution (HOLDER, 2004; BAYFORD, 2006; BERA, 2018). For instance, by exciting an homogeneous sample containing a conductivity drop at a single point, the disturbance caused in the potential field will have a distribution similar to a dipole. Figure 3.2 shows the basic steps in EIT reconstruction.

Figure 3.2 – The electrical impedance tomography process

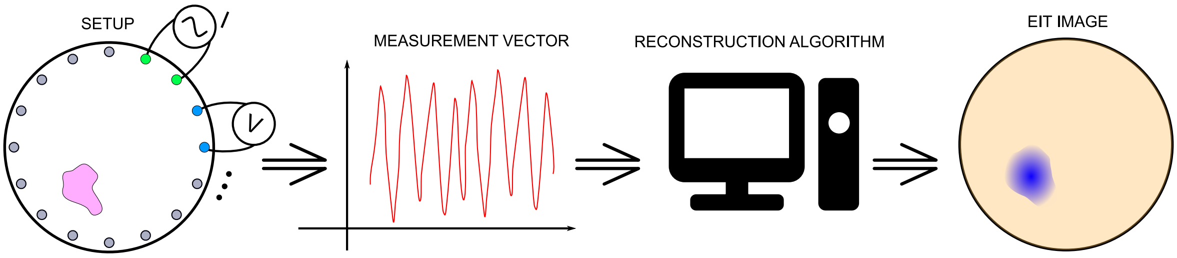

Source: Produced by the Author, 2021.

A mathematical model of the sample combined with an image reconstruction algorithm are required to obtain the conductivity distribution of the sample. In general, the image reconstruction algorithm operates by gradually changing the conductivity distribution of the mathematical model until measurements taken in the model matches the measurements obtained experimentally and *a priori* information (HOLDER, 2004; LIONHEART, 2004). There are several image reconstruction image reconstruction algorithms available, but most of them can be divided into two steps: the forward problem and the inverse problem.

### 3.2.1 Mathematical Formalization

In an EIT measurement, the sample can be defined by a region $\Omega$ and a boundary $\partial\Omega$. The sample have a conductivity distribution $\sigma$, and a potential distribution $\phi$. In this case, the internal potential distribution can be calculated using the modified Laplace equation (HOLDER, 2004):

$$\nabla \cdot \sigma \vec{\nabla} \phi = 0 \tag{3.1}$$

Moreover, current is only injected at the boundaries of the sample. The current density at $\partial\Omega$ can be defined as:

$$j = \sigma \vec{\nabla} \phi \cdot \vec{n} \tag{3.2}$$

Where $\vec{n}$ is the unit normal vector that defines the boundary surface and $-\vec{\nabla}\phi$ is the electrical field. These equations show that the potential $\phi$ can be calculated from both the conductivity distribution $\sigma$ and the current density at the border (HOLDER, 2004). Moreover, a transconductance operator can be defined. This operator maps the potential distribution to the current density at the boundary:

$$\Lambda_\sigma : \phi|_{\partial\Omega} \mapsto j \tag{3.3}$$

The reconstruction process can be formally defined as the calculation of $\sigma$ from the transconductance operator $\Lambda_\sigma$ (HOLDER, 2004). The transcondutance operator $\Lambda_\sigma$ can be measured by injecting a current and measuring the correspondent voltages. However, the EIT problem applies and measures currents only at the electrodes, so $j$ and $\phi|_{\partial\Omega}$ are not completely defined. The actual measurements correspond to a finite set of voltages $\boldsymbol{V}$ and injection currents $\boldsymbol{I}$, and the transconductance operator becomes a transconductance matrix (HOLDER, 2004).

Moreover, the effect of electrode impedance must be considered. The Complete Electrode Model (CEM) is used to account for the voltage drop at the electrode site. The electrode voltage can be calculated using equation 3.4, where $z_{elec}$ is the electrode impedance (HOLDER, 2004).

$$V_{elec} = \phi + z_{elec}\sigma\frac{\partial\phi}{\partial\vec{n}} \tag{3.4}$$

### 3.2.2 The Forward Problem

The forward problem (FP) consists of solving a mathematical model that predicts the potential distribution within the volume at the boundaries from a given conductivity distribution (HOLDER, 2004). Thus, the problem can be defined as (BAYFORD et al., 2001):

$$V = S\sigma \tag{3.5}$$

Where, $\sigma$ is the conductivity distribution, $\boldsymbol{V}$ is the boundary voltage distribution and $\boldsymbol{S}$ is the sensitivity field of the sample. The sensitivity field is the weighted contribution of each conductivity point to the boundary voltage field. Grimnes and Martinsen presented the following equation to calculate the sensitivity field (GRIMNES; MARTINSEN, 2011):

$$S = \vec{J_{reci}} \cdot \vec{J_{CC}} \tag{3.6}$$

In this equation, $\vec{J_{CC}}$ is the normalized injection current density field and $\vec{J_{reci}}$ is the normalized reciprocal current density field (GRIMNES; MARTINSEN, 2011). The reciprocal current is defined as the hypothetical current distribution that would be generated if the pair of measuring electrodes was carrying the current. This means that:

- The sensitivity field depends on both the injection and measuring pair of electrodes;
- The sensitivity field remains unchanged if the excitation and measuring pairs are switched.

The second consequence is the reciprocity property of tetrapolar measurements (GRIMNES; MARTINSEN, 2011), which are used to evaluate the performance of the EIT device using the reciprocity error parameter. The forward problem consists of simply finding the sensitivity matrix for each injection/measurement pair (Equation 3.6) to solve equation 3.5. The injection current density $\vec{J_{CC}}$ and the reciprocal $\vec{J_{reci}}$ can be obtained using equations 3.1, 3.2, 3.4 and the boundary conditions (see (HOLDER, 2004)).

However, analytical methods are difficult to solve and limited to well defined and simple geometries. In real-life applications, numerical methods are applied. The most popular way of solving the FP is by using Finite Element Method (FEM) (LIONHEART, 2004). To each element, a conductivity is assigned, and the electrical potential distribution can be calculated using FEM for every excitation mode. The steps required to solve the Forward Problem are:

1. Define a 3D geometric model of the measurement area;
2. Create a FEM mesh, using finer meshes around the electrodes and near the sample (if the position is known), and coarser meshes at the background region;
3. Implement the Complete Electrode Model (CEM) to estimate the contact impedance of the electrodes;
4. Assemble the system matrix from the FEM model combined with CEM;
5. Calculate the sensitivity matrix for each excitation mode.

There are a huge amount of published work on how to solve the forward problem, such as optimal mesh generation, improve convergence and efficiency improvement and hybrid methods combining FEM with other discretization techniques for faster computation (DANESHMAND; JAFARI, 2013; ALEX; REDDY, 2018; EDMANS; INTES, 2015; LIONHEART, 2004). However, these methods are outside the scope of this work. This thesis will focus on forward solvers based on first order FEM, with a fixed mesh and tetrahedral elements.

### 3.2.3 The Inverse Problem

The inverse problem (IP) is the calculation of the internal conductivities from the boundary measurements (HOLDER, 2004). The most basic method consists in adjust the conductivity distribution until the calculated potentials match the experimental voltages, using least-squares approximation (BAYFORD, 2006). In this case, the minimization is performed over the cost function $f(\sigma)$ in equation 3.7, where $V_{elec}$ is the measured electrode voltage set, $F(\sigma)$ is the correspondent voltage set calculated in the forward problem and $\sigma_{est}$ is the estimated conductivity distribution.

$$f(\sigma_{est}) = ||V_{elec} - F(\sigma_{est})||^2 \tag{3.7}$$

The conductivity distribution can be defined as:

$$\sigma_{est} = argmin_{\sigma}||V_{elec} - F(\sigma)|| \tag{3.8}$$

However, the Inverse Problem is highly ill-posed and non-linear (HOLDER, 2004). This means that the solution is not unique, and small measurement errors in $V_{elec}$ can generate large errors in the conductivity distribution. To stabilize the solution, the problem must be regularized (LIONHEART, 2004).

### 3.2.4 Regularization

Regularization consists in using *a priori* information about the sample as an heuristic tool to obtain the correct solution (LIONHEART, 2004). For instance, one can include penalty functions to avoid solutions with sharp oscillatory behavior, or to provide geometric information about the conductivity distribution that is previously known (HOLDER, 2004; BAYFORD, 2006). Regularization can be implemented by adding a regularizing term $G(\sigma_{est})$ to the cost function.

$$f(\sigma_{est}) = ||V_{elec} - F(\sigma_{est})||^2 + G(\sigma_{est}) \tag{3.9}$$

The function $G(\sigma_{est})$ is a function that calculates a penalty value for a certain $\sigma_{est}$ distribution. This way, the minimization of the cost function will reduce both the quadratic voltage error and the regularization term. Therefore, there is a compromise between fitting the calculated voltages to the measurements and defining the type of solution that are needed (BAYFORD, 2006). Over-fitting the data can lead to large errors due to inaccurate measurements and model representation, whereas over-regularization reduces the range of features that the inverse algorithm is capable to reconstruct (LIONHEART, 2004).

One classic example is the Tikhonov regularization (TIKHONOV, 1963). This method defines $G(\sigma_{est}) = \alpha^2||\sigma||^2$. This allows control over the values of $\sigma$ as well as the least-square minimization. The $\alpha$ term is called regularization parameter, and can control the trade-off between regularization and fitting (HOLDER, 2004).

Another reconstruction algorithm is the Total Variation Regularization (BORSIC et al., 2007). In this case, the regularization term $G$ consists of integral of the conductivity variation (Equation 3.10). This approach prevents results with wild variations, such as oscillatory solutions, while still allowing sharp edges (HOLDER, 2004). The integral term is weighted by the regularization parameter $\alpha$

$$f(\sigma_{est}) = ||V_{elec} - F(\sigma_{est})||^2 + \alpha \int_{\Omega} |\nabla \sigma_{est}| \tag{3.10}$$

In the cell culture context, regularization can be used to specify the scaffold location and shape to the algorithm, as well as the expected fluctuations in conductivity. For instance, one should not expect sharp changes in conductivity outside the boundaries of the scaffold, so solutions containing such features should be avoided. Also, as imaging are performed constantly during cell maturation, the conductivity distribution is correlated in time, thus time-regularization methods can be implemented.

### 3.2.5 Linearization

To solve the inverse problem using conventional numeric methods, the problem is typically linearized. Newton-based algorithms are the conventional approach for system linearization (LIONHEART, 2004). Linearized solutions can provide fast and useful results for small perturbations. In the case of EIT, the function to be linearized is the forward function $F(\sigma)$. The linearized function can be described by Equation 3.11, where $F(\sigma_O)$ defines the initial point and the Jacobian $J(\sigma - \sigma_O)$ is the Jacobian of the forward function applied to the interval $\sigma - \sigma_O$ (HOLDER, 2004).

$$F(\sigma) = F(\sigma_O) + J(\sigma - \sigma_O) \tag{3.11}$$

The linearization error decreases with the interval $\sigma - \sigma_O$, so for a infinitesimal interval perturbation $\delta\sigma$, the error tends to zero. In linearized and iterative problems, the forward problem is solved using the linearized equation (HOLDER, 2004).

One-step reconstruction algorithms combine equations 3.9 and 3.11, and minimizes the result using analytical methods to obtain the linearized Equation 3.12, where $\delta\sigma$ is the conductivity perturbation, $\sigma_{ref}$ is a reference conductivity for regularization and $L$ is a differential operator that performs the regularization (HOLDER, 2004).

$$\delta\sigma = (J^*J + \alpha^2 L^*L)^{-1}(J^*(V_{elec} - F(\sigma_0)) + \alpha^2 L^*L(\sigma_{ref} - \sigma_0)) \tag{3.12}$$

When using this approach, the Jacobian needs to be calculated using the forward model, and then the explicit equation solves the conductivity. Although simple and efficient to implement, the One-step approach is limited to small perturbations, as the linearization error grows quickly with $\sigma - \sigma_O$.

### 3.2.6 Iterative Methods

Iterative methods are broadly applied in numerical calculations of non-linear functions. They can be used to overcome the limitation of the One-Step approach, being able to solve the problem for larger variations of conductivity (LIONHEART, 2004). The iterative method can be described by Equation 3.13 (HOLDER, 2004).

$$\sigma_{n+1} = \sigma_n + ({J_n}^*J_n + \alpha^2 L^*L)^{-1}(J_n(V_{elec} - F(\sigma_n))) + \alpha^2 L^*L(\sigma_{ref} - \sigma_n)) \tag{3.13}$$

In this equation, the conductivity distribution is updated inevery iteration $n$, starting from a seed point $\sigma_0$. In each iteration, the Jacobian $J_n$ and the voltages $F(\sigma_n)$ are re-calculated. The iteration stops after the conductivity update reaches a tolerance or the maximum number of iterations is obtained (HOLDER, 2004).

Because of the iterative nature, these methods can converge to the solution without the large estimation error of *One Step* solutions, even for large differences in conductivity (LIONHEART, 2004; HOLDER, 2004). However, the computation cost is increased significantly, especially in 3D imaging. Therefore, a trade-off must be considered when selecting between *One-step* and iterative approaches.

### 3.2.7 Absolute and Difference EIT

Two of the main paradigms in EIT calculation are the absolute EIT and the difference EIT (HOLDER, 2004). Absolute EIT stands for solving the exact value of the complex conductivity at each point in space. The difference EIT, on the other hand, solves the difference between the conductivity values at two different points in time and/or frequency. The obvious advantage of absolute EIT is that the exact value of conductivity can be directly correlated with material properties of the sample (MARTINS et al., 2019). However, absolute EIT is significantly more difficult and time consuming to implement (BAYFORD, 2006).

Difference imaging, on the other hand, can reduce common-mode systematic errors, which appear in both reference and sample measurements, and can be directly solved using linearized and iterative methods, as the definition of linearization (Equation 3.11) requires a reference point $\sigma_O$. In cell cultures, the conductivity of the background media is known. Therefore, one can calculate the culture absolute conductivity using difference EIT with the background media as the reference image, if the background conductivity remains unchanged. For this reason, this thesis will focus on difference EIT. However, absolute EIT methods for cell cultures should be investigated in future works, especially because in long-term monitoring the background media changes with cell metabolism (WU, 2020).

## 3.3 HARDWARE REVIEW

Due to the ill-posed nature of the problem, the electrical measurements must be extremely precise (HOLDER, 2004). Therefore, the hardware designed to excite the sample and to read the voltage pairs is fundamental for the quality of EIT imaging. The basic EIT hardware can be divided in four modules: the excitation stage, the voltage measurement system, the switching circuit, the electrode array and the logical unit. The hardware review performed during this thesis was published in the journal Review of Scientific Instruments (RSI), named *"Hardware for Cell Culture Electrical Impedance Tomography: a Critical Review"* (MORCELLES; BERTEMES-FILHO, 2021). A copy of the article can be found attached at the end of this document.

## 3.4 TECHNOLOGY LIMITATIONS

As discussed previously, electrical impedance tomography is biocompatible, non-invasive and can be performed in real-time and remotely. All these characteristics make the technology desirable for cell culture imaging applications, especially in bioprinted cultures. However, EIT presents several limitations that should be taken into account before applying it to cultures. Firstly, EIT is limited in terms of spatial resolution (BAYFORD, 2006; HOLDER, 2004). The spatial resolution is tightly linked to the number of electrodes, and increasing the number of electrodes increases exponentially the time required for each image (CANALI et al., 2016). Therefore, the number of electrodes is limited, and so is the spatial resolution. Secondly, different from conventional imaging techniques, the excitation currents do not travel in straight lines, neither are confined in 2D slices of material (LIONHEART, 2004). Instead, the current spreads through the whole volume of the sample. Therefore, simple 2D cross-sectional imaging is not reliable for 3D structures, as there is no control of the current flow. In this scenario, electrodes should be distributed in 3D arrangements to improve sensitivity (WU et al., 2018). However, this introduces complexity in the manufacturing process, as well as increasing the total number of electrodes required. Finally, the EIT problem is highly ill-posed (HOLDER, 2004), which means that small errors in the boundary voltages can cause large errors in the reconstructed image.

# 4 MATERIALS AND METHODS

## 4.1 BIOPRINTER DESIGN

To produce the 3D printed parts for the EIT experiments, a 3D bioprinter was developed. The machine is based on the robotic extrusion paradigm, and is composed of a syringe pump connected to the header using a silicon tube and a needle, a positioning unit, responsible for controlling the nozzle in the XYZ coordinates, and a main board, that provides control signals for the extruder and the dispensing unit, and receives commands from the host computer. The design details, as well as the hydrogel synthesis, are presented in this section.

### 4.1.1 Robotic Extruder

The extruder consists of one syringe pump, that sends the hydrogel to the nozzle using flexible tubes. The dispensing nozzle is made of a blunt-tip needle. The pump piston and body were developed using PLA 3D printed parts. The actuation mechanisms of the pump is based on a bipolar stepper motor, a rectangular lead-screw connect to the piston to convert circular motion to linear actuation, a medical grade syringe containing the hydrogel, a flexible tube and a needle. The 3D printed header is designed so that each needle can be easily replaced, using luer-lock connectors. Each stepper motor is electrically controlled by the main board, using 4 digital signals (12 V of amplitude) generated by a stepper driver A4988. The driver was set to 1/16 microstepping mode, to increase the control range of the flow. Differently from conventional bioprinting machines, the syringe pump was designed to operate outside the header. This decision was made for two reasons: to reduce the header weight, which minimizes the risk of missing steps and vibration, and to allow different multi-printing configuration, such as mixing and coaxial nozzles, without needing to replace the complete extrusion system.

### 4.1.2 Positioning Unit

The positioning unit is responsible for positioning the header according to the printing program. It is composed of an aluminum triaxial frame, three 12 V stepper motors to control the axis movement, circular-to-linear motion mechanisms (based on lead-screws, metal rods and bearings) and three end-stops to limit the motion control. The frame was made by adapting a *Ender 8* 3D printer (Creality™).

### 4.1.3 Main Board and Firmware

The main board is the general control unit of the bioprinter. It is based on the Ramps 1.4 control board, which provides the necessary connections between the microcontroller and the peripherals. The Ramps 1.4 is mounted on top of an Arduino Mega™board. The Arduino Mega is a development board containing an ATMega368 microcontroller, which is the main logic unit of the printer. The ATMega368 is connected to the motor drivers, LCD display, heater, temperature sensor and buttons via the Ramps 1.4 board. The Ramps 1.4 provides slots for three positioning motors (XYZ) and two extruder motors.

The ATMega368 is programmed using the Marlin 2.0 firmware, which is a multiplatform open-source firmware optimized for RepRap  3D printing. The firmware is constantly being updated and upgraded by the maker community, and this consistent evolution makes it one of the most reliable and efficient 3D printing firmwares in the market. Another advantage is that it can be easily modified to support new functions, G-CODE commands and platforms. The Marlin firmware contains machine configurations, kinematic functions, peripheral drivers and the communication language, which is based on G-CODE commands.

There are two interfaces between user and the main board. The first is the LCD display and a control knob, that allows the user to preset printing parameters on-the-fly without a computer. The second is via serial communication with the host computer, using USB connection. The host computer communicates with the board using the G-CODE commands supported by the Marlin software.

### 4.1.4 Host Software

The host computer is responsible for slicing the 3D model and converting the file into a G-CODE sequence. This sequence is sent to the bioprinter using USB communication. Each command triggers one function embedded in the firmware, which performs a certain task. G-CODE lines are composed of a command followed by parameters, and ends with a semicolon. For instance, the G-CODE line:

```
G0 X50 F3000;
```

means a linear movement (command G0) of 50 mm in the x-direction (parameter X50) with a feedrate of 30000 mm/min (parameter F3000). The whole G-CODE dictionary, containing all possible commands and parameters, is well documented on the Marlin website.

The slicer implemented in this thesis was the Cura 4.0 slicer, which allows configuration of both the machine and materials to be used. This is important in this project, as the hydrogel is not a typical material in 3D printing, and the printing flow, speed and retraction parameters should be carefully defined for each bioink. Also, this slicer allows post-processing of the G-CODE sequence, that was used to configure the start and end routines of the printing process.

### 4.1.5 Hydrogel Synthesis

Because of its versatility, robustness and printability, alginate was chosen as the main hydrogel component for this bioprinter. Alginate gelification is a chemical process that occurs in the presence of ${C_a}^{+2}$ ions, forming a molecular grid by binding the alginate polymeric chains together via electrostatic forces. This grid, combined with water, forms a mechanically stable and biocompatible hydrogel that can be used as a initial scaffold for cells. However, alginate alone is not mechanically stable for printing before crosslinking, so gelatin was added to the bioink to improve viscosity (LI et al., 2018). The printing process is described in Figure 4.1.

Figure 4.1 – The developed bioprinting process. First, the bioink is extruded on top of a gelatin bath (a). After the biopriting is finished (b), the part is crosslinked using a 11 mM $CaCl_2$ solution for 15 minutes. The gelatin is then heated at 39ºC to free the part and melt the gelatin from the part. The gelatin is finally removed and the construct is rinsed with distilled water at room temperature (d).

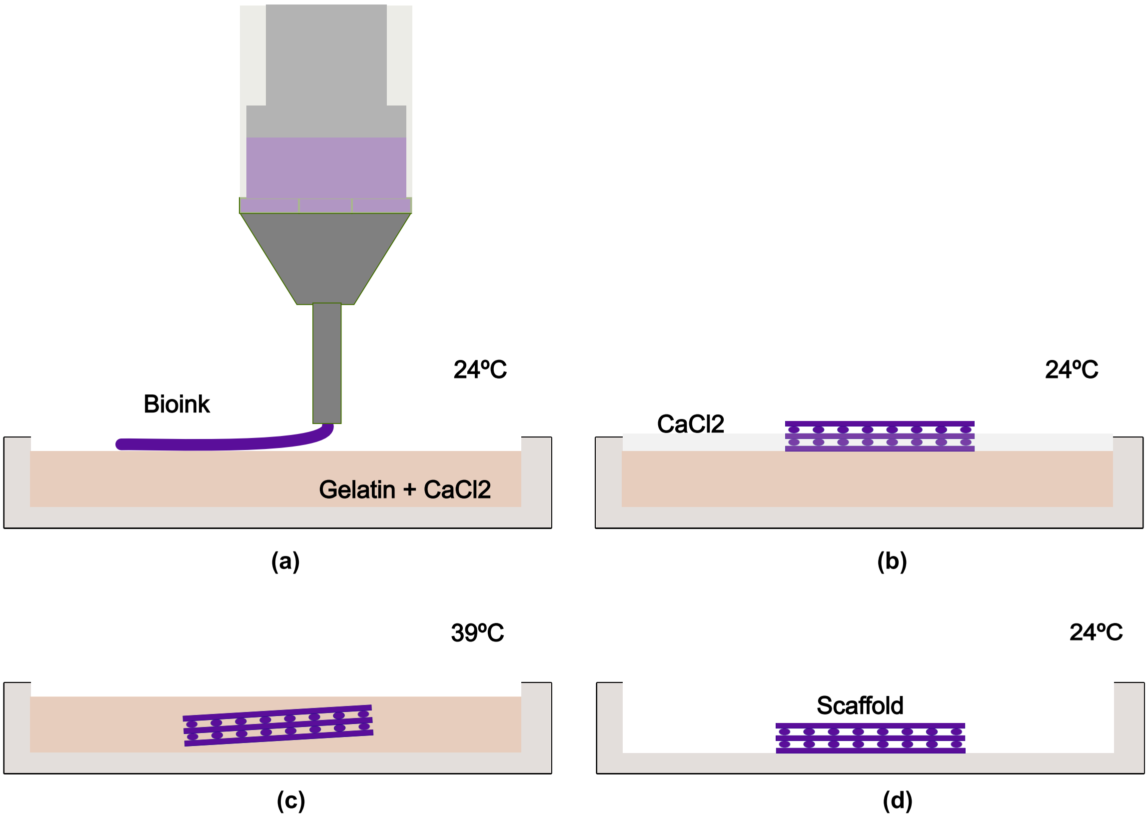

Source: Produced by the Author, 2021.

The developed bioink consisted of a mixture of 2% w/w solution of sodium alginate and 4% w/w gelatin. This mixture was based on the work of (LI et al., 2018), that proposed the use of a gelatin/alginate composite to improve the rheological properties of the bioink. The hydrogel was also mixed with five drops of food grade purple dye, which is used to better distinguish the liquid flow during printing. This mixture was prepared in a temperature of approximately 70° C. The alginate bioink was then printed on top of a gelatin bed (7% w/w) containing 11 mM of $CaCl_2$, inside a petri dish. At the end of the printing process, a 11 mM $CaCl_2$ solution was added to the petri dish, and the mixture was heated at 37 °C to melt the gelatin. The $CaCl_2$ was used to gelify the alginate, and the gelatin is used to provide a flat, soft and lightly wet surface for printing. Figure 4.2 shows the bioprinter setup and the bioprinting process in practice.

Figure 4.2 – Bioprinting setup developed and implemented in the experiments (a) and the printing process (b).

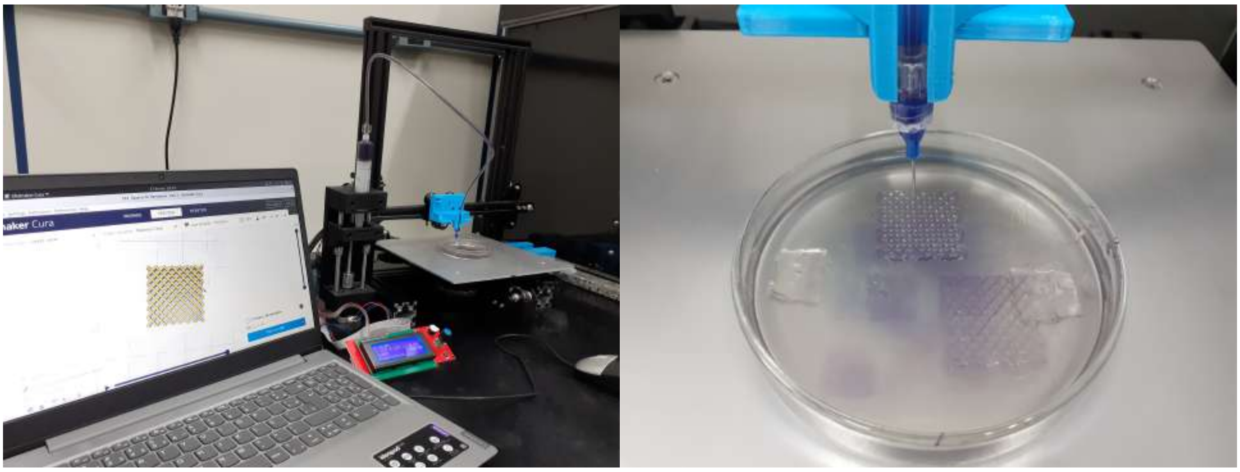

(a) (b)

Source: Produced by the Author, 2021.

## 4.2 DESIGN TOOLS

### 4.2.1 Simulation and Design Tools

Simulations were performed to test and validate both the analog circuit and image reconstruction algorithm before experimental implementation. EIDORS was used as the main simulation framework for image reconstruction, whereas PSPICE was used to simulate the circuit aspects. Moreover, to verify how the circuit affects the image reconstruction process, a, integrated simulation framework was developed, combining both PSPICE and EIDORS. This framework is described in subsection 6. The software KiCAD was used for layout design of both the circuit and the electrode array.

### 4.2.2 Processing

To each measurement in EIT, a single number is assigned to each measurement, representing the contribution of the measurement to the image reconstruction process. Because square waveforms were used in this thesis, FFT was applied to collect the value of the fundamental harmonic of the voltages. The FFT was calculated using the equation 4.1.

$$Y(f) = \sum_{t=1}^{n} X(t) W_n^{(t-1)(f-1)} \tag{4.1}$$

Where $Y$ is the harmonic vector in the frequency domain, $X$ is the signal vector in time, $n$ is the number of points, $t$ and $f$ are the time and frequency independent variables (respectively), and $W_n$ is equal to:

$$W_n = e^{\frac{-2\pi j}{n}} \tag{4.2}$$

### 4.2.3 Image Reconstruction

The reconstruction software was implemented in MATLAB, based on the EIDORS library. The EIDORS is an open-source EIT MATLAB library that contains several functions to perform EIT, such as forward problem solvers, Jacobian matrices, image reconstruction algorithms and mesh-generation functions for FEM. To obtain FEM models that accurately represent the system, the NETGEN mesh generator was used in combination with EIDORS. NETGEN is an automatic 3D tetrahedral mesh generator, and EIDORS provides native interface functions with the software. In this thesis, the Iterative Total Variation Regularization algorithm was implemented as the main reconstruction method (see Section 3.2.4), based on the technique proposed by Andrea Borsic *et. al* (BORSIC et al., 2007). To facilitate the imaging process, a circular 2D FEM model was implemented, using the *mk_circ_tank()* EIDORS function.

### 4.2.4 Testbench Equipment

The HF2IS impedance analyzer (Zürich Instruments) was used as reference device, to evaluate the absolute impedance of the samples. The RTC1002 oscilloscope and signal generator (Rohde & Schwarz) was implemented to measure voltage and current values, used to characterize the analog circuit. A test-bench power-supply of ±5 V was used to provide power to the prototype.

# 5 PROPOSED SYSTEM

The micro-EIT system was designed following the conclusions of the literature review presented in Chapter 3, considering all the limitations and requirements of a compact and precise EIT device. The proposed system is described in Figure 5.1.

Figure 5.1 – Proposed micro-EIT system

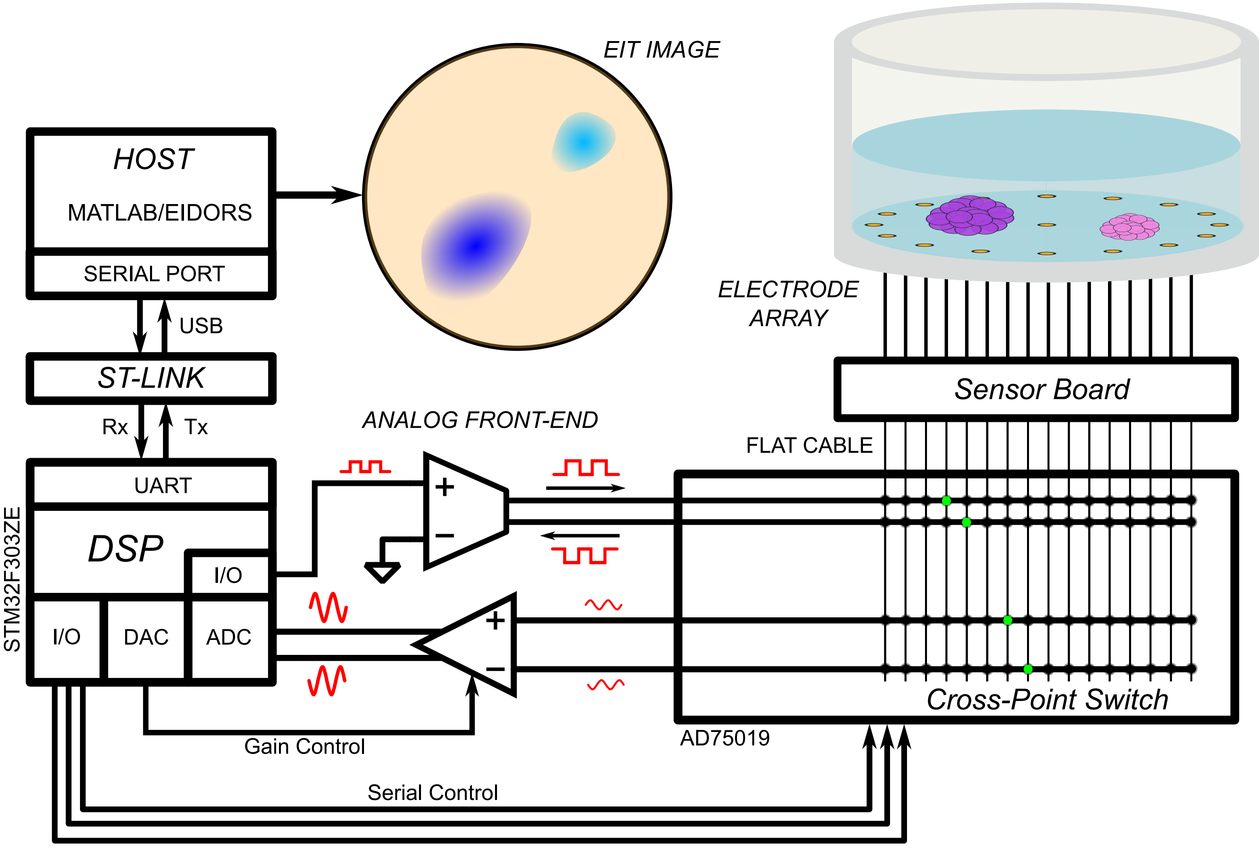

Source: Produced by the Author, 2021.

The system can be divided in four parts: the analog front-end, the digital module, the host computer and the sensor array. The analog front-end is composed by the excitation circuit, the voltage sensing circuit and the commutation module. This stage is controlled by the digital unit, which performs analog-to-digital conversion, gain adjustment, channel selection, signal generation and communication with the host. The host computer provides an interface between user and machine and performs the image reconstruction using the EIT data. Finally, the electrode array is the physical interface between the analog front-end and the sample. This section describes how each stage was implemented, as well as the signal specifications and measurement protocols applied.

## 5.1 EXCITATION CIRCUIT

The excitation circuit was designed to provide a square-wave current with constant amplitude to the load. The load current should be independent of the load within the whole frequency range. The Howland current source is a voltage controlled current generator that provides high output impedance and stability with discrete components, being one of the most implemented excitation topologies in BIA and EIT. Therefore, this topology was selected as the basis of the excitation unit. However, the single-ended Howland source provides poor common-mode performance, injecting common-mode currents with half the total signal amplitude (SIRTOLI; MORCELLES; VINCENCE, 2018). This can lead to measurement errors due to the limited CMRR of the sensing circuit. To reduce common-mode voltage, as well as to increase the voltage compliance of the source, a differential Howland topology was designed (Figure 5.2).

Figure 5.2 – Proposed Excitation Circuit

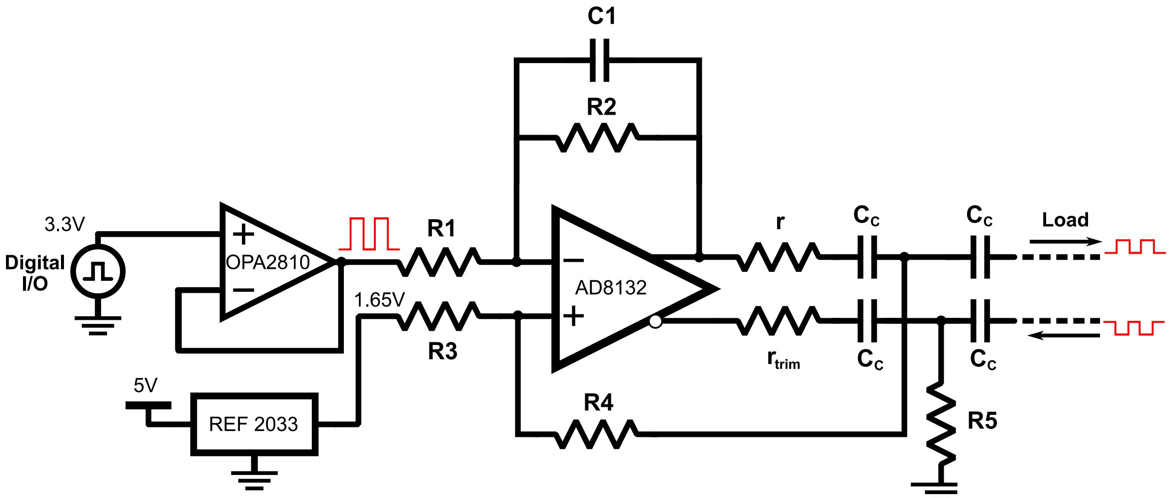

Source: Produced by the Author, 2021.

The differential Howland source implemented is based on a fully-differential operational amplifier. This type of amplifier applies an internal common-mode adjustment to create two outputs that have equal value with opposite signs. The difference between both outputs is proportional to the difference between the inputs, whereas the common mode voltage of the outputs is defined by the common-mode pin. The differential Howland topology implemented here was based on the Diff-M circuit proposed by Sirtoli *et al* (SIRTOLI; MORCELLES; VINCENCE, 2018). The design parameters are described below:

Table 5.1 – Design Parameters for the Differential Mirrored Howland

| | |
|---|---|
| Maximum Amplitude | 250 $\mu$A |
| Frequency Range | 10 kHz - 100 kHz |
| Waveform | Square |
| Load Range | 0 - 3.3 kΩ |
| Supply Voltage | ±5 V |

These requirements were used to select the operational amplifier and design the Diff-M source. The AD8132 is a fully differential amplifier with 300 MHz of gain-bandwidth, which provides stable unity gain and high slew-rate (1200 V/$\mu$S) to generate square waves with 100 kHz. Also, it provides high input impedance (12 MΩ || 1 pF), which are fundamental in Howland sources to prevent instability issues and to ensure high output impedance. The common-mode pin of the AD8132 was set to 1.65 V.

The Diff-M resistors were calculated using Equations 5.1-5.3 (SIRTOLI; MORCELLES; VINCENCE, 2018). Equation 5.1 describes the Howland balance condition, necessary to obtain maximum output impedance; and equation 5.2 represents the common-mode balance condition, that minimizes the output common-mode voltage. If both conditions are met, the output current is defined by Equation 5.3.

$$\frac{R_4 + r_x}{R_3} = \frac{R_2}{R_1} \tag{5.1}$$

$$R_5 = R_4 + R_3 \tag{5.2}$$

$$I_{out} = \frac{V_{in}}{r_x} \times \frac{R_2}{R_1} \tag{5.3}$$

Therefore, any resistor set that satisfies all the above equations can be used to provide a stable and functional current source. To reduce the value of $r_x$, the ratio $R_2/R_1$ was selected to be 0.5, which is an attenuation gain that still keeps the AD8132 stable. This is done to increase the maximum load, as large $r_x$ values tend to reduce voltage compliance (MORCELLES et al., 2017). The input voltage comes from the microcontroller's I/O, which has a maximum amplitude of 1.65 V (0 to 3.3 V peak-to-peak). To satisfy the output current described in Table 5.1, the value of $r_x$ must be 3.3 $k\Omega$ (Equation 5.3).

The remaining resistors were selected according to the trade-off between bandwidth and compliance: large resistors reduce the feedback current, increasing the maximum load, but large resistors combined with the input capacitance of the amplifier increase the current peak at high frequencies (MORCELLES et al., 2017; TUCKER; FOX; SADLEIR, 2012). Using the balance conditions described previously, the resistor set obtained was: $r_x$ = 3.3 $k\Omega$, $r_{trim}$ = 3.3 $k\Omega$, $R_1$

= 20 $k\Omega$, $R_2$ = 10 $k\Omega$, $R_4$ = 10 $k\Omega$, $R_3$ = 26.6 $k\Omega$ and $R_5$ = 36.6 $k\Omega$. To increase stability, a negative feedback resistor $C_1 = 0.5\ pF$ was added to the design. Capacitors $C_C = 1\ \mu F$ were used to decouple the DC current from the biological load.

Because square waves were used, the input signal was generated by the microcontroller's digital GPIO. However, the impedance of digital pins may interfere with the Howland balance. To isolate the Howland from the GPIO impedance, a voltage buffer was used, based on the OP2810 amplifier. This amplifier provides high input impedance (FET inputs) and stable unity gain at 105 MHz. It also achieves high slew-rates of 192 $V/\mu s$. Furthermore, a reference source (REF 2033) provides a stable 1.65 V to the positive pin of the Howland Source, referencing the differential input in zero.

## 5.2 VOLTAGE MEASUREMENT MODULE

This module is responsible for measuring the voltage difference between any pair of electrodes. It receives the voltage difference from the electrode array, rejects the common-mode voltage, amplifies the signal according to the amplitude, filters any DC voltage and high frequency noise and finally sends the signal to the ADC input. In this thesis, the circuit was designed in three stages: the input stage, the VGA and the anti-aliasing filter. The whole circuit was designed to operate with fully-differential signaling, to increase common-mode noise and interference immunity. Differential signaling also improves linearity, voltage compliance and signal-to-noise ratio.

The input stage provides high input impedance for the electrode signal, preventing current leakage. Typically, instrumentation amplifiers are used at the input, mainly to reduce the common-mode voltage. However, there are not many fully-differential instrumentation amplifiers in the market providing both high input impedance and large bandwidth. Thus, two identical buffers were used instead. The buffer implemented was based on the OPA2810, which provides FET inputs and stable unitary gain. To isolate the DC voltage from the VGA stage, two 2 $\mu F$ capacitors were used in series with the buffer outputs. The capacitors combined with the PGA input resistance of 500 Ω creates a high-pass filter with cut-off frequency at 159.15 Hz, which is approximately 62 times smaller than the minimum operating frequency (10 kHz), preventing phase errors.

The VGA stage is designed to adapt the measured signal amplitude to obtain maximum resolution for the ADC. The VGA is controlled by one of the DAC channels of the microcontroller. The core of the VGA is the AD8338 chip, which is a fully-differential VGA. The amplification process in this chip is performed in current mode, and two transimpedance amplifiers convert the amplified current to a differential voltage at the output.

The common-mode of the circuit is defined internally as 1.5 V, which is also why the DC inputs were blocked by the 2 $\mu F$ capacitors. The differential gain can be controlled by the DAC voltage, with values between 0 dB to 80 dB with a linear volts to dB slope (12.5 mV/dB). Although the VGA operates in current mode, it allows voltage inputs using internal 500 Ω resistors.

The final analog stage of the voltage measurement circuit is the anti-aliasing filter. A third-order Butterworth multiple-feedback filter was implemented, using a fully-differential topology based on the AD8132 amplifier. The filter was designed with a cut-off frequency of 1 MHz and quality-factor of 0.707, which yields a flat response with minimal error at the maximum frequency (100 kHz). The value of resistors and capacitors were calculated using Filter Design tool, from Texas Instruments ™. First, a single-ended circuit was calculated, and then the circuit was adapted to fully-differential operation. The output of the filter is connected to the differential ADC. Both outputs of the antialiasing filter were terminated with 3.3 V Zener diodes, to protect the microcontroller inputs.

Figure 5.3 – Sensing circuit with all amplification and filtering stages

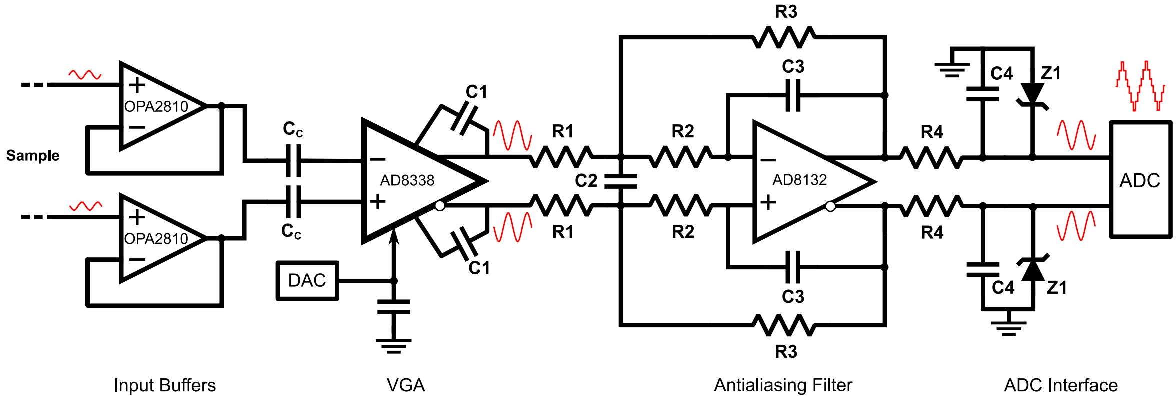

Source: Produced by the Author, 2021.

## 5.3 COMMUTATION STAGE

The commutation stage controls the connections between electrodes and the analog front-end. To support arbitrary EIT protocols, any electrode should be connected to both the voltage measurement module and the excitation circuit through a switch. Therefore, the developed system was based on the 16x16 cross-point switch AD75019, which allows control over 256 switches via serial communication. The AD75019 provides 16 input and 16 output channels, and any of the input channels can be connected to one or more output channels (and vice-versa) by setting individual switches. The main advantage of this configuration is that it requires only one IC and three control signals: a serial data line to select which switches should be ON and OFF, a serial clock, to load the internal shift register of the AD75019 that stores the serial data, and a parallel clock, used to load the register state to the actual switches. In comparison, a multiplexer configuration with the same characteristics would require 4 ICs (16x1 multiplexers) and 16 control signals (4 for each multiplexer).

Figure 5.4 – Cross-point switch commutation module. Each intersection between the lines represents one switch, and the green lines represent the selected channels.

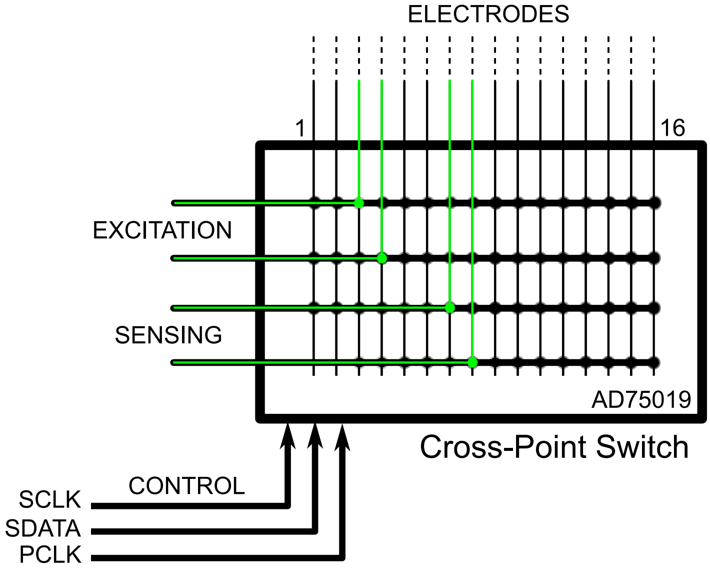

Source: Produced by the Author, 2021.

The maximum serial clock rate of the AD75019 is 5 MHz, which results in a minimum switching time of 52 $\mu s$. An adjacent protocol for EIT, with no measurements at the excitation electrodes, requires 208 measurements. This means a maximum frame rate of $1/(208 \times 52 \mu s) =$ 92.46 frames per second. Therefore, the main disadvantage of using the AD75019 is the speed penalty, especially systems if using 32 electrodes or more. However, for the scope of this thesis, the maximum speed is way beyond the required frame-rate. The series ON resistance of the AD75019 is 200 Ω, the common-mode capacitance is 25 pF and the channel isolation is more than 69 dB at 10 kHz. In the proposed module, the AD75019 was controlled by the STM32 digital GPIOs, all 16 electrodes were connect to the output channels and the excitation circuit and measurement system were connected to four input channels.

## 5.4 ELECTRODE ARRAY AND SENSOR ASSEMBLY

Typical EIT electrode configurations are based on lateral rings of electrodes facing a cross-section of the sample. However, this is not optimal if 3D EIT images are required. Therefore, planar electrodes at the bottom of the culture well were designed, providing quasi-3D sensitivity fields that can be used to reconstruct 3D images. Another advantage of the planar geometry is that it can be fabricated using simple PCB manufacturing manufacturing, which allows direct integration with the processing board.

Different planar electrodes geometries can be found in the literature. From these, the one proposed by Yang *et al* was the most successfully implemented in cell cultures (YANG et al., 2016). The design is easy to implement in PCB technology, is able to reconstruct 3D images and avoids direct contact between electrode and cells, reducing spike noises at the bottom of the sample (YANG et al., 2016). Therefore, the electrode sensor applied in this article was inspired by the paper. The proposed electrode array consists of 16 planar electrodes in circular shape (diameter = 1 mm), distributed equally in a circle with 15 mm of radius at the bottom of the culture well. At the center of the ring, a ground electrode (diameter = 0.4 mm) was placed, to bias the sample and reduce common-mode voltage coupled from the power lines (Figure 5.5).

Figure 5.5 – Designed electrode array (a) and implemented sensor (b)

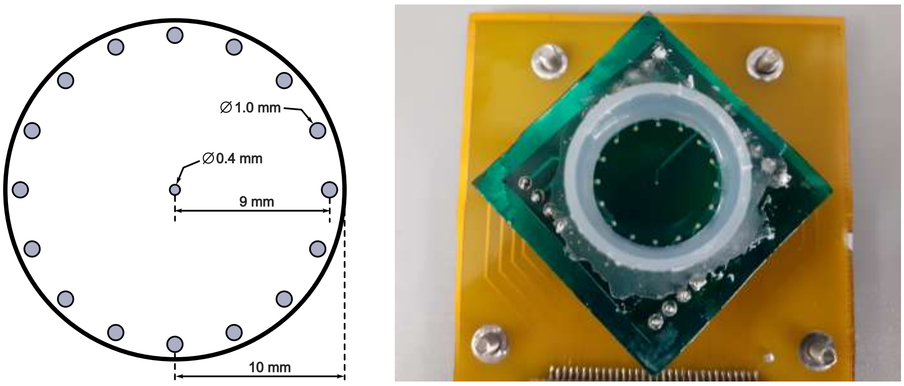

(a) (b)

Source: Produced by the Author, 2021.

The electrodes were manufactured in gold coated copper, using PCB technology and sputtering coating, on top of a glass fiber board, which is mechanically resistant and provides low parasitic capacitances. A photo-resist mask was implemented to passivate the undesired areas, leaving only the circular electrodes exposed. An acrylic cylinder, with 10 mm of height and 20 mm of diameter, was glued to the electrode board, concentric to the ground electrode (Figure 5.5). To fix the cylinder to the board, a medical grade methyl-methacrylate resin was used. The electrode board was connected to a holder board via pin headers.

The connection between the electrode board and the analog front-end was made using a FFC cable with 32 wires. From 1 to 32, even-numbered wires connect the electrodes to the AD75019 cross-point switch, and odd-numbered wires carries the ground reference. The alternation between signal wire and ground wire reduces cross-talk between channels and increases EMI immunity. Although flat cables provide significantly less EMI immunity than coaxial cables, they were selected due to the small footprint. The degradation in EMI immunity is compensated by the fully differential operation of the measuring system, that reduces common-mode interference and coupling.

## 5.5 SIGNAL SPECIFICATION AND MEASUREMENT PROTOCOL

The device was designed to measure Time Difference EIT (TDEIT) at 10 kHz and Frequency Difference EIT (FDEIT) at 10 kHz and 100 kHz. To prevent frequency variations cause by stray capacitances and other non-idealities, the calibrated FDEIT method proposed by Wu *et al* (WU et al., 2019) was implemented (see Section 7.3.2). Both 10 kHz and 100 kHz frequencies were selected because they are within the alfa and beta dispersion range, which are typically used to characterize tissue, and were successfully implemented in cell-culture EIT (MORCELLES; BERTEMES-FILHO, 2021). During each scan, 5 periods of the voltage response signal were measured for each channel. Because the signals are square-waves, the FFT was calculated to isolate the magnitude of the fundamental harmonic. Only the absolute magnitude of the fundamental harmonic was used in signal reconstruction.

The proposed EIT system implements the adjacent measurement protocol, without measuring the voltage at the current driving electrodes. The process is described in Figure 5.6. The adjacent protocol was selected due to its good performance in cell culture imaging and the reduced number of measurements required (HOLDER, 2004; WU, 2020). However, the adjacent protocol is not optimal for imaging the center of the sample (ADLER; BOYLE, 2017), due to the reduced field density at this location. The opposite measurement protocol is an alternative, with an increased field density at the center it provides better sensitivity for central conductivity variations (RUSSO et al., 2017).

Figure 5.6 – Adjacent protocol description

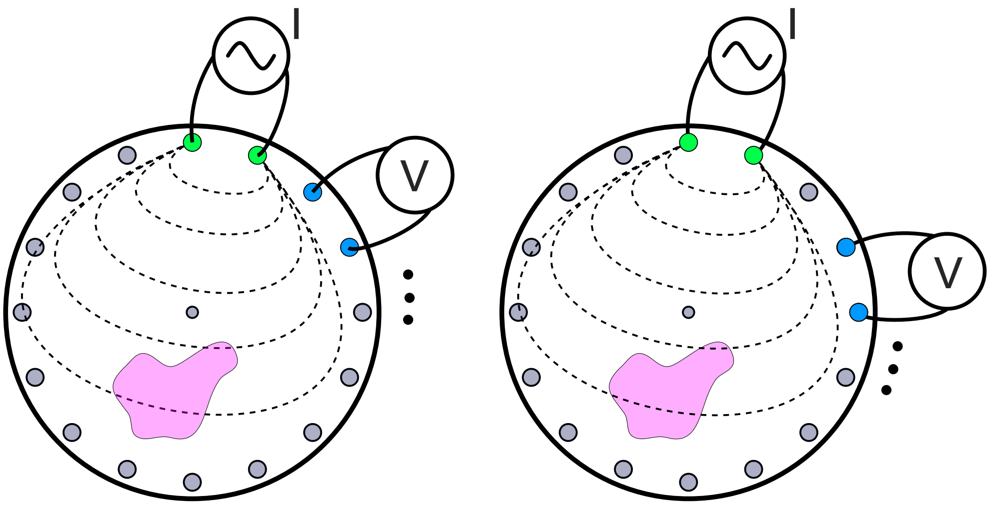

Source: Produced by the Author, 2021.

Figure 5.7 – Injection current distribution using adjacent protocol (a) and opposite protocol (b)

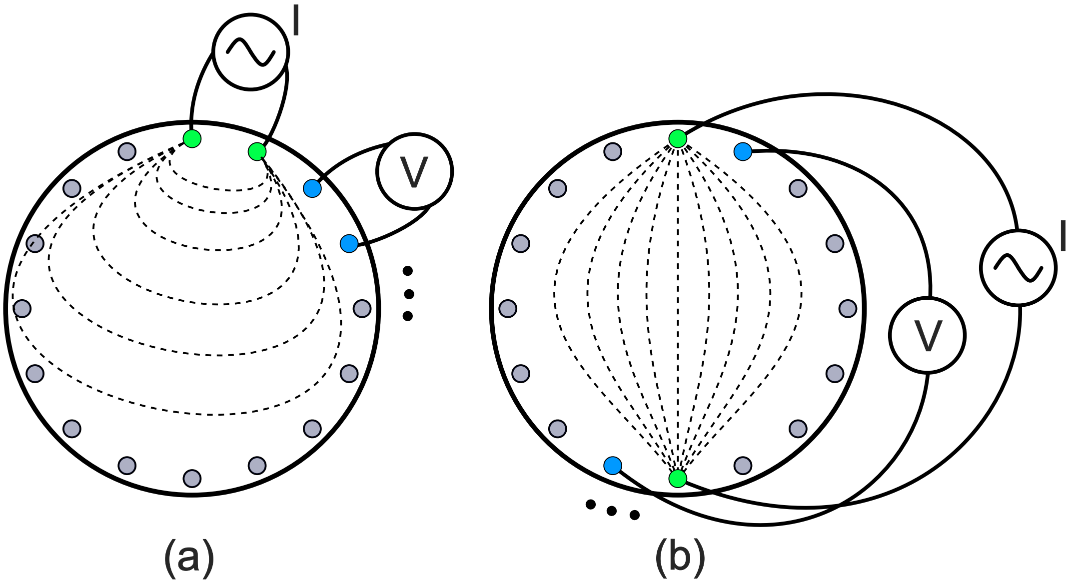

Source: Produced by the Author, 2021.

For 16 electrodes, the adjacent protocol requires $16 \times 13 = 208$ measurements. The period of each measurement can be calculated using Equation 5.4, where $t_{tot}$ is the total measurement time, $t_s$ is the sampling time, $t_{sw}$ is the switching time and $t_{stab}$ is the channel stabilization period.

$$t_{tot} = t_s + t_{sw} + t_{stab} \tag{5.4}$$

The five periods of the signal take $t_s = 500\ \mu s$ (10 kHz) or $t_s = 50$” $\mu s$ (100 kHz) to finish. Considering that the minimum $t_{sw}$ is 52 $\mu s$ (subsection 5.3) and each channel takes $t_{stab} = 100\ \mu s$ to stabilize, the total measurement time is $t_{tot} = 652\ \mu s$. Therefore, each adjacent and opposite scan takes $208 \times 0.652 = 135.62\ ms$ to complete. In this case, the maximum frame rate is 7.37 fps at 10 kHz and 23.8 fps at 100 kHz.

## 5.6 MICROCONTROLLER UNIT AND FIRMWARE

The microcontroller unit (MCU) selected was the STM32F303ZE, from STMicroelectronics™. This microcontroller is based on the ARM Cortex-M4 processor core (32-bits). From the several features and peripherals provided by the MCU, the ones implemented in this work were:

- Clock frequency at 72 MHz;
- High-speed memories (512 Kbytes of flash memory and 64 Kbytes of static random-access memory - SRAM);

- Two direct memory access (DMA) controllers;
- Four 12-bit ADC with sampling frequency of 2 MS/s in a differential configuration;
- One 12-bit DAC for VGA control;
- Three general purpose timers: one for signal generation using PWM , one for serial clock to communicate with the commutation circuit, and one for timebase interruption;
- A serial full-duplex serial communication interface using UART .

The MCU was embedded in a Nucleo-144 development board. This board is intended for rapid prototyping, and provides direct connection to the MCU through 4 external headers, USB connection and an integrated debugger/programmer ST-LINK/V2-1. The firmware was designed using the ST32Cube IDE provided by STMicroelectronics™. The main libraries implemented were the HAL Drivers and the peripheral configuration code generated using CubeMX.

The firmware runs as a state machine (SM) , with each state running a section of the EIT measurement process. The SM begins in the *RECEIVE COMMAND*, that receives commands from the host computer using UART communication (115200 baud rate, 8 data bits, odd parity). To ensure that no data is lost, and to avoid program blockage by polling, the DMA controller is called by the UART peripheral, so data can be received without the CPU . When the receive buffer is full, the action *COMMAND RECEIVED* is triggered, and the SM goes to the *TREAT COMMAND* state. The full SM map is described in Figure 5.8.

If the first character of the received command is ’G’, the SM enters the the *SET GAIN* state. In this state, the second character of the command message is used to set the VGA gain. According to the datasheet, the minimum and maximum voltages for the AD8338 gain selection are 0.1 V and 1.1 V, respectively. The firmware sets the DAC voltage according to Equation 5.5, where *Val* is the command value (8-bit unsigned integer). From this equation, one can see that the DAC voltage is limited between 0.1 V ($Val = 0$) and 1.1 V ($Val = 255$), with a step of approximately 3.92 mV per unit of $Val$. This translates into 0.3144 dB per unit of *Val* (see Section 5.3).

$$V_{DAC} = \frac{Val}{255} + 0.1 \tag{5.5}$$

The *SET CHANNELS* state becomes active if the first character of the command message is ’S’. In this case, the next four characters are respectively interpreted as: "Injection Electrode 1", "Injection Electrode 2", "Measurement Electrode 1" and "Measurement Electrode 2". The electrode numbers are then processed by the state function and sent to the AD75019 cross-point switch, via serial communication (2.5 Mbits/s).

Figure 5.8 – Firmware State Machine.

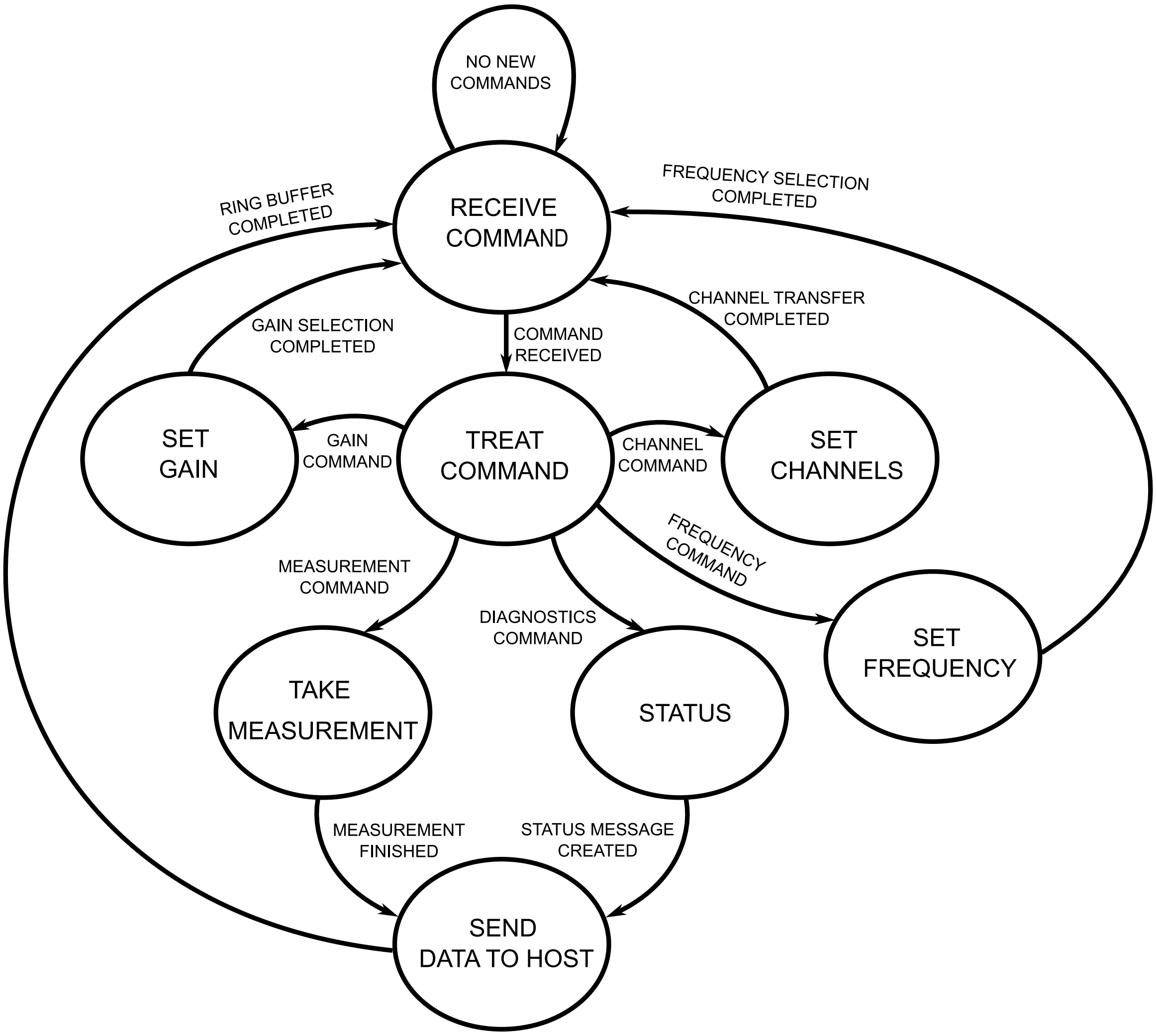

Source: Produced by the Author, 2021.

If the first character of the command is ’E’, then the SM activates the *SET FREQUENCY* state, with the second character being the frequency selection: ’0’ disables the signal, and ’1’ and ’2’ enables the 10 kHz and 100 kHz excitation signals, respectively. In this thesis, only square waves were applied (0 to 3.3 V), so the waveform is fixed. The signal was generated using the PWM peripheral, and sent to the Howland Source through a *push-pull* GPIO.

The *TAKE MEASUREMENT* state is the most important one. It is triggered when the host message begins with ’M’, and performs the measurement of a single channel. It initializes the differential ADC (configured to 2.5 MS/s), waits 100 $\mu s$ ($t_{stab}$) for stabilization, and measure five periods of the signal. The measured data is then stored in a buffer (SRAM) . The size of the buffer is equal to 1000. After measurement, the buffer is sent to the host via UART.

Finally, the *STATUS* state is activated when the system receives a character ’D’ from the host, and sends information about the current state of the EIT measurement, such as signal parameters, active electrodes and VGA gain value.

## 5.7 INTERFACE WITH HOST

The interface was used to control the system from the computer. It was implemented in MATLAB, and performs both the human-machine interface and the image reconstruction process. Figure 5.9 shows the flowchart description of the algorithm.

Figure 5.9 – Flowchart of the host interface algorithm

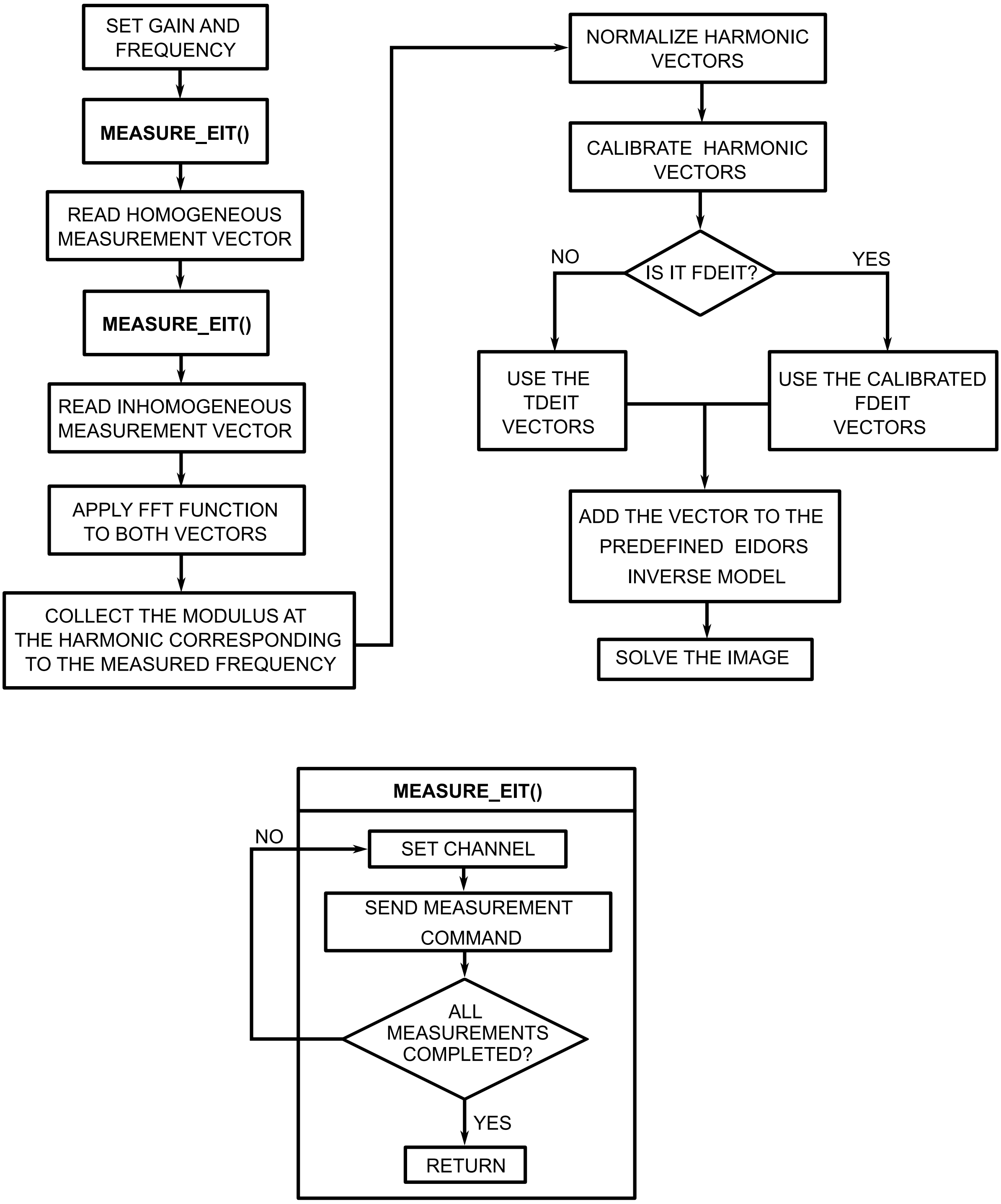

Source: Produced by the Author, 2021.

The interface is responsible for the communication with the board. The user can select the signal frequency, the EIT mode (if it is TDEIT of FDEIT), the calibration type and the VGA gain. The software then generates a command sequence that is sent to the board via UART (*MEASURE_EIT()* function), and receives the measurement buffer of each channel. The process is repeated for the homogeneous (reference) and inhomogeneous (the object of interest) samples. The output of the interface software is a CSV file containing the EIT parameters and all the measurement buffers of the EIT scan. After each scan, the measurement file is fed to the reconstruction software. For TDEIT, only one scan is measured per file (at 10 kHz), whereas in FDEIT, two scans are measured per file (at 10 kHz and 100 kHz).

## 5.8 SYSTEM ASSEMBLY

The analog front-end board was mounted on top of the Nucleo-144 board using pin header connectors. Both boards were fixed inside a package made of ABS plastic. The package was drilled to allow passage of the USB cable, flat cable and power-supply connectors. The sensor board was fixed on top of the box using M3 screws, and connected to the analog-front end through the flat cable. Finally, the electrode board containing the sample was mounted on top of the holder board using gold plated pin headers. The sensor was fixed outside the box to facilitate experiments.

Figure 5.10 – Proposed EIT equipment

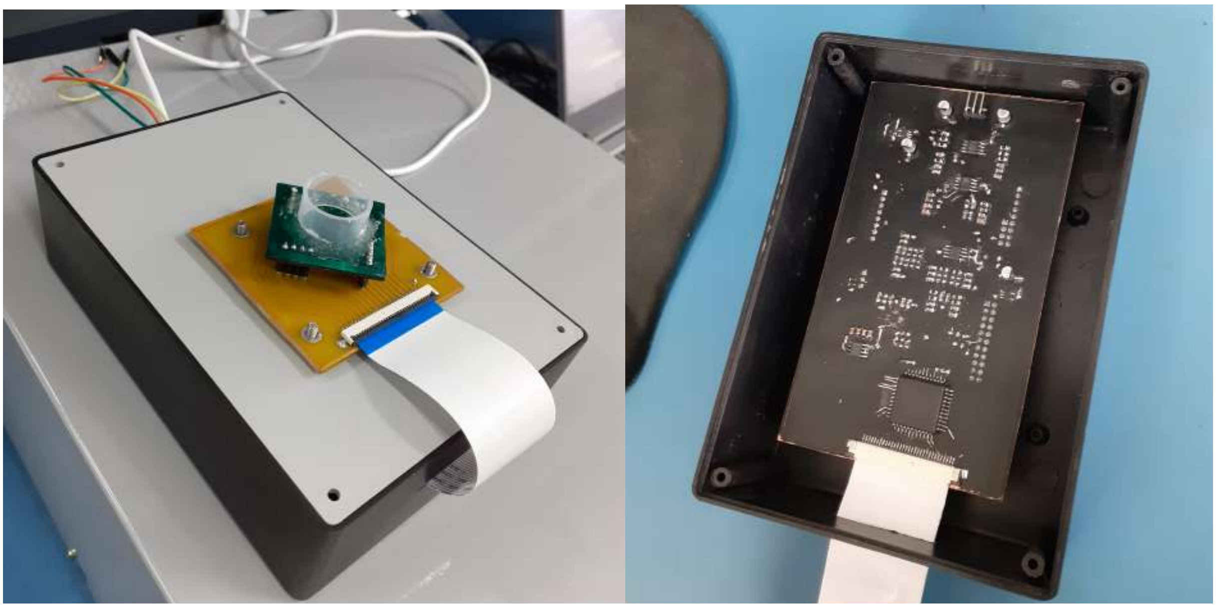

Source: Produced by the Author, 2021.

# 6 SIMULATION RESULTS AND DISCUSSION

Simulations were used to obtain preliminary results during the design of the electronic circuit, to guide and improve the process, as well to evaluate the performance of the software and the measurement method implemented. The simulation results were divided in three sections: the EIT simulation, the circuit characterization and the integrated EIT simulation. The first describes the ideal EIT simulations, which were used to select the measurement protocol, FEM model and reconstruction algorithm. The second analyzes the designed circuit performance in electrical terms. Finally, the third presents a simulation framework that integrates the EIDORS library with PSPICE, which yields more realistic results considering the non-idealities of the designed electronics.

## 6.1 EIT SIMULATION

The simulation of an EIT system in ideal conditions (that is, without considering the circuit non-idealities) was used to validate the electrode configuration, analyze the potential and sensitivity field distributions, and select the image reconstruction algorithm for the experiments. The ideal simulation process is described in Figure 6.2, following the "EIDORS SIMULATION" branch of the diagram. A Finite Elements Model (FEM) phantom (Figure 6.1) was designed to simulate an spheroid of breast tumor cells (MCF-7 line) inside a culture plate. The culture well was designed as a cylinder with 10 mm of radius and 5 mm of height. The spheroid was designed with a radius of 0.5 mm, and positioned 5 mm away from the center. The maximum element size of the mesh was 1 mm for the background, 0.5 mm for the spheroid and 0.5 mm near the electrodes.

Figure 6.1 – Homogeneous and inhomogeneous FEM phantoms used for simulation.

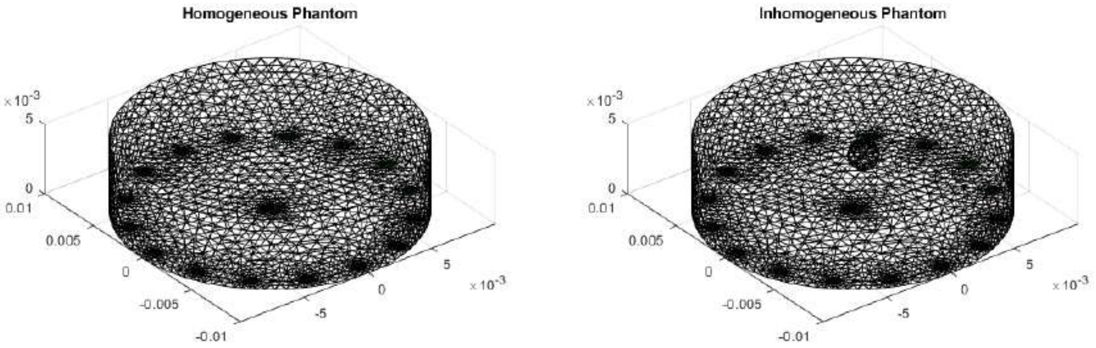

Source: Produced by the Author, 2021.

Figure 6.2 – Flowchart describing the simulation process

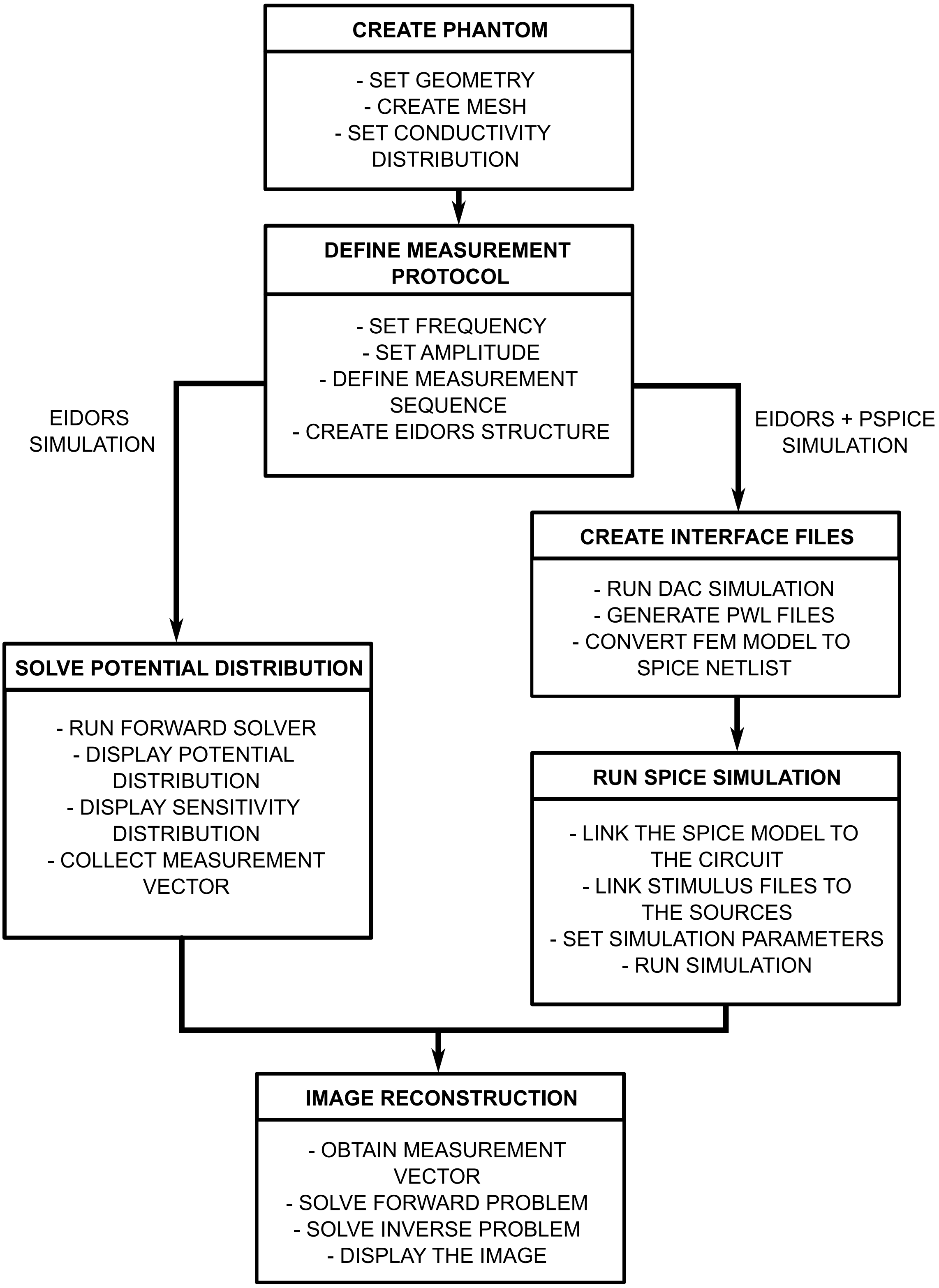

Source: Produced by the Author, 2021.

The conductivity of the background media was set to 1.5 S/m to simulate a culture media (WU, 2020). The conductivity of the spheroid was obtained using the effective medium approximation model implemented by Wu (WU, 2020). This model calculates an effective homogeneous conductivity for the spheroid using the Maxwell-Garnet and Hanai equations (ASAMI, 2002; SKRYABIN et al., 1997), which considers both electrical and geometrical characteristics of cells. The calculated conductivity of the spheroid was equal to 0.5952 S/m.

Using the EIDORS first-order forward solver and the adjacent measurement protocol (with injection current of 0.5 mA at 10 kHz), the potential distribution for each current injection was calculated. The visualization of the potential distribution provides better intuition about the EIT process. Figure 6.3a shows the ideal conductivity distribution of the phantom for several horizontal cross-sections (or Z-planes), used here as reference, and figure 6.3b shows the electric potential distribution for each current injection at a Z-plane that crosses the middle of the spheroid.

Figure 6.3 – Ideal conductivity distribution for several Z planes (a), the resulting potential distribution for each injection pair (b), the potential difference between homogeneous and inhomogeneous phantoms for each injection pair (c) and the potential difference for several Z planes.

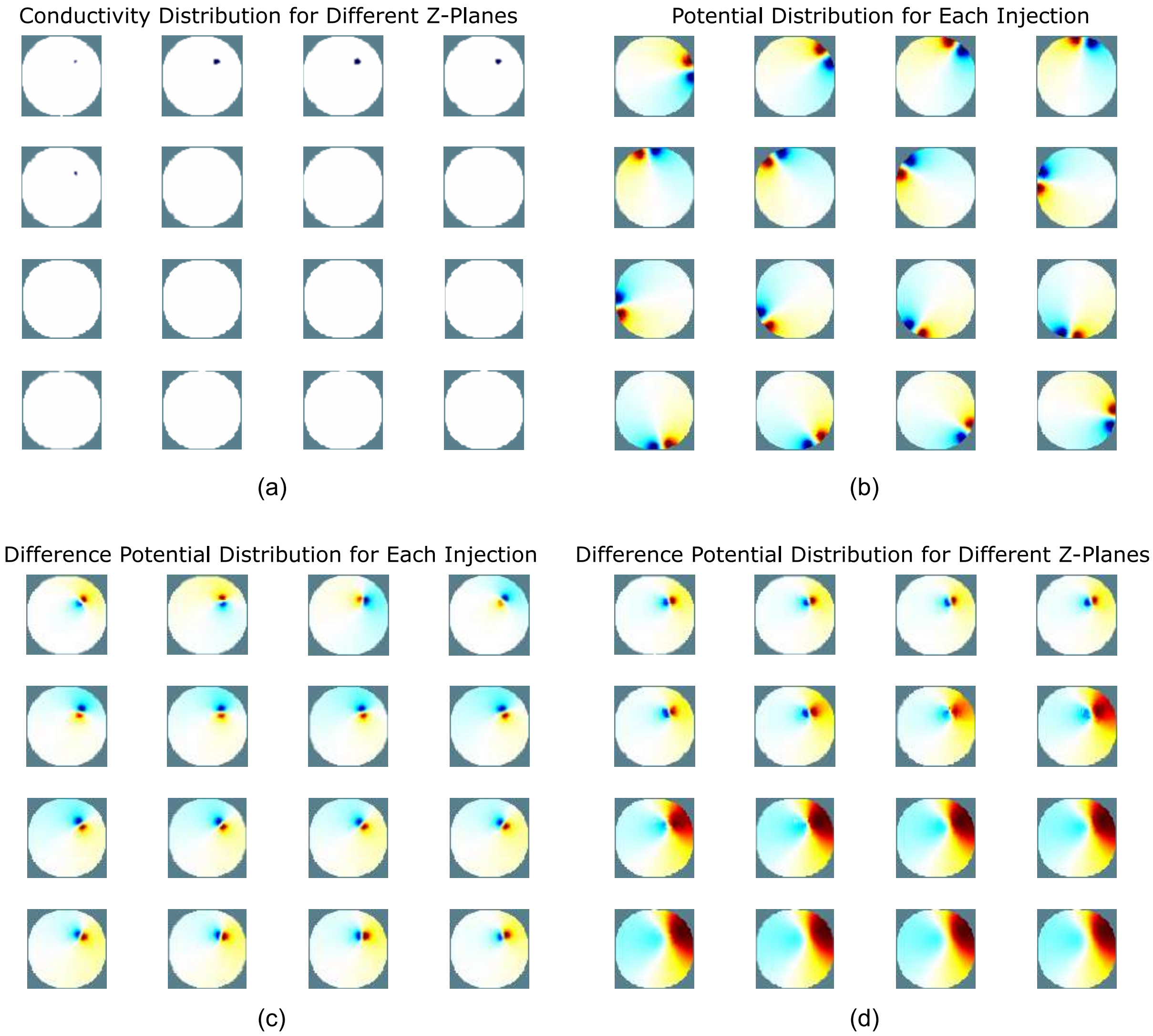

Source: Produced by the Author, 2021.

It can be seen that the electrical potential is significantly concentrated around the electrodes, with red being a positive potential and blue a negative potential, and the field disturbances caused by the spheroid are too small to visualize. However, when applying the difference between the potential distributions of the inhomogeneous and homogeneous phantoms (Figure 6.1), the contribution of the spheroid can be visualized, as shown in Figure 6.3c. The potential disturbance caused by the spheroid can be approximated to a dipole source. The potential of this electrical dipole spreads through the medium and reaches the electrodes, causing the measured voltage variation. Moreover, the orientation of the dipole moment rotates with the injection electrodes, indicating that it depends on the current density vectors near the spheroid. The dipole distribution for several Z-planes at increasing heights is shown in Figure 6.3d. As the height increases, the distribution becomes more diffuse, showing that the dipole fields are three-dimensional.

The sensitivity distributions for each injection/sensing pair were also analyzed. As explained in subsection 3.2.2, the sensitivity field is one of the most important parameters in EIT, which shows how much each portion of the measured volume contributes to the measured voltage (LIONHEART, 2004; BAYFORD, 2006). A region with high sensitivity will caused larger voltage variations for small changes in conductivity, so the SNR and, hence, the accuracy depends on where the spheroid is located. Figure 6.4a shows the sensitivity distributions for each injection/sensing pair. It can be seen that the regions with larger sensitivity modulus are near the electrode pairs (both injection and sensing). On the other hand, the sensitivity at the center of the sensor is almost zero for all measurement pairs. Therefore, it is expected that the EIT performance will be better for objects close to the boundaries of the sensor in comparison with objects near the center. This result is typical for adjacent protocols, and sensitivity at the middle can be improved by using other measurement protocols (DANG et al., 2021). Because the potential distribution is 3D, the sensitivity field also varies with the Z-planes. Figure 6.4b shows that the sensitivity distribution becomes less concentrated at the electrodes as the height increases.

Using the forward solver function provided by the EIDORS library, the simulated voltage differences for each injection/sensing pair were obtained for both the homogeneous and inhomogeneous phantoms. Time Difference EIT uses the variation of the measured voltages instead of the absolute voltage itself, so Figure 6.5 shows the normalized amplitude of voltage variations for each measurement. The measurement sequence corresponds to the adjacent EIT sequence discussed in Section 5.5.

Image reconstruction was performed using this ideal data vector. The first step in image reconstruction is the definition of the FEM model to solve the forward problem. When simulating EIT data, it is important to use different FEM models for the simulation and

Figure 6.4 – Sensitivity field distribution for each injection pairs (a) and for several Z planes with a fixed injection pair (b).

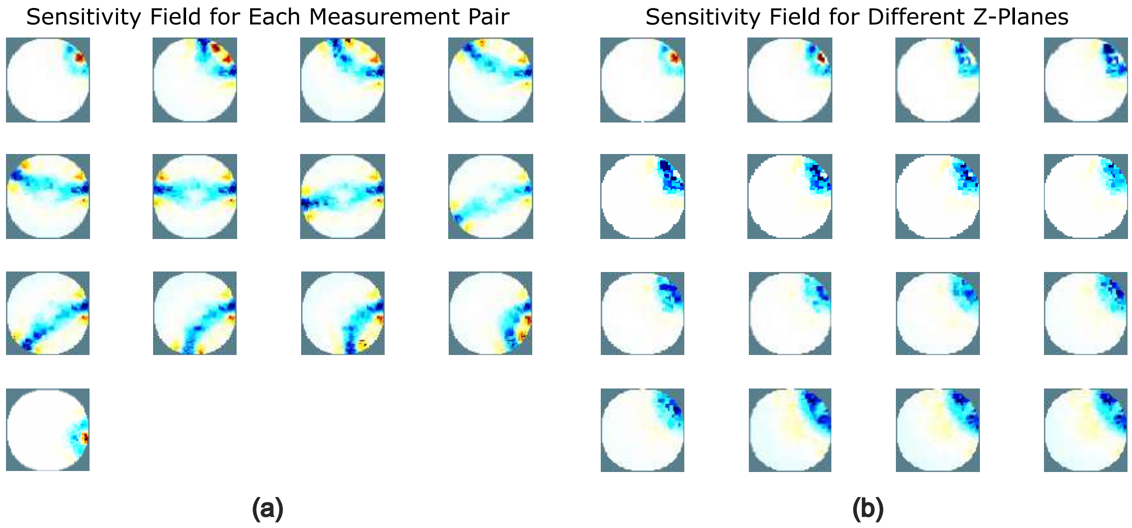

Source: Produced by the Author, 2021.

reconstruction steps (LIONHEART, 2004). Thus, a coarser mesh was used. Moreover, because only 2D image reconstructions were implemented in this thesis, the FEM model of the simulated EIT was also two-dimensional. The model is shown in Figure 6.6.

Figure 6.5 – Data vector obtained from the simulated EIT.

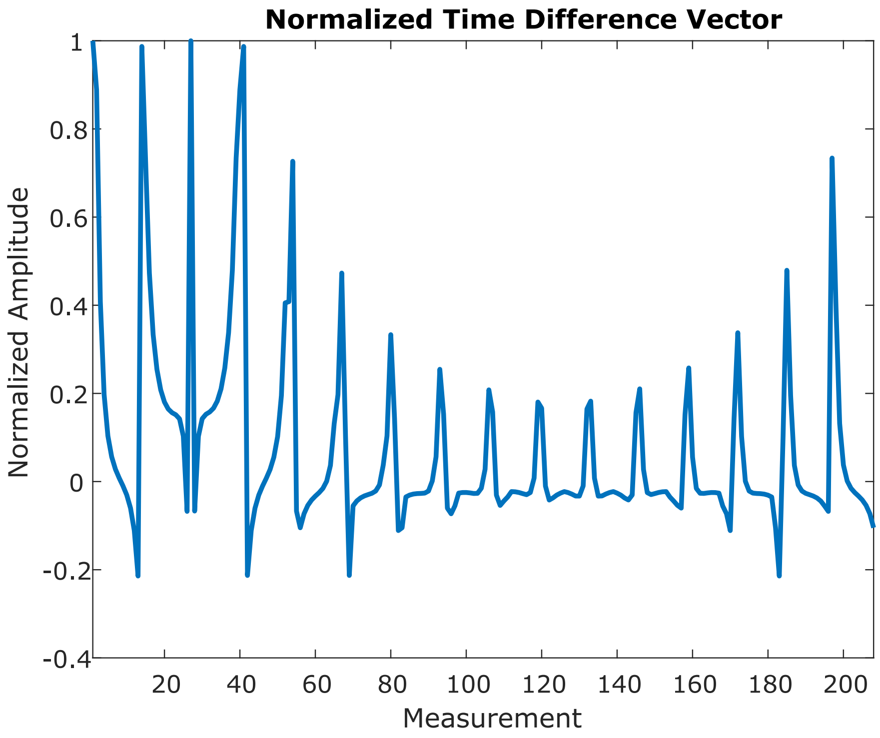

Source: Produced by the Author, 2021.

Figure 6.6 – Forward model used for image reconstruction.

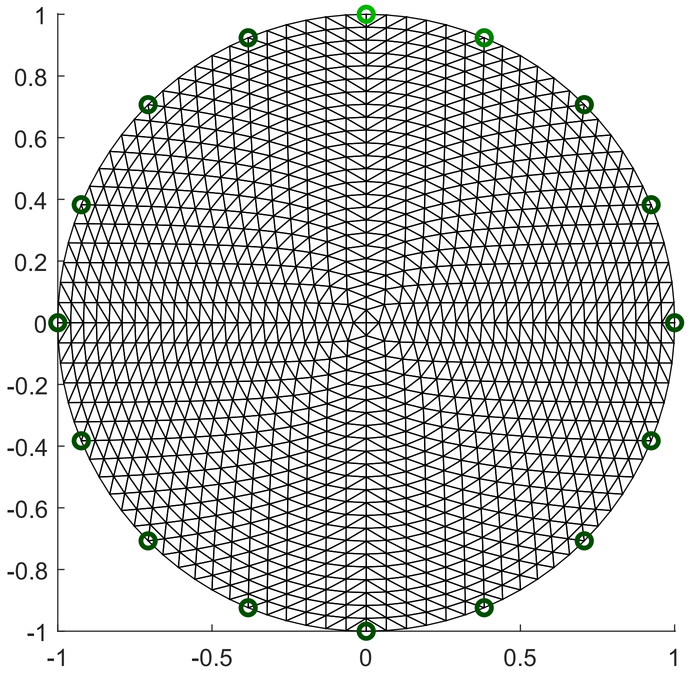

Source: Produced by the Author, 2021.

Two different reconstruction algorithms were implemented for comparison. The first one was the One-Step Gauss-Newton (*GN-One Step*) algorithm proposed by Adler and Guardo (ADLER; GUARDO, 1996). It uses The second one was the Iterative Total Variation Regularization solver proposed by Borsic *et al* (BORSIC et al., 2007). Both algorithms are readily available in EIDORS, in the form of *inv_solve_diff_GN_one_step* and *inv_solve_TV_pdipm* functions, respectively. The hyperparameter in both was set to $0.3 \times 10^{-6}$. The *Iterative TV* algorithm was limited to 5 iterations. Results are shown in Figure 6.7.

Figure 6.7 – EIT images obtained using several reconstruction algorithms.

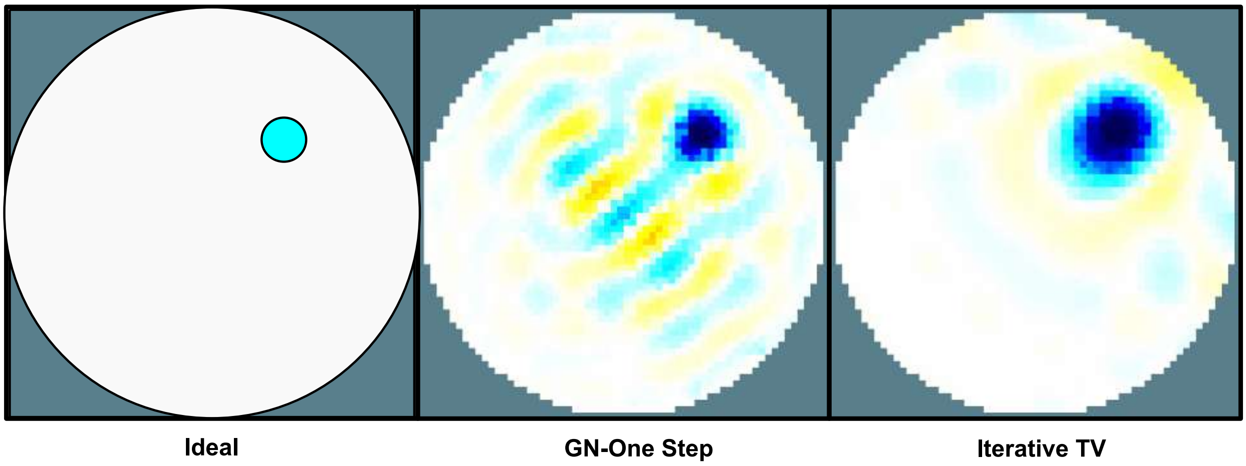

Source: Produced by the Author, 2021.

Both algorithms were able to detect the phantom correctly in terms of position. However, the *GN-One Step* algorithm presented a higher level of image artifacts, especially at the center in the form of conductivity ringing. The *Iterative TV*, on the other hand, presented a lower level of artifacts and better position reconstruction, but the shape was significantly more distorted than the *GN-One Step* case. However, this distortion was caused by the 2D assumption of the image reconstruction. It is clear from Figure 6.1 that the structure is not symmetric in the Z-axis, and both potential and sensitivity fields change with height (Figures 6.3 and 6.4). Therefore, shape distortions are expected. Considering this fact combined with the lower image artifacts and better position tracking performance, the *Iterative TV* algorithm was selected for experimental image reconstruction,

## 6.2 CIRCUIT CHARACTERIZATION

The first stage of the electronic circuit is the Howland source. This circuit is responsible for the excitation signal, which must be a constant amplitude current independent of the load. The differential topology of the Howland should also ensure a symmetrical voltage across the load. Therefore, the Howland circuit was characterized in terms of: transconductance, output impedance and CMRR. Figure 6.8 shows the simulated transconductance of the circuit.

Figure 6.8 – Howland transconductance as function of frequency

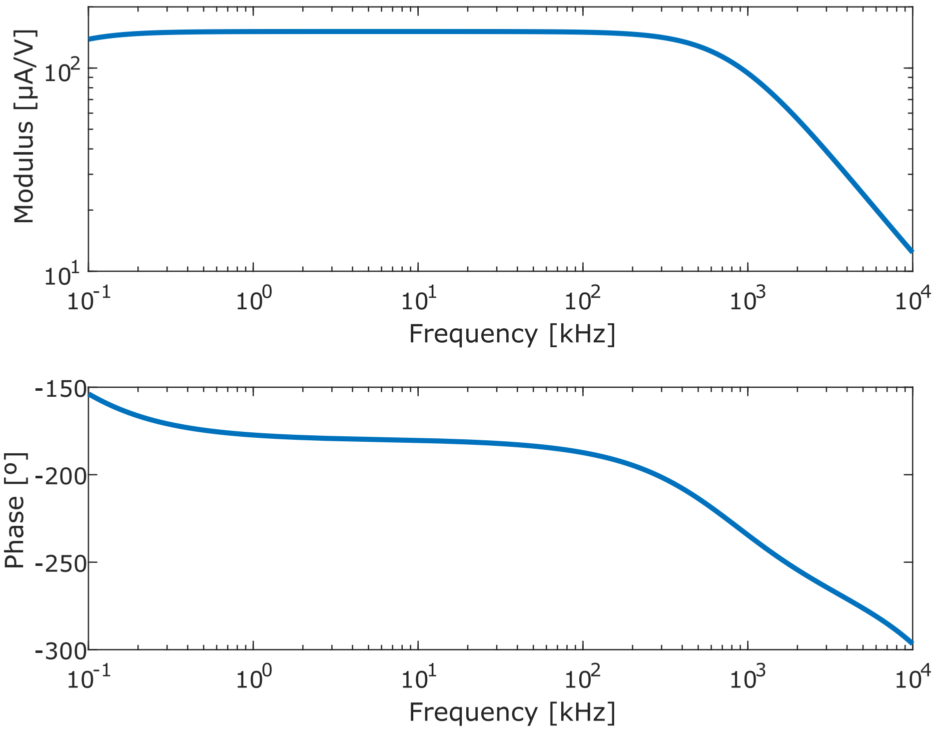

Source: Produced by the Author, 2021.

The transconductance of the designed Howland source is flat for the entire band between 1 kHz and 100 kHz, with modulus equal to $150\mu S$. The phase variation between 10 kHz and 100 kHz is lower than 7°. This shows that the circuit is able to provide stable currents with constant amplitudes within the entire frequency range.

The output impedance tells how much the circuit transconductance will change with the load: larger output impedances result in smaller current variations. The output impedance is shown in Figure 6.9. It can be seen that the output impedance is smaller for lower frequencies. This is due to the coupling capacitors $C_C$ (Figure 5.2. As designed, the peak of output impedance was located at 10 kHz, with absolute value of 5.05 MΩ. The output impedance drops to 2.38 MΩ at 100 kHz. Using the minimum output impedance equation presented by Tucker *et al* (TUCKER; FOX; SADLEIR, 2012), the maximum load variation for a current error smaller than 1 LSB was 1232.9 Ω at 10 kHz and 581.1 Ω at 100 kHz.

Figure 6.9 – Howland output impedance as function of frequency

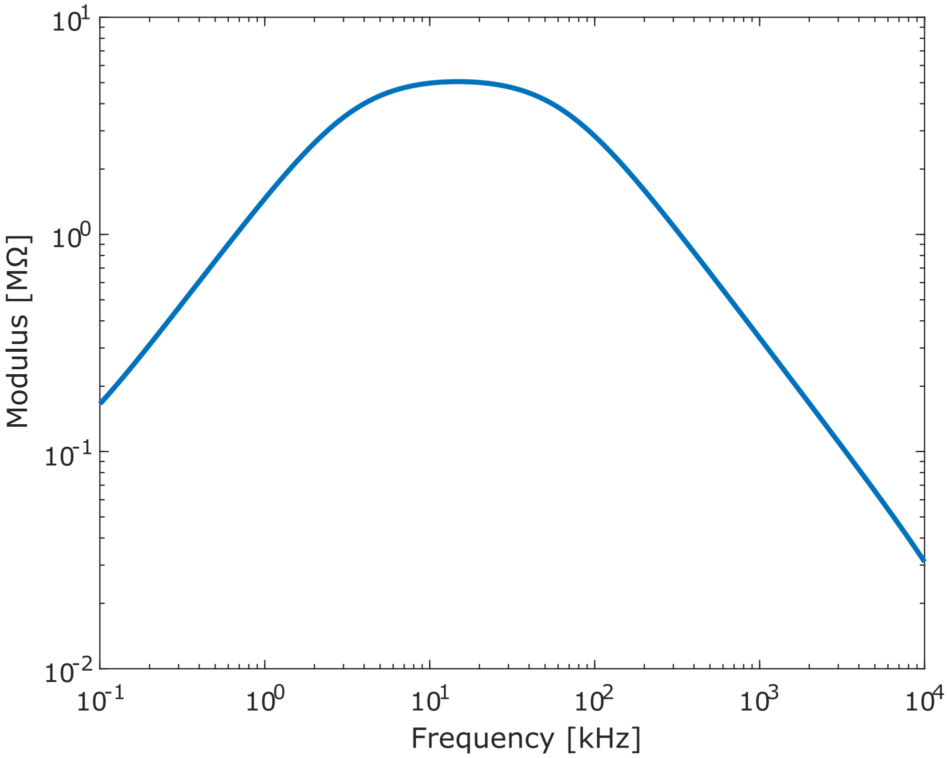

Source: Produced by the Author, 2021.

Finally, the symmetry of the both howland outputs is shown in Figure 6.10 in terms of differential and common-mode voltage, using a square wave at 10 kHz. It can be seen that the differential voltage dominates the signal, and only a few mV of common-mode voltage is delivered to the load. However, some spikes of common-mode voltage can be seen, which are resulted from mismatches in the phase of both outputs. However, the maximum amplitude of these spikes are less then 20 mV, which is 10 times lower than the differential amplitude. Common-mode rejection is essential to improve the noise performance of the circuit, considering that the CMRR of the voltage sensing circuit is not perfect.

The performance of the sensing circuit was also characterized via simulation. As discussed in Section 5.2, a Variable Gain Amplifier (VGA) was used to control the overall gain of the sensing circuit. The gain is selected using an analog voltage between 0.1 V and 1.1 V. The differential gain and phase for several control voltages can be seen in Figure 6.11. As expected, the gain varied from 0 dB to 80 dB with a step of 12.5 mV/dB. Moreover, the frequency response is independent of the gain, which maintains the frequency content of the signal regardless the amplification level.

Figure 6.10 – Common-mode rejection of the Howland Excitation Circuit

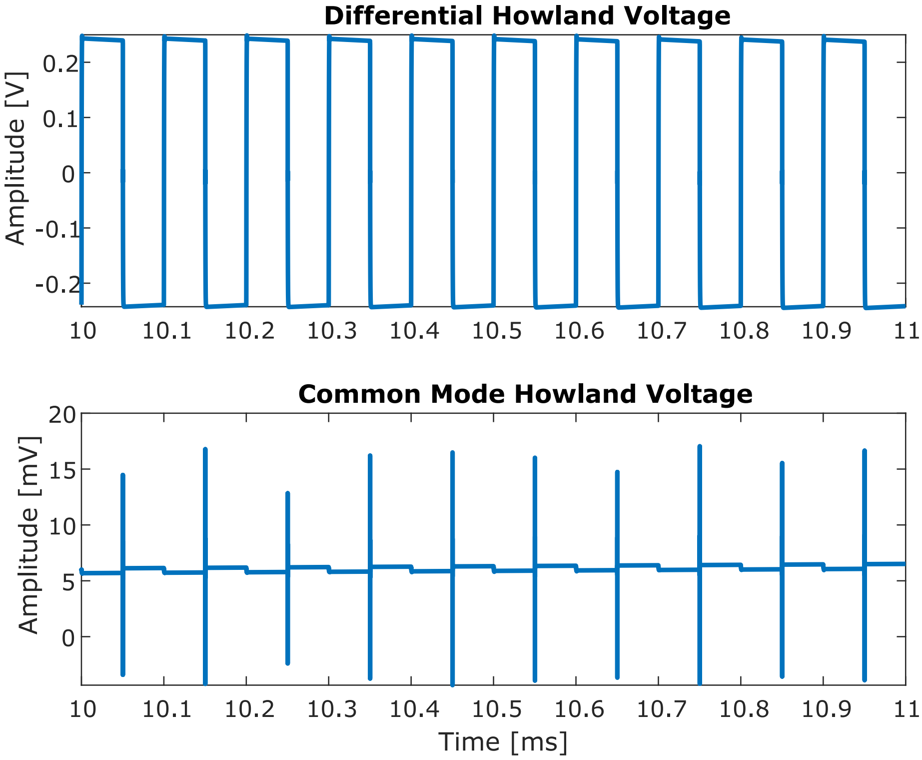

Source: Produced by the Author, 2021.

The response of the anti-aliasing filter is also crucial for proper operation. As discussed in Section 5.2, the circuit is a fourth-order low-pass filter based on the multiple-feedback topology, with cut-off frequency at 1 MHz. The frequency response of the filter can be seen in Figure 6.12. The filter has a gain equal to -1, which is typical for multiple-feedback topologies. Although the Sallen-Key filter topology is more recommended in low-pass filters with unitary gain, it cannot be easily implemented in fully-differential circuits.

Figure 6.11 – VGA transfer function for several gain values.

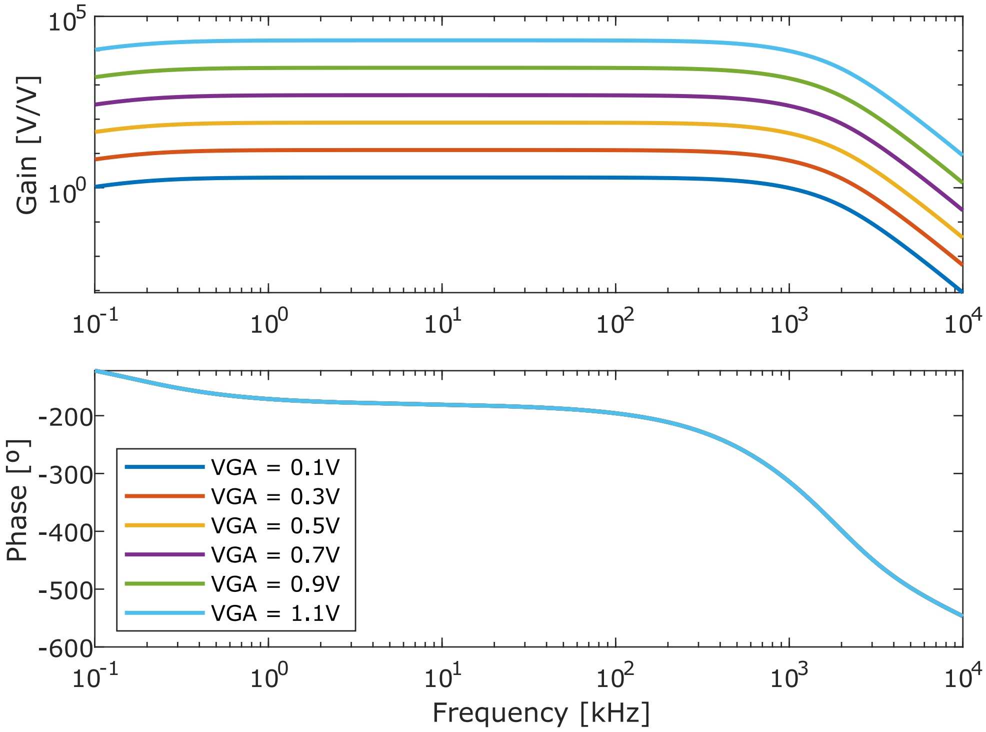

Source: Produced by the Author, 2021.

Figure 6.12 – Transfer function of the anti-aliasing filter.

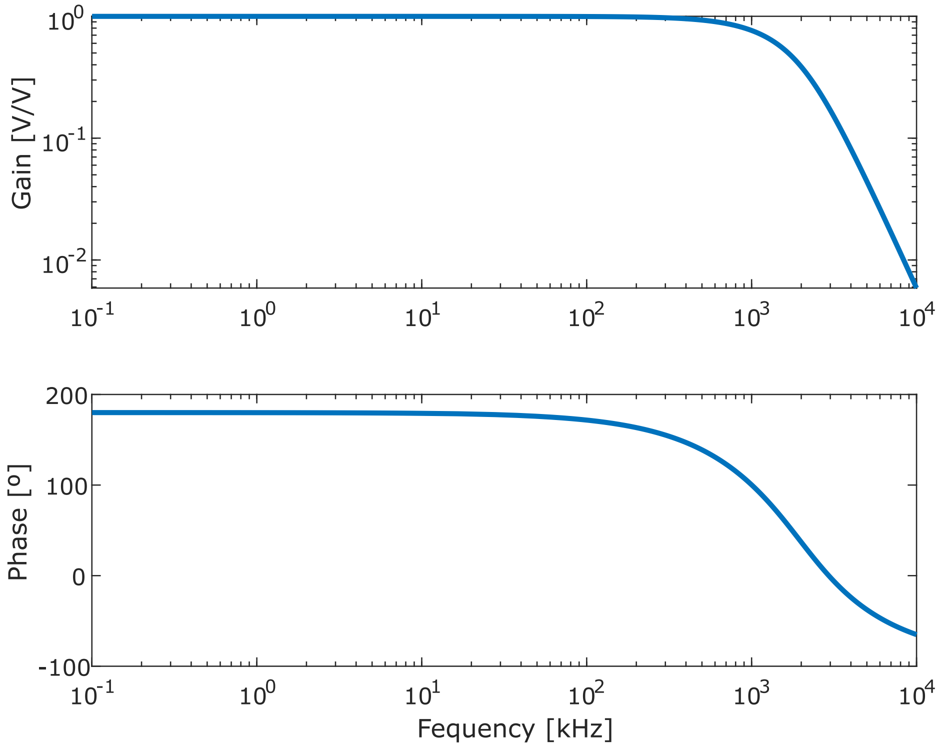

Source: Produced by the Author, 2021.

Finally, the common-mode rejection capability of the sensing circuit was tested. In this simulation, a large common-mode interference was generated and added to the differential signal. The signal of interested was a differential voltage with amplitude equal to 20 mV at 10 kHz. The common-mode interference was composed of one harmonic at 120 Hz with 1 $V_P$, one at 100 kHz with 100 $mV_P$ and one at 1 MHz with 100 $mV_P$. The signal was then amplified by the sensing circuit, with a gain of 40 V/V. It can be seen that only the differential signal was amplified, with the common-mode signal being completely rejected by the circuit. Considering that most of the electrical interference affects the circuit in a common-mode fashion, it is expected that the differential signaling strategy will eliminate most of the noise in the experimental setup.

Figure 6.13 – Extraction of differential voltages from an input corrupted by common-mode voltage. The input contained common-mode harmonics at 120 Hz ($V_{cm} = 1V$), 100 kHz ($V_{cm} = 100mV$) and 1 MHz ($V_{cm} = 100mV$). The differential voltage have $V_d = 20mV$ at 10 kHz.

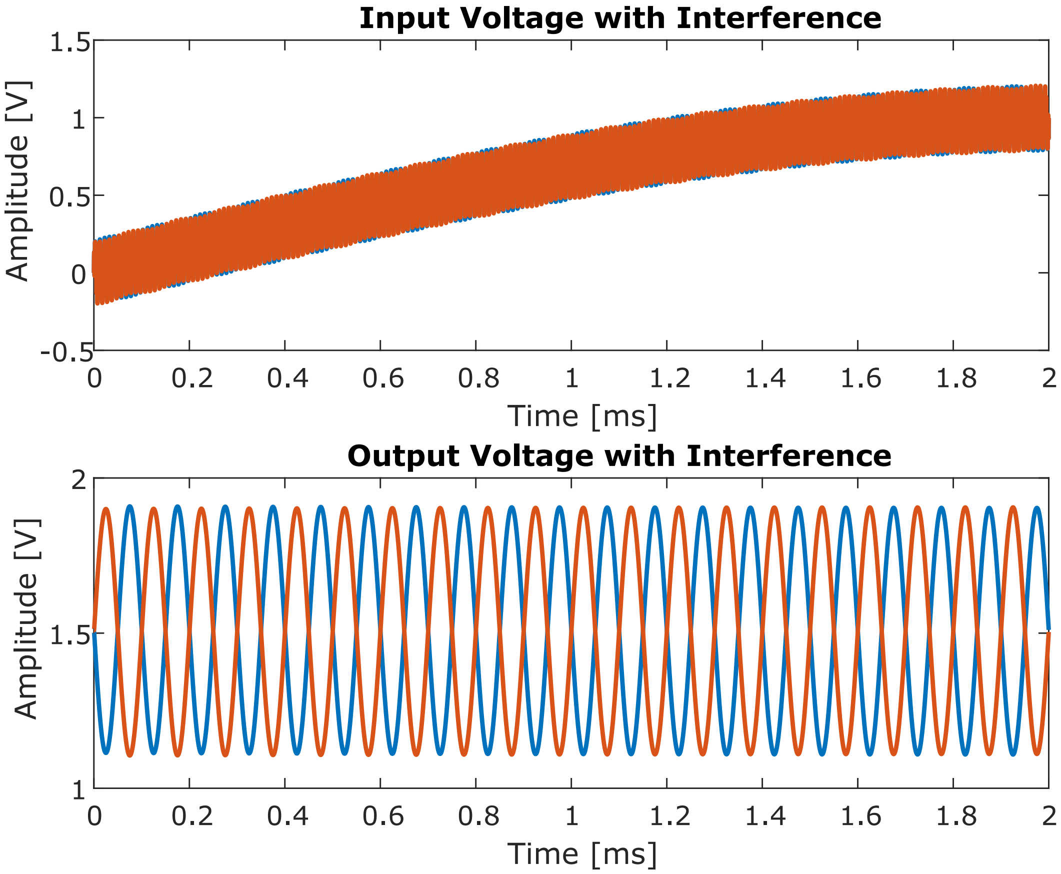

Source: Produced by the Author, 2021.

## 6.3 INTEGRATION BETWEEN EIDORS AND PSPICE SIMULATIONS

The EIDORS library contains all the image reconstruction functions implemented in this thesis, whereas the circuit simulations were all performed using the PSPICE software. In this thesis, an integrated framework is proposed, allowing reliable simulations of the EIT process, taking into account the reconstruction methods, electrode geometry, circuit non-idealities and analog-to-digital conversion limitations. The working flow of the integrated simulation was described in Figure 6.2 following the EIDORS + PSPICE branch. Figure 6.14 describes the data sharing process of the framework.

Figure 6.14 – Integration between EIDORS and PSPICE simulations

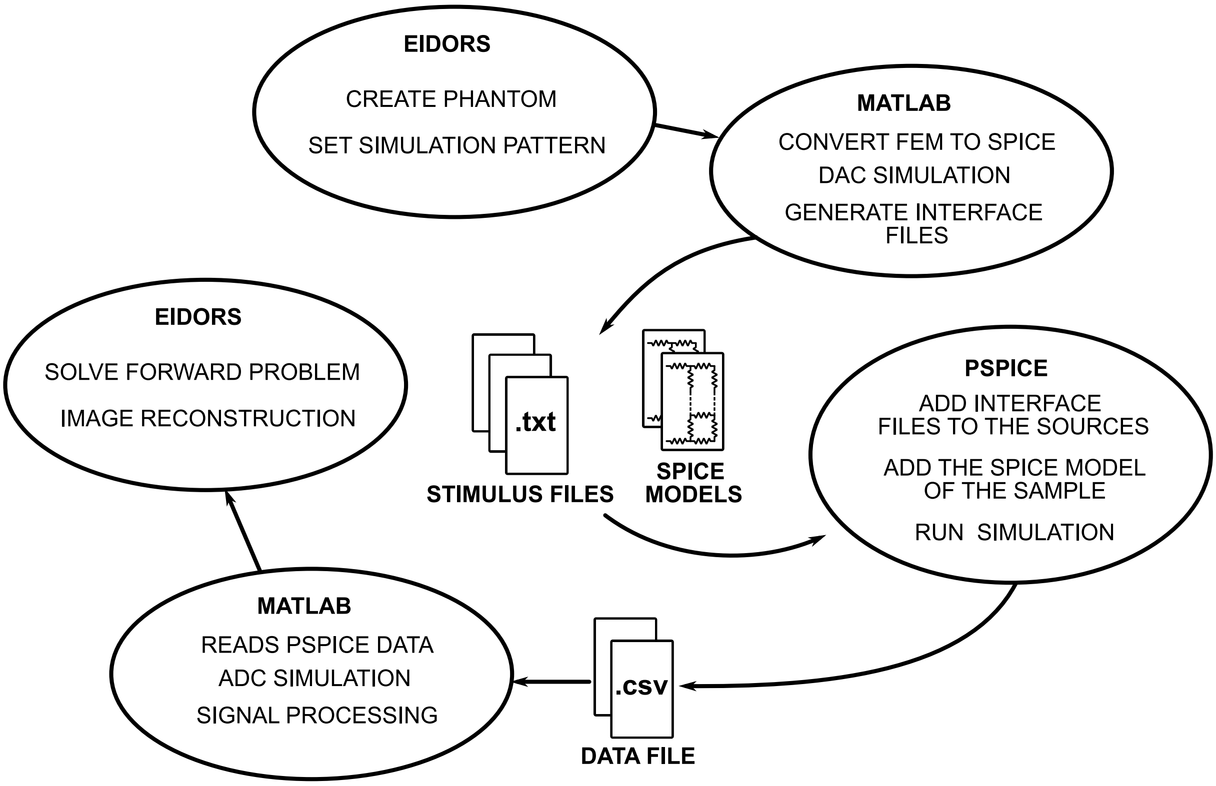

Source: Produced by the Author, 2021.

The process is further described below:

- A FEM phantom object, representing the measured sample, is generated using the NETGEN mesh generator. A stimulation pattern is also generated using EIDORS, containing all the measurement sequence that defines the EIT protocol;

- The FEM phantom is converted to a passive SPICE model using the *eit_spice()* function. A DAC model developed in MATLAB generates a sine wave to be used as excitation signal, and this signal is stored in a stimulus file. Moreover, a voltage command sequence for the commutation module is automatically generated from the stimulation pattern structure, which is also stored in .txt stimulus files.

- At the PSPICE side, the stimulus files are linked to piece-wise linear (PWL) sources. These sources generate voltages from the .txt values, and are used to drive both the excitation and commutation circuits. The spice netlists containing the phantom information are linked to PSPICE components.

- A transient PSPICE simulation is performed for both the homogeneous and inhomogeneous samples, covering the whole EIT scan. The resulting data vectors are saved in CSV files.

- A MATLAB interface automatically reads the CSV files to obtain the PSPICE data. An ADC MATLAB model reads the PSPICE data and converts it to a digital form according to the pre-defined sampling frequency and number of bits. This is done to simulate the ADC discretization process. However, the raw PSPICE data is already discretize, with an irregular and much smaller sampling period. The ADC model uses linear interpolation to approximate the PSPICE data to a truly analog signal.

- The signal processing consists of obtaining the value of the harmonic at the 10 kHz frequency using FFT. This harmonic is taken for each injection/sensing pair, and the absolute value is stored in a data vector.

- The data vectors of the homogeneous and inhomogeneous samples are used for image reconstruction. The forward FEM model was the same as in Figure 6.6. The algorithms implemented were the same used in Section 6.1.

A simulation was performed using the same specifications described in Section 6.1 and the circuit described in 5. Figure 6.15a shows the transient simulation of the output voltage of the sensing circuit during the entire EIT sequence. After discretization and processing, the data vector shown in Figure 6.15b was obtained. When compared to the ideal data vector in Figure 6.5, it can be seen that the data was greatly affected by the circuit non-idealities and discretization noise, but the overall shape of the vector remained the same.

Finally, the reconstructed images using the integrated framework can be seen in Figure 6.16, using both reconstruction algorithms implemented in Section 6.1. The *GN-One-Step* algorithm was not able to reconstruct the image, probably due to the high noise level introduced by the circuit and the discretization process. The *Iterative TV*, on the other hand, was able to reconstruct the spheroid. However, compared to Figure 6.7, the position error is significantly higher, which can be attributed to the circuit non-idealities. Nevertheless, the integrated

Figure 6.15 – PSPICE measurements during the EIT protocol (a) and the resulting data vector obtained (b).

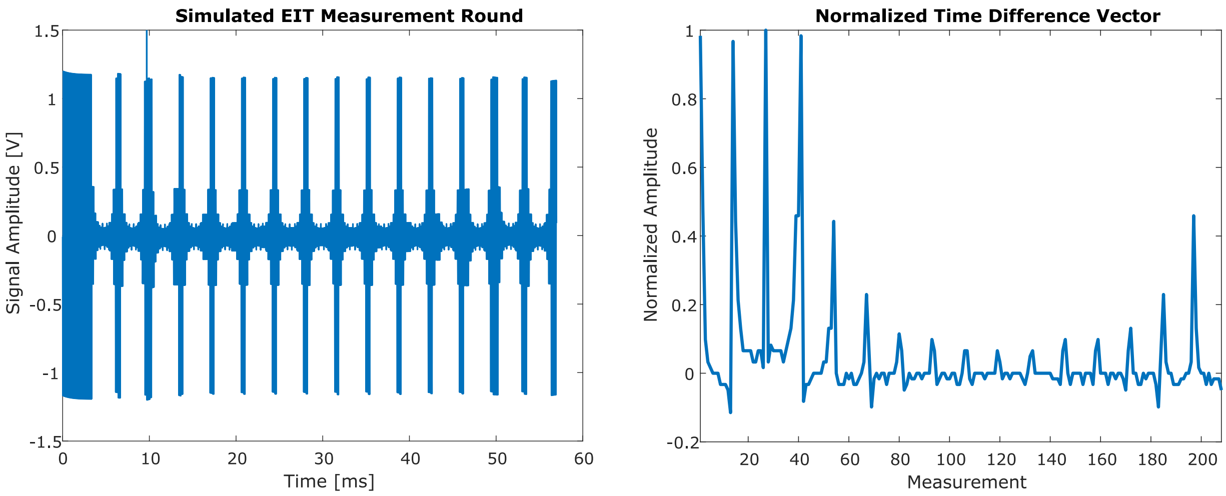

(a) (b)

Source: Produced by the Author, 2021.

framework provided a more reliable prediction of the system performance in real-life, and can be used in the future as a powerful development tool to verify how each system component, such as excitation circuit, electrode configuration and ADC resolution, affects the EIT image.

Figure 6.16 – EIT images obtained from the EIDOR/PSPICE simulation interface using several reconstruction algorithms.

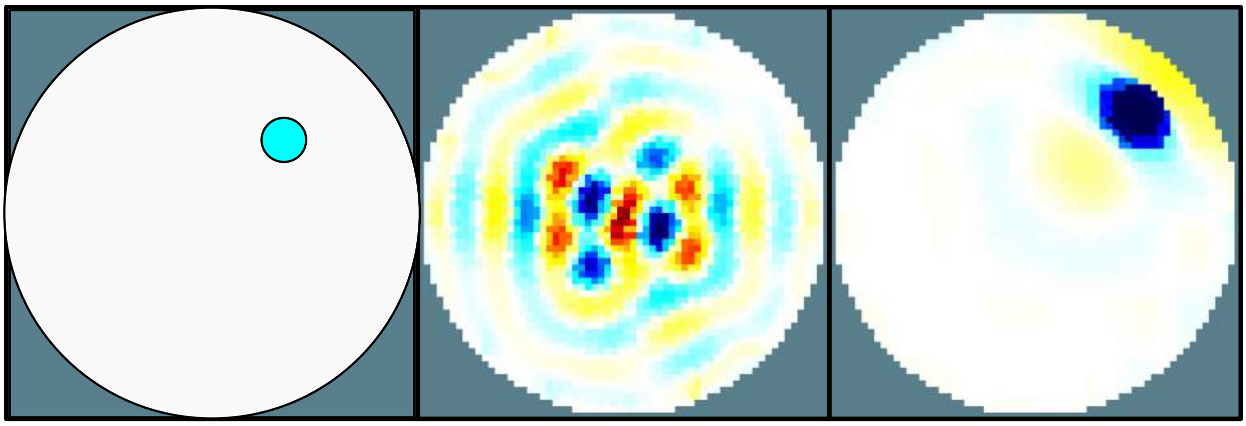

**Ideal** **GN-One Step** **Iterative TV**

Source: Produced by the Author, 2021.

# 7 EXPERIMENTAL RESULTS AND DISCUSSIONS

## 7.1 3D BIOPRINTING

The gelatin bed was prepared using a petri dish filled with the gelatin/$CaCl_2$ mixture, which as left in the fridge at 4°C for gelification. After the gelatin bed was ready, the bioink was prepared. The alginate/gelatin mixture was stored inside the printing syringe and left to cool down at room temperature for 30 minutes. The petri dish was fixed to the printer bed using double-sided tape, to prevent movement. After the bioprinting setup was finished, the Z-axis was manually calibrated to ensure that the distance between needle and gelatin bed was the same in every point and enough to allow bioink flow. The first bioprinted structure was an hexagon, showed in Figure 7.1.

Figure 7.1 – Hexagon structure with dimensions (a) and printed structure (b).

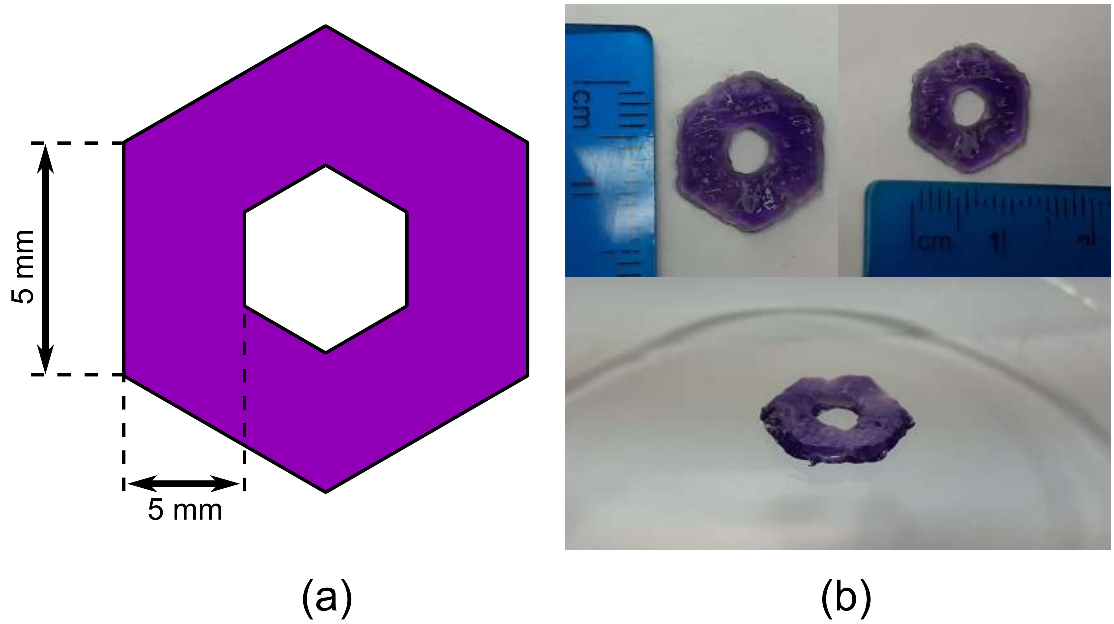

Source: Produced by the Author, 2021.

The design hexagon structure have a total length of 15 mm, internal thickness of 5.0 mm and 3.0 mm of height. After cross-linking, the printed part showed mechanical stability, allowing hand manipulation without breaking or compromising the structure. The external geometric fidelity was enough to provide visual shape identification, but the part presented several printing defects. Firstly, the internal hexagon-shaped region assumed a circular geometry, reducing shape fidelity. Secondly, the height of the printed structure dropped significantly , caused by deformations of the bioink filaments during the printing process. Both problems were caused by the limited properties of the bioink, whose rheological properties did not provide enough mechanical stability for the filament. Rheological properties can be improved in the future by selecting the optimum ratio between gelatin and alginate (TASOGLU; DEMIRCI, 2013) or by incorporating different components to the bioink, such as carboxymethyl cellulose (CMC) (HABIB et al., 2018).

The second printed structure was a bone-shaped part (Figure 7.2). Although the geometry is not completely biologically accurate, it was used to verify the capability of printing round shapes and parts with large aspect ratio. The printer was able to print the round structures accurately, as well as the weight and length of the bone. However, the height was not completely uniform due the deformation of the top layers before cross-linking. Also, the bioink spreaded significantly at the edges of the bone. Both problems can also be explained by the limited performance of the implemented bioink.

Figure 7.2 – Bone-shaped structure with dimensions (a) and the printed result (b).

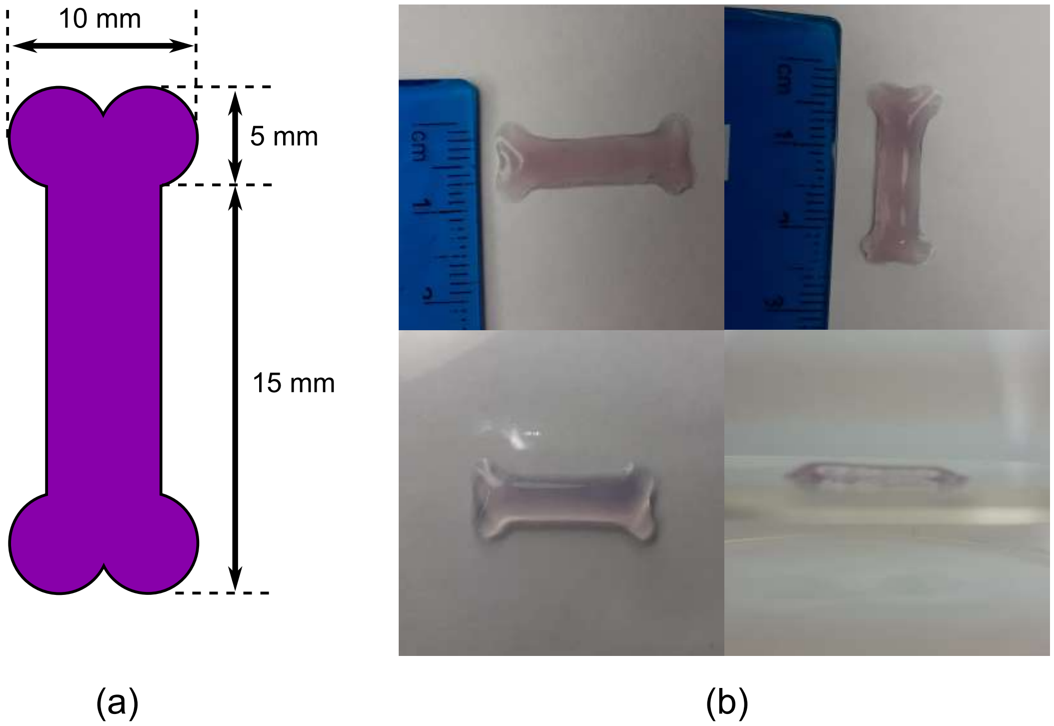

Source: Produced by the Author, 2021.

Porous scaffolds are important structures in bioprinting, as they provide better distribution of nutrients and other substances. To verify the printer's ability to manufacture porous scaffolds, a rectangular grid structure was designed (Figure 7.3). Each pore had 3 mm of diagonal length, and the total height of the structure was 3 mm. The print result presented a high level of shape fidelity, preserving the porous geometry and the dimensions. Moreover, the part was mechanically stable after crosslinking, allowing hand manipulation and even providing a moderate level of elasticity due to the grid structure.

Overall, the bioprinted parts presented an acceptable level of printability, shape fidelity and mechanical stability for the purposes of this thesis, which is the validation of EIT for

Figure 7.3 – Porous scaffold with dimensions (a) and the printed part (b)

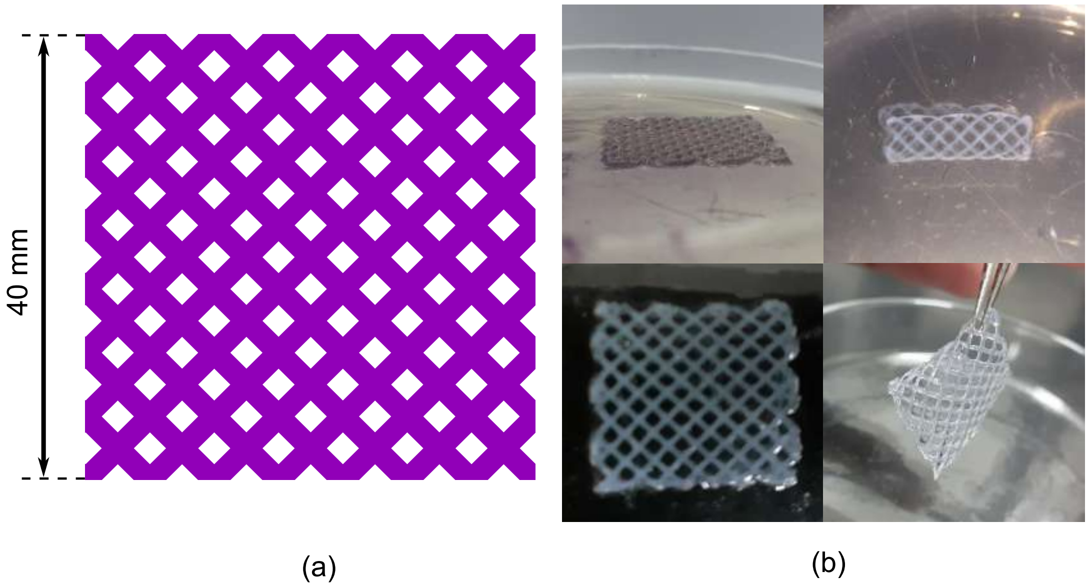

Source: Produced by the Author, 2021.

4D bioprinting. Moreover, the developed machine was able to produce flat porous scaffolds, which can be implemented in applications requiring structural conformability, such as skin regeneration. However, the applicability of the printer in actual biomedical applications is still significantly limited, especially due to the degradation in shape fidelity caused by the rheology of the bioink. Future work should be performed to tune the bioink properties.

## 7.2 CIRCUIT CHARACTERIZATION

Each stage of the designed system described in Chapter 5 was analysed in terms of electrical performance, to validate its applicability in impedance sensing and EIT. Moreover, this analysis can provide powerful insights to troubleshoot possible problems limitations in the imaging outcomes. This section presents the electrical characterization of the excitation circuit, measurement stage, communication with the host and electrode array.

### 7.2.1 Excitation Circuit

The excitation circuit should provide a constant amplitude signal without distortion for several different loads values. This ensures a consistent sensitivity field during the imaging process. Therefore, the output current of the circuit was analysed. Current was measured using the oscilloscope connected to both sides of the load. The differential voltage divided by the load value corresponded to the current. The output current for a square-wave input signal (3.3 $V_{p-p}$ at 10 kHz) and load equal to 3.3 $k\Omega$ is shown in Figure 7.4.

Figure 7.4 – Output current of the excitation circuit for a 3.3 $k\Omega$ load in the frequency domain (a) and time domain (b).

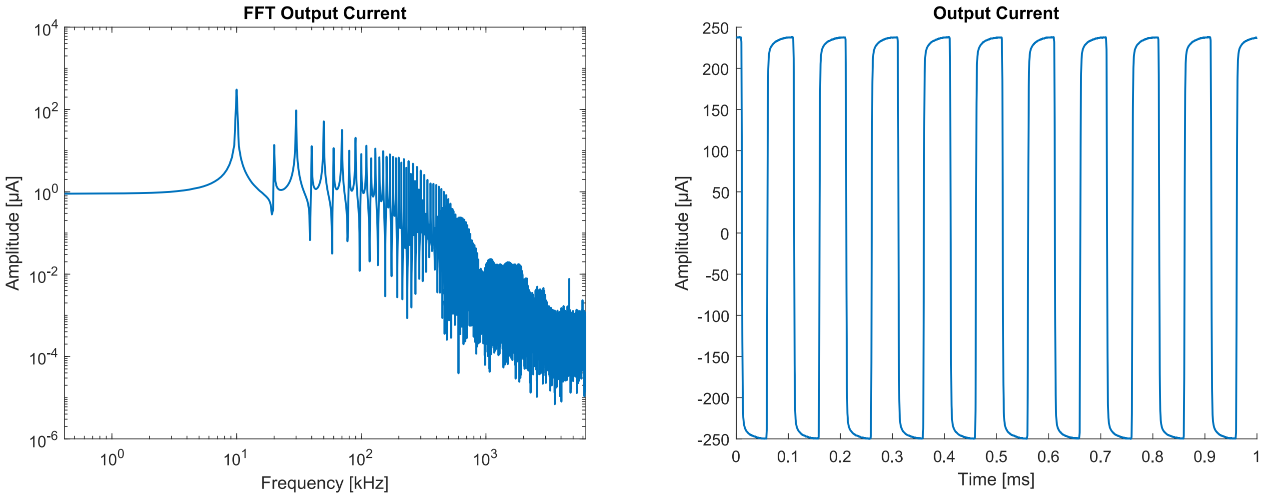

(a) (b)

Source: Produced by the Author, 2021.

It can be seen that the average level of the output current is equal to zero, which prevents DC excitation of the sample. Also, the fundamental harmonic is centered in 10 kHz, as expected, with amplitude of 304.3 $\mu A$ . Despite the noise, the largest harmonics were located at odd integer multiples of the fundamental harmonic, which is expected in a square-wave signal. These harmonics and the fundamental signal were used to estimate the signal response in frequency for several loads. Figure 7.5 shows the output current curves for different loads and frequencies.

As expected, the current level drops with the increase in load. This drop is lower than 4% for loads below 3.3 $k\Omega$. Although this may be unacceptable in precision bioimpedance applications, difference EIT is more robust for current dependency on the load. This is because the impedance seen by the excitation circuit is a series combination between electrode impedance and sample impedance. The electrode impedance is several orders of magnitude higher than the sample impedance (see Subsection 7.2.4), thus a large variation in sample impedance results in a small variation in the overall impedance seen by the current source, causing a negligible variation in current. Therefore, a 4% drop in current for a 3.3 $k\Omega$ load is acceptable in TDEIT.

However, the output current also drops with frequency. The current at 100 kHz dropped 6.5% for the 470 $\Omega$ and more than 32% for the 3.3 $k\Omega$ load when compared to the 10 kHz harmonic. This can degrade significantly the performance of the system in FDEIT. A calibration method was then implemented to reduce the effects of circuit variation in frequency. This method is described in Section 5.5. Nevertheless, the sensitivity field is lower at 100 kHz.

Figure 7.5 – Output current response for several loads.

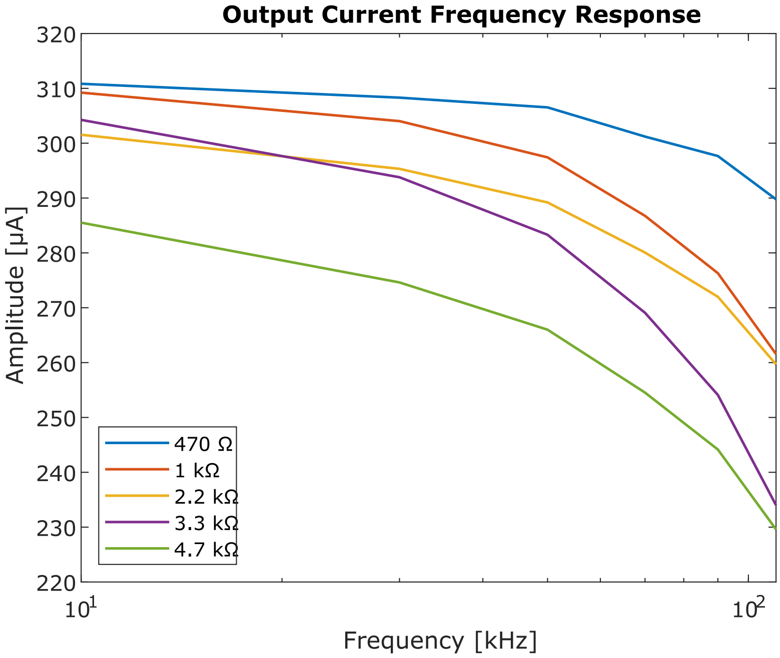

Source: Produced by the Author, 2021.

Finally, the variation of the output current with the channel was analysed. This analysis is important to ensure that each channel receives the same current amplitude, despite mismatches in stray capacitances and parasitic impedances. Figure 7.6 shows the current error for each electrode pair with 10 kHz and 100 kHz. The maximum error in 10 kHz is smaller than 1%, which shows consistency between channels. As expected, the current error increases at 100 kHz due to the higher effect of stray capacitances. However, even for 100 kHz the current error remained below 2%.

Figure 7.6 – Variation of the Output Current with the Injection Channel.

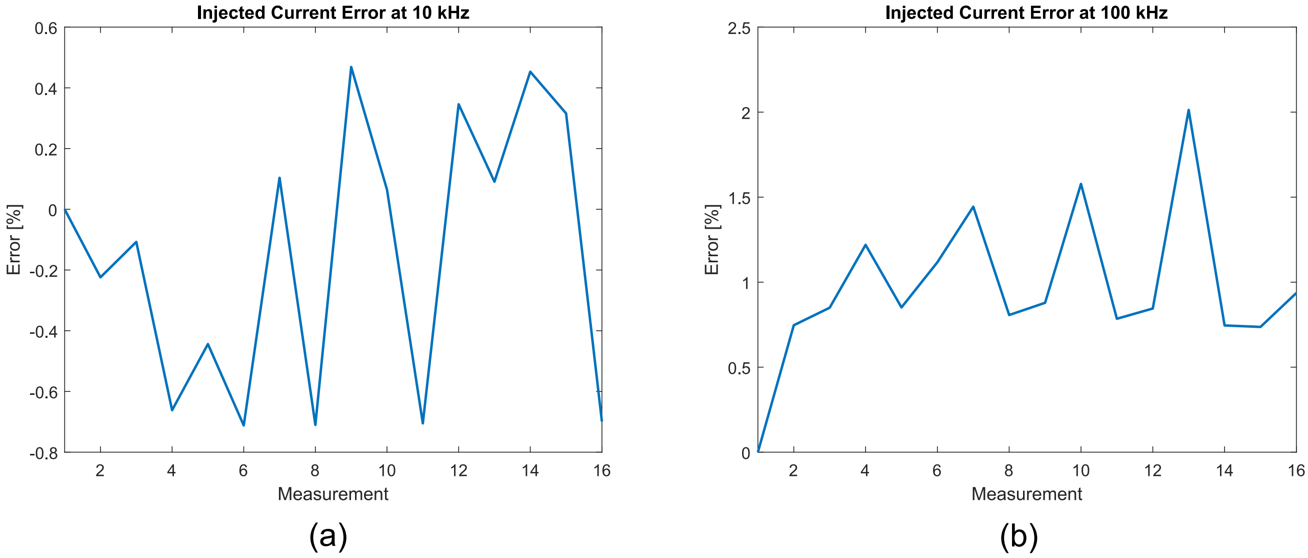

(a) (b)

Source: Produced by the Author, 2021.

### 7.2.2 Measurement Stage

The measurement stage was characterized in terms of channel variation, common-mode noise and differential noise. The error for different channels was measured using a resistive phantom composed of 16 identical 1 $k\Omega$ resistors in a ring configuration (Figure 7.7). This configuration ensures that all resistors external to the injection pair receive the same current, so the voltage drop is identical in a perfect measurement system. Any deviation between channels will then be caused by the system itself.

Figure 7.7 – Resistive phantom implemented to detect measurement error between channels.

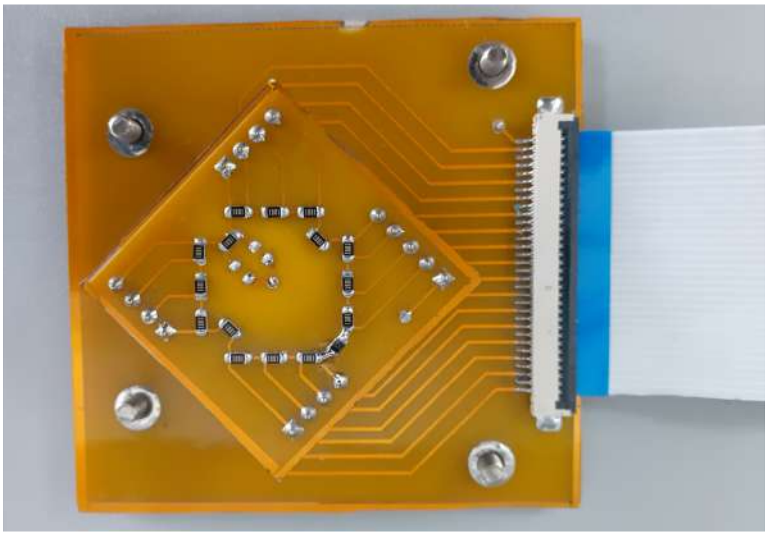

Source: Produced by the Author, 2021.

The measured voltages were obtained using the VGA system with three different gains. The measured signal was then divided by the gain so all voltages are referred to the input. The measurement error for each channel is shown in Figure 7.8.

Measurement errors at 10 kHz are smaller than 2.5%, and the variability profile between measurements and gains suggests that it is caused by noise (analog noise and discretization noise). On the other hand, the 100 kHz varies drastically, with errors reaching 70%, which can completely degrade an EIT image. Fortunately, this variation is independent on the gain, suggesting that the error occurs before the signal reaches the VGA. In fact, it is reasonable to assume that the error comes from the stray capacitances of the commutation system and flat cable. These capacitances can vary greatly from channel to channel, which explains why it happens in higher frequencies and why it is independent on the VGA gain. Because this variation is constant, a calibration vector can be calculated in order to correct the voltages in actual measurements. The calibration vector was created using the measurements of Figure 7.8 and applied to the results of Section 7.3.

Figure 7.8 – Error between measurement channels for 10 kHz and 100 kHz.

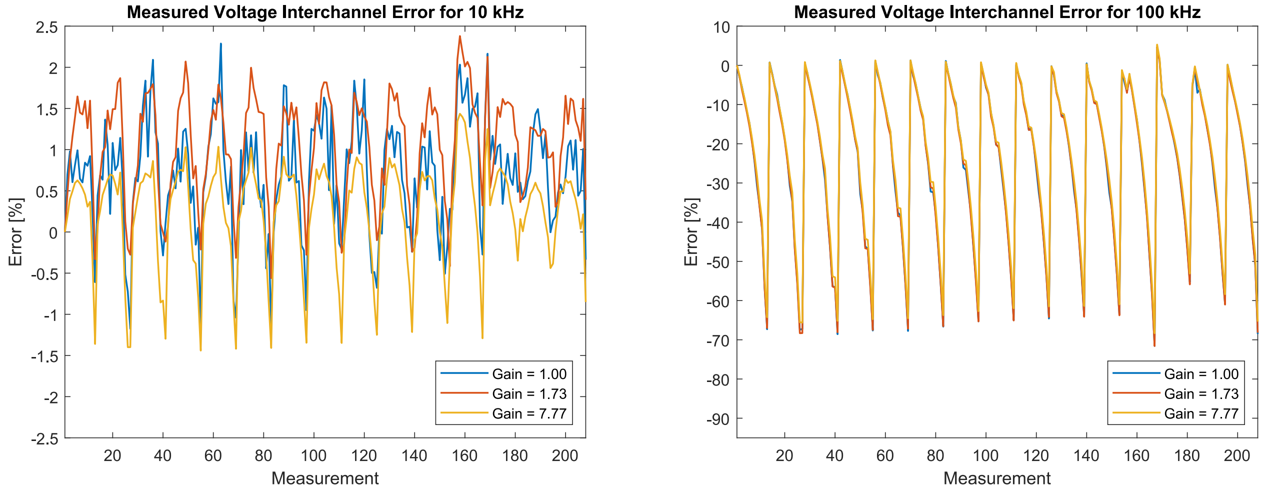

(a) (b)

Source: Produced by the Author, 2021.

Noise was measured at the differential input of the ADC. To analyse the benefits of implementing differential ADC instead of single-ended, figure 7.9 compares the single-ended noise with the differential. The single-ended noise was significantly higher than the differential, showing that even though the fully-differential signaling approach was able to eliminate most of the common-mode noise, differential ADCs are still necessary for further noise optimization. The single ended power spectrum density (PSD) , in a bandwidth of 2 MHz, was equal to 741.8 $nV/\sqrt{Hz}$, while the differential counterpart remained below 173.7 $nV/\sqrt{Hz}$.

Figure 7.9 – Differential and single-ended output noise for a VGA gain of 0 dB.

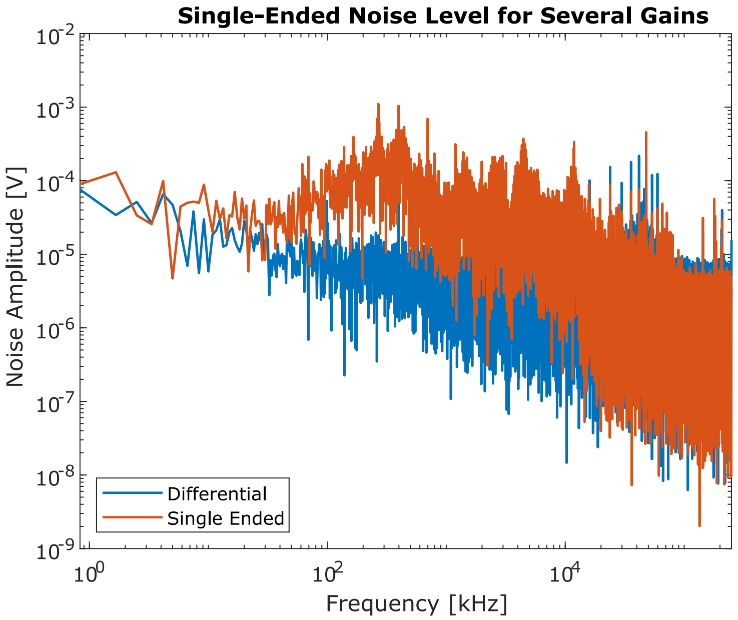

Source: Produced by the Author, 2021.

To analyze the effects of VGA gain on the overall noise, the output noise was measured for several VGA gains. As expected, the output noise increases with the gain (Figure 7.10), but with a slope smaller than the increase in gain. For instance, the PSD increased less than 0.8 $\mu V/\sqrt{Hz}$ for a gain variation of 35 V/V. This means that the signal-to-noise ratio decreases with the increase in gain, as the desired signal grows faster than the noise.

Figure 7.10 – Total spectrum of output noise (a) and the total PSD (b) for several VGA gains.

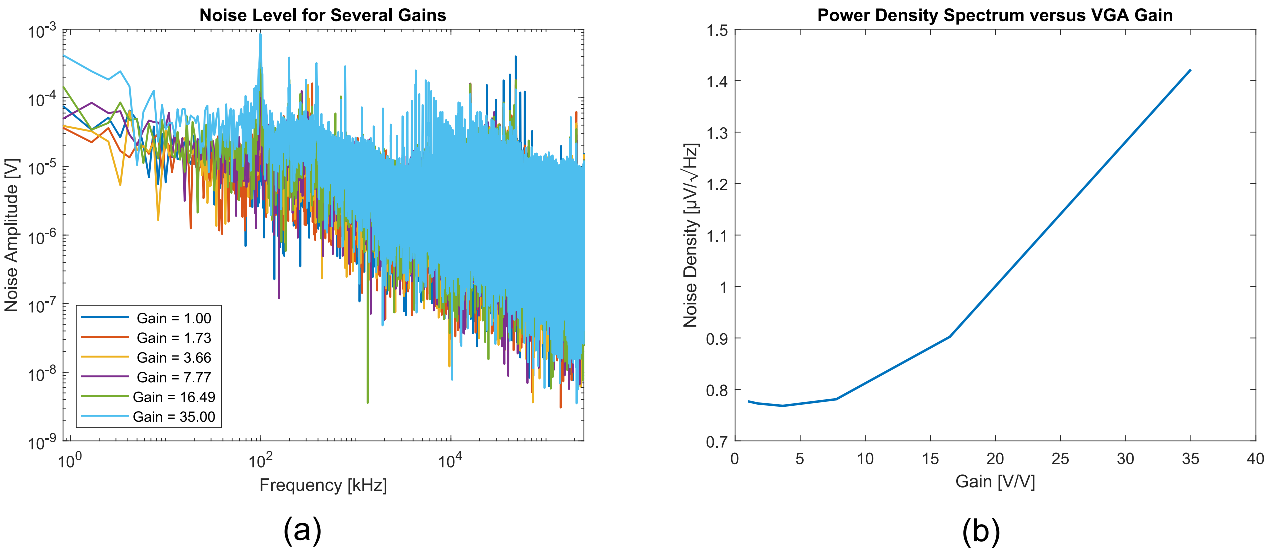

Source: Produced by the Author, 2021.

### 7.2.3 Host Communication

The system was designed to operate with a frame rate of 7.37 fps using 10 kHz and 23.8 fps using 100 kHz (Section 5.3). However, the host communication interface was implemented using MATLAB's function called *serialport()*. This function is not optimized for real-time COM applications, which resulted in a latency of 0.02 seconds per measurement. Due to the significantly high latency in host communication, all images were obtained offline. This problem can be readily solved by optimizing the serial communication process, using python interfaces or faster protocols. Future upgrades in the system will focus on true real-time operation.

### 7.2.4 Electrode Impedance

The electrode impedance of the sensor was measured using the HF2IS Impedance Analyzer (Zurich Instruments). The sensor was filled with a saline solution of 1.5 S/m to act as background media. This conductivity is based on the culture media conductivity reported by

Wu (WU, 2020). The HF2IS Analyzer was connected to electrodes 1 and 8, which are located at opposite sides of the array, forming a bipolar configuration. Bipolar measurements can sense the interface impedance in series with the sample impedance (GRIMNES; MARTINSEN, 2011).

Assuming the electrode impedance is much higher than the sample impedance, which is expected by using gold electrodes due to the ionic double-layer (GRIMNES; MARTINSEN, 2011), the measured impedance can be approximated to the interface impedance of electrode 1 in series with the interface impedance of electrode 8. Considering the saline homogeneous and the gold electrodes identical, the interface impedance can be estimated as half of the measured impedance. The resulting electrode interface impedance is shown in Figure 7.11, for frequencies between 100 Hz and 1 MHz.

Figure 7.11 – Gold electrode interface impedance.

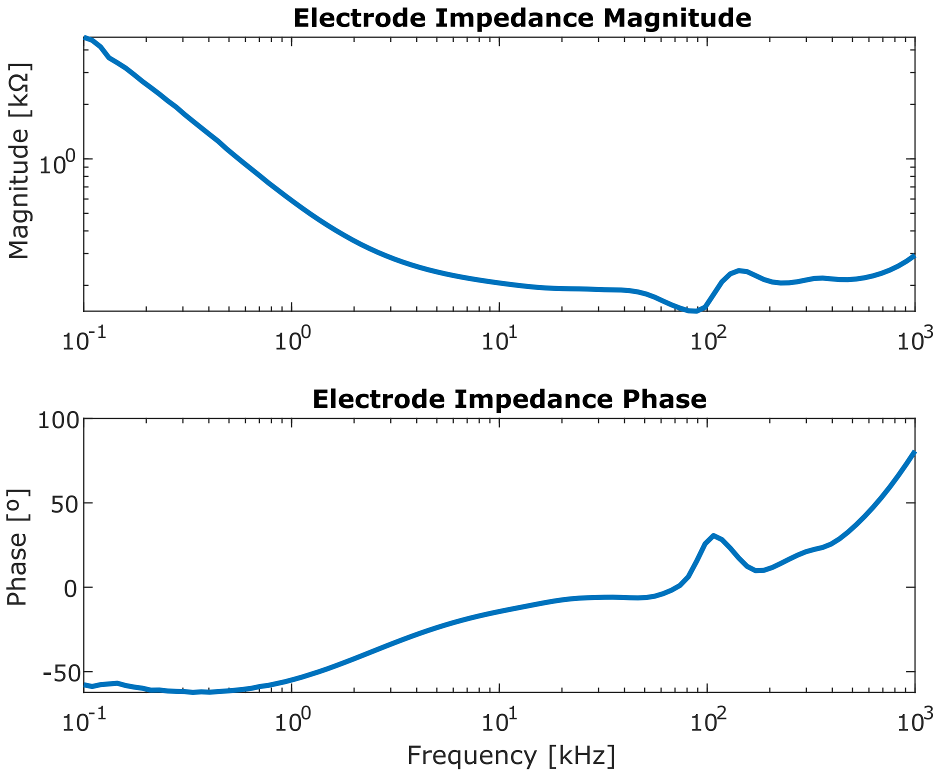

Source: Produced by the Author, 2021.

Different from copper, gold is quite inert in contact with electrolytes. Therefore, there is no reaction at the electrode site, and thus no actual charge is exchanged between gold and electrolyte. This defines a polarizable electrode (GRIMNES; MARTINSEN, 2011), that blocks DC current and allows AC currents resulted from charge displacement. Polarizable electrodes present a high impedance that drops with frequency (GRIMNES; MARTINSEN, 2011). Therefore, Figure 7.11 confirms that the gold electrospinning process was successful. Moreover, the measured electrode impedance was equal to 204.7 Ω at 10 kHz and to 144 Ω at

100 kHz. The excitation circuit sees this impedance doubled (two electrodes), so the maximum load is equal to 409.4 Ω, which is within the optimal range of the circuit (subsection 7.2.1).

## 7.3 EIT IMAGING OF PHANTOMS

This section shows the EIT results for organic, inorganic and bioprinted samples using both TDEIT and FDEIT methods. To mimic scaffolds with cells, different pieces of vegetables (carrot and apple) were used. All images were reconstructed using the *Iterative Total Variation Regularization* solver (BORSIC et al., 2007), set to 5 iterations, first-order forward solver and hyper-parameter equal to $0.36 \times 10^{-6}$.

### 7.3.1 Impedance Analysis of Samples

Both TDEIT and FDEIT measure the difference in conductivity compared to the background. Therefore, the electrical impedance of samples must be different from the saline, otherwise no image can be obtained. The impedance of the samples were measured using a tetrapolar sensor, to reduce cable and electrode effects (GRIMNES; MARTINSEN, 2011), composed of gold electrodes in a fixed planar configuration showed in Figure 7.12.

Figure 7.12 – Electrode probe used for conductivity measurements.

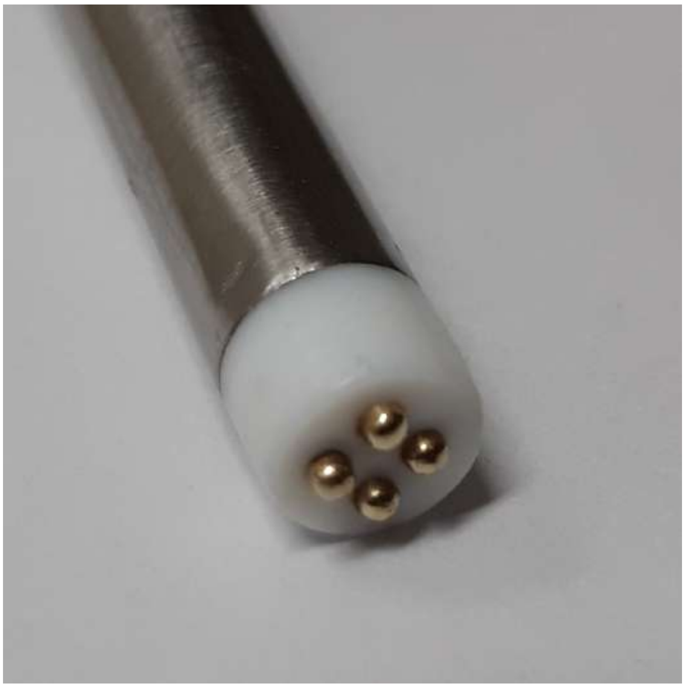

Source: Produced by the Author, 2021.

Because the electrode configuration is fixed, the probe factor remains the same for all samples, allowing comparison. Figure 7.13 shows the impedance curves of each sample compared to the background saline (1.5 S/m). All data was calibrated using a resistive load to eliminate equipment error in magnitude and phase.

Figure 7.13 – Impedance measurement obtained from samples.

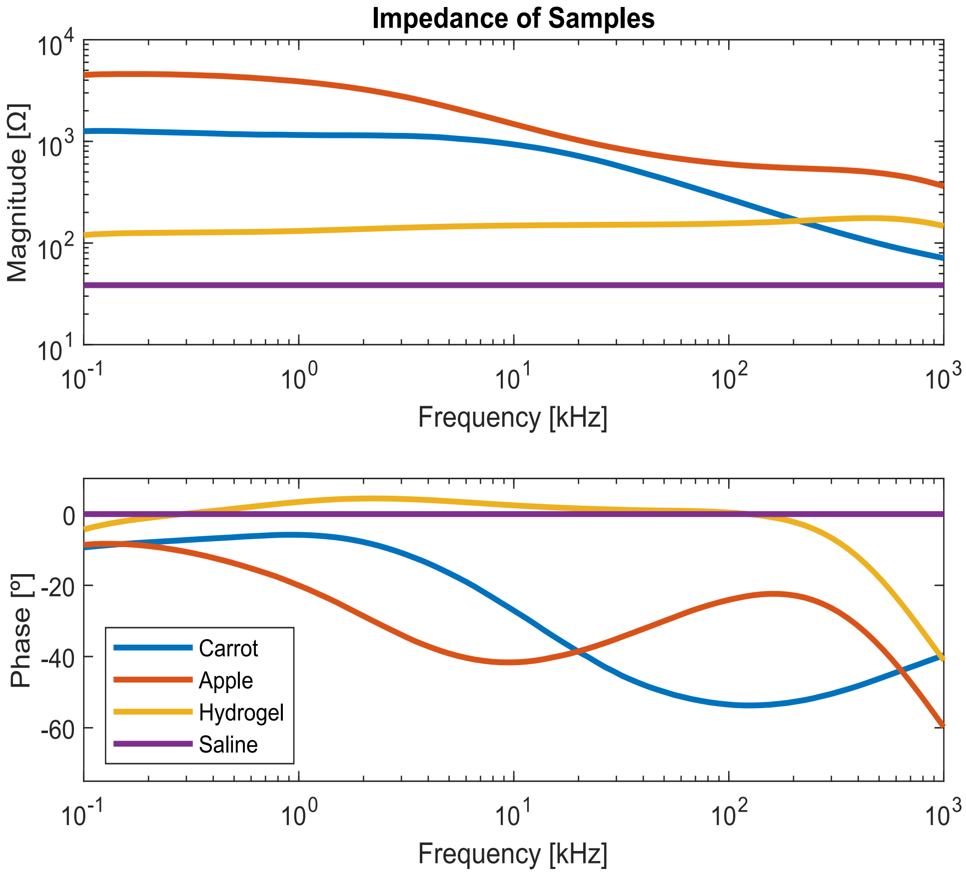

Source: Produced by the Author, 2021.

It can be seen that the impedances of both biological samples (carrot and apple) are several orders of magnitude larger than the saline solution. Therefore, TDEIT should have no problem to identify these materials and even distinguish between then. Moreover, the impedance of apple and carrot dropped from 1.4 $k\Omega$ to 588.8 Ω and from 945 $k\Omega$ to 276.6 Ω, respectively, between 10 and 100 kHz. Meanwhile, the saline impedance remained at 38.48 Ω at all frequencies. This means that FDEIT is also able to detect these samples, as the conductivity increases in frequency in contrast with the background. It is also interest to notice the behavior of the phase, showing the presence of dispersion domains that are typical to biological tissues (GRIMNES; MARTINSEN, 2011).

The hydrogel impedance, on the other hand, showed a behavior very similar to the saline: the impedance remained at approximately at 136.4 Ω for all frequencies. This means that the hydrogel part will be invisible to FDEIT measurements, but TDEIT may be able to detect variations. This is desirable in bioprinting applications, where the main goal is to detect the presence of biological material without interference of the hydrogel.

### 7.3.2 Calibration

In all imaging experiments, the mismatches between channels (subsection 7.2.2) were calibrated. The calibration process consisted of simply multiplying the data by a calibration factor:

$$data_{calibrated} = data_{raw} \times \frac{100\%}{(100\% + error_{\%})} \tag{7.1}$$

The $error_{\%}$ term corresponds to the error vector obtained in subsection 7.2.2. Moreover, FDEIT data was further calibrated to reduce the effects of circuit parasitic components. The calibration method implemented was proposed by Wu (WU et al., 2019), which performs FDEIT measurements in a homogeneous saline sample and uses the data vector as reference:

$$FD\_data_{calibrated} = FD\_data_{sample} - FD\_data_{reference} \tag{7.2}$$

The idea is that the reference saline sample is frequency invariant, so any variation detected is generated by the circuit itself. Considering that the impedance of the samples are not very different from the homogeneous reference, the variations remain constant in all samples. Therefore, by subtracting the reference vector (equation 7.2) the circuit error can be eliminated (WU et al., 2019).

### 7.3.3 Gain Selection

As discussed previously, the VGA gain plays an important role in image quality, by increasing the analog signal-to-noise ratio and improving the resolution of the discretized data. However, gain is limited by the dynamic range and slew-rate of the circuit, so too much gain can lead to distortion and saturation. Therefore, one sample was prepared to empirically select the optimal gain. The sample consisted of a piece of carrot placed inside the saline background (1.5 S/m). The excitation frequency was equal to 10 kHz. Figure 7.14 shows the different EIT images for several VGA gains.

It can be seen that the increase in gain increases the sharpness of the detected object and reduces the amount and magnitude of artifacts. Gains below 35 V/V resulted in images with several errors and distortions. Both 35 V/V and 157.7 V/V presented good performance, although several artifacts were also present. However, the 710.1 V/V showed strong image errors, due to signal saturation caused by the excessive gain. The 157.7 V/V gain was selected as the best one due to the reduced magnitude of artifacts and better sharpness of the object

Figure 7.14 – Measured sample and the correspondent EIT image for each VGA gain.

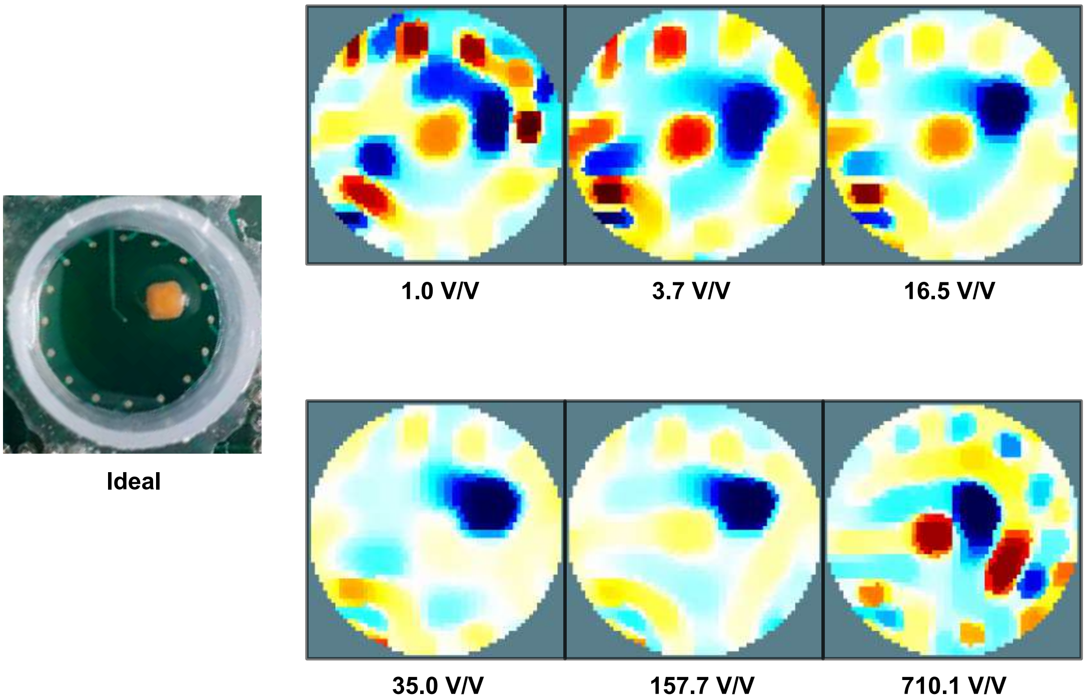

Source: Produced by the Author, 2021.

boundaries. It is important to notice that the optimal gain depends on the sample, so different experiments may require different gain values.

### 7.3.4 Inorganic Samples

To verify the ability to differentiate between conductive and insulating materials, a silicone rod and a metallic rod, both with approximately 3 mm of diameter, were measured. The EIT image of the silicone rod is showed in figure 7.15. The blue color means a negative change in conductivity. This result agrees with the insulating property of silicone, with an electrical conductivity almost negligible when compared to the saline. It can be seen that the position and the shape of the rod were correctly reconstructed in the EIT image. The 100 kHz image was sharper and presented less artifacts than the 10 kHz counterpart, which can be attributed to the number of periods collected: because the sampling window was fixed, the 100 kHz measurements had ten times more periods than the 10 kHz. This makes the FFT of the 100 kHz signal more accurate and less prone to leakage and noise.

The metallic sample, when compared to the silicone rod, presented stronger image noise, especially at 100 kHz. Moreover, both position and shape reconstruction were worst than the insulating sample. Nevertheless, the EIT system was able to detect a positive change in conductivity at the object region. The 10 kHz measurement presented a better outcome than the

Figure 7.15 – EIT images of the plastic rod at 10 kHz and 100 kHz.

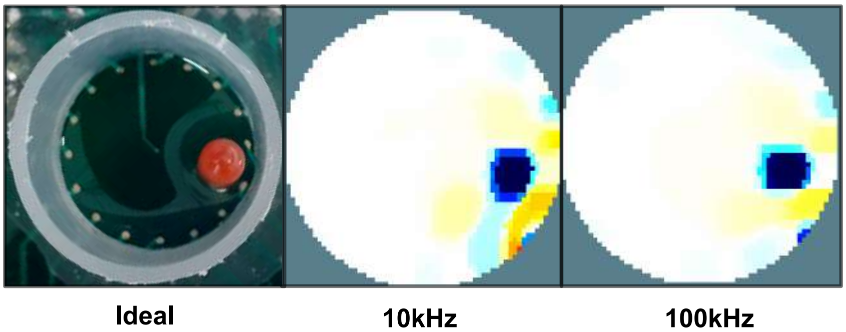

Source: Produced by the Author, 2021.

100 kHz TDEIT, maybe due to skin effect or the self-inductance of the stainless steel, which decreases the conductivity and, hence, the contrast between background and sample.

Figure 7.16 – EIT images of the metallic rod at 10 kHz and 100 kHz.

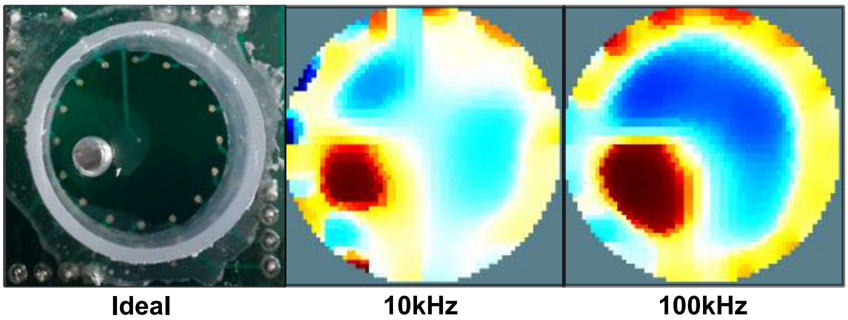

Source: Produced by the Author, 2021.

These results show that the EIT device can detect both positive and negative changes in conductivity, which is essential to monitor both cell growth, activity and metabolism. However, the conductivity change resulted from inorganic samples do not properly represent the variations encountered in biological samples, so the imaging of biological materials is fundamental for system validation.

### 7.3.5 Biological Materials

As discussed in the previous sections, the electrical conductivity of biological materials is largely defined by the $\alpha$, $\beta$ and $\gamma$ dispersion domains (GRIMNES; MARTINSEN, 2011), which are not found in metals and silicone. To obtain biological properties that better simulates a cultivated tissue, pieces of vegetables (carrot and apple) were used as phantoms. The first EIT feature analysed was position tracking, which verifies if the device can reconstruct the object at the correct positions. A piece of carrot (3 mm x 3mm) was positioned at different locations and the correspondent TDEIT image was obtained. Results are shown in figure 7.17.

Figure 7.17 – EIT images of a carrot phantom at several different positions, using 10 kHz and 100 kHz.

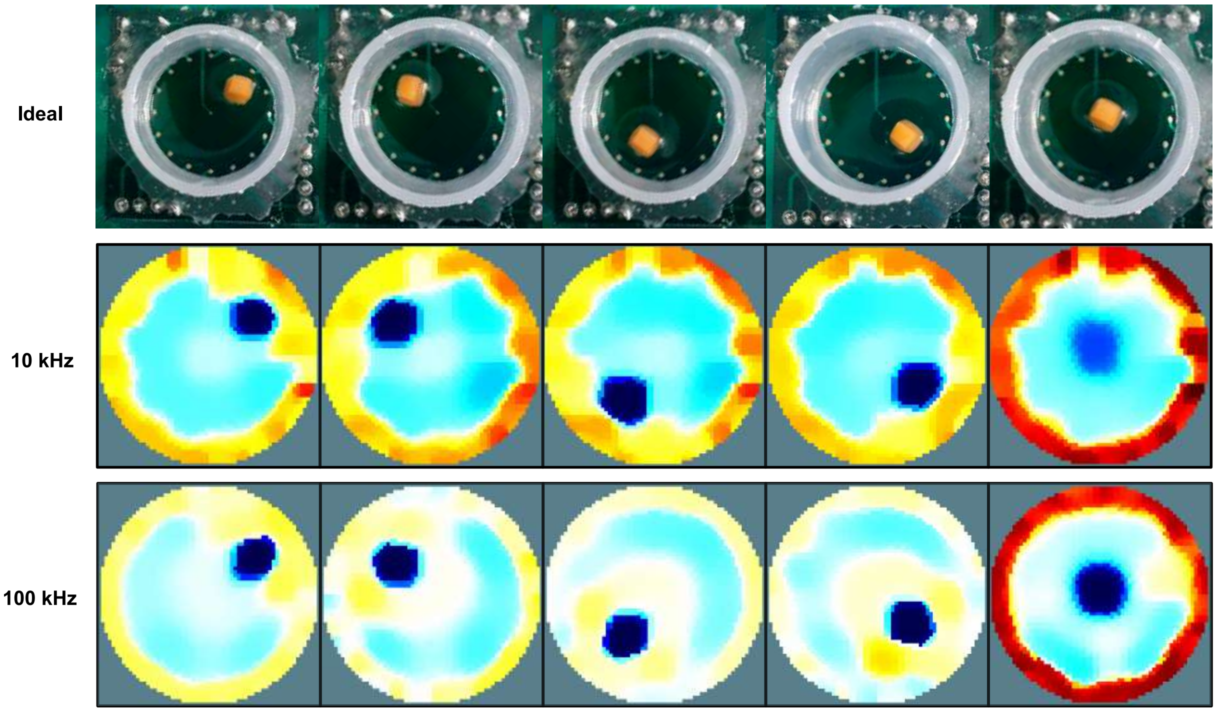

Source: Produced by the Author, 2021.

It can be seen that both frequencies were able to correct capture the phantom position in all configurations. Also, it can be correctly assumed from the EIT images that the conductivity of the object (carrot) is lower than the conductivity of the background (saline) in both frequencies, which agrees with the impedance data presented in Figure 7.13. The 100 kHz frequency provided less image artifacts and better shape fidelity when compared to the 10 kHz images. The artifacts in both frequencies can be attributed to two factors:

- The carrot displaces a volume of water when inserted into the well. Although this volume was removed from the well to keep the water height constant, this process was not perfect, and some mismatch between homogeneous and inhomogeneous water volume is expected to occur;
- The water formed a meniscus between the well and the phantom. This meniscus increases the liquid height at the vicinity of the phantom and the walls, resulting in a local increase of conductivity. This explains the orange/yellow artifacts near the image boundary and phantom.

Furthermore, the image quality of the last image, corresponding to the phantom located at the center of the sensor, was significantly lower than the others. This result was expected, as the sensitivity of the adjacent EIT protocol is lower at the center and higher at the boundaries of the sensing region (Figure 6.4).

After the position tracking experiments, the ability to proper reconstruct shapes was verified. Three geometries were selected: a small square (3 mm x 3 mm), a large square (5 mm x 5 mm) and an isosceles right triangle (5 mm of side). Results are shown in figure 7.18.

Figure 7.18 – EIT images of a carrot phantom with three different shapes, using 10 kHz and 100 kHz. Measured shapes were: small square (a), large square (b) and triangle (c)

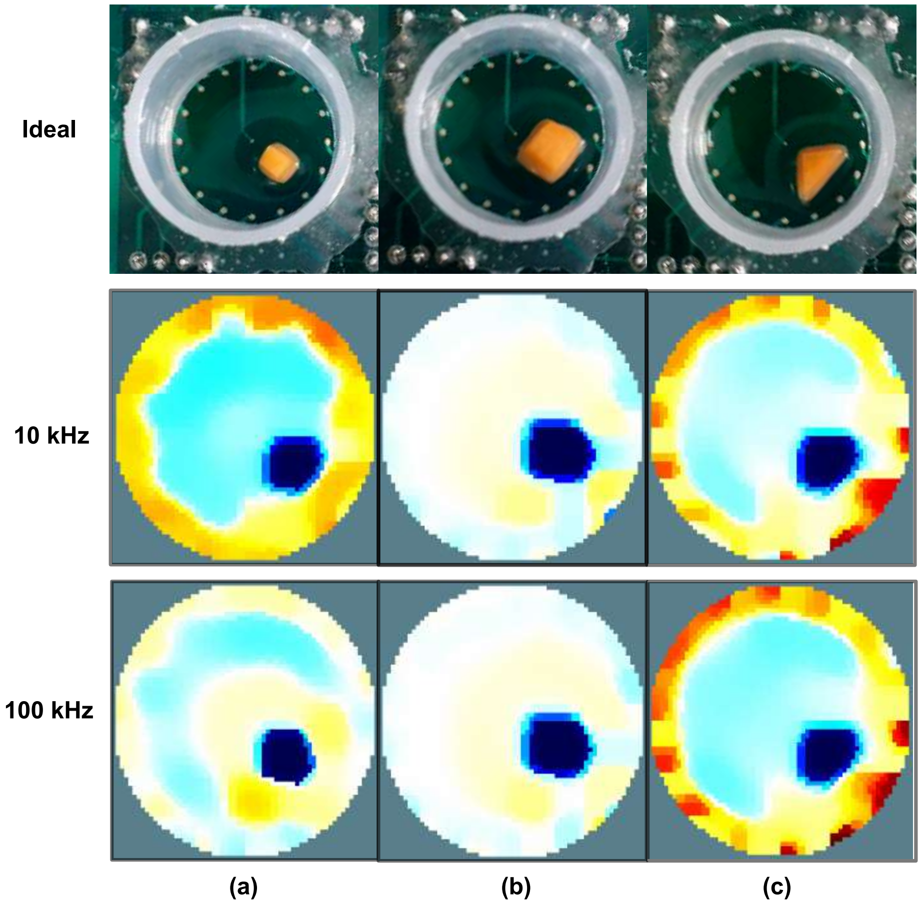

Source: Produced by the Author, 2021.

The EIT device was able to detect the increase in size of the square phantom. This feature is desirable in tissue engineering, when the growth of the constructed tissue must be monitored. Moreover, the direction of each tip of the triangle can be correctly identified in the EIT image. However, the edges of the geometries were not properly reconstructed. Although sharp edges are a typical limitation in conventional reconstruction algorithms (RANADE; GHARPURE, 2019), the shape distortion can also be attributed to the use of a 2D FEM model in a 3D electrical environment (see Section 6.1). The use of 3D FEM models and/or advanced image reconstruction algorithms can improve image sharpness. Despite the lack of edge features, the EIT device was able to capture the orientation of the object, as showed in Figure 7.19.

In the ideal image of Figure 7.19, the arrows are pointing to the direction of the hypotenuse, which is the largest length of the triangle. In biomedical applications, it is important to correctly identify the growing direction of the cultivated tissue, especially if this growth

Figure 7.19 – EIT images of a carrot phantom with three different orientations, using 10 kHz and 100 kHz.

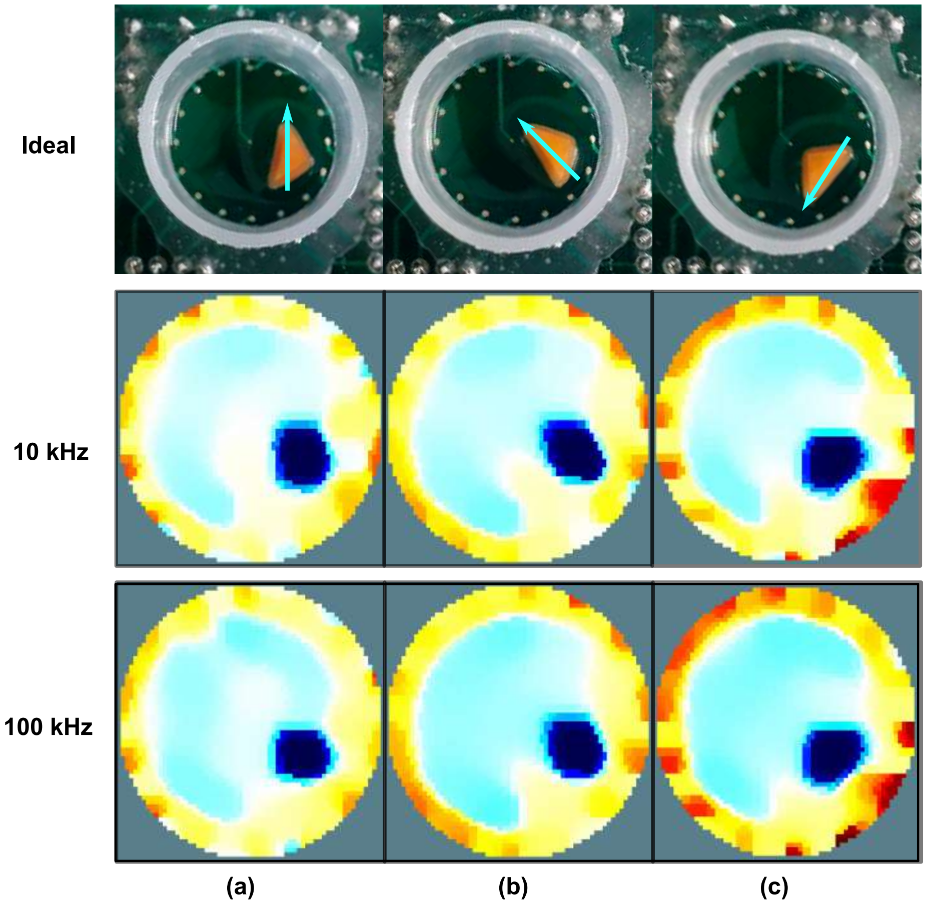

Source: Produced by the Author, 2021.

is being stimulated by a bioreactor. The 10 kHz frequency provided better results in terms of contrast and orientation fidelity. Besides growth direction, it is also important to identify multiple spots of tissue formation. To analyze the device's ability to correctly reconstruct multiple objects at the same time, two pieces of carrot with same dimensions were measured, using TDEIT at 10 kHz and 100 kHz. Results are shown in Figure 7.20.

The results confirmed the possibility of measuring two distinct objects at the same time, with little distortion. Moreover, the intensity of the blue color is the same in both objects, which is expected as both are constituted by the same material. However, tissue engineering often require co-cultures of different tissues within the same structure. One possible application is the manufacturing of cartilage-to-bone interfaces *in vitro* (NOOEAID et al., 2014). To test imaging of different materials, one of the carrot phantoms was replaced by a similar object made of apple. The results (Figure 7.21) show a slight difference in conductivity between the apple and the carrot object. However, the apple object shows a higher conductivity than the carrot one, which contradicts the results in Figure 7.13. One hypothesis is the higher porosity of the apple when compared to the carrot, which allows a higher level of water intake and

Figure 7.20 – EIT images of two identical carrot phantoms, using 10 kHz and 100 kHz.

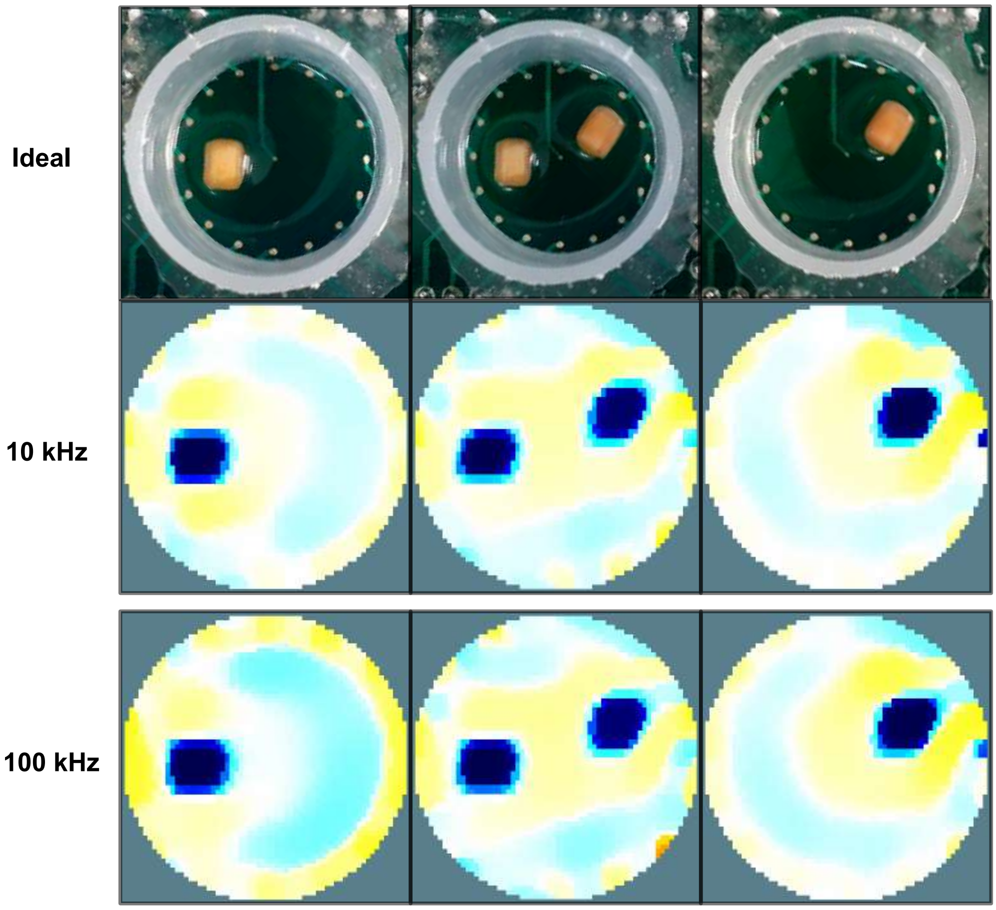

Source: Produced by the Author, 2021.

ion exchange with the background, resulting in an increase in conductivity. One evidence supporting this hypothesis is the presence of light-blue artifacts surrounding the apple object, indicating a reduction in saline conductivity caused by the ion exchange.

The FDEIT image also detected a difference in conductivity between samples. The red color indicates an increase in conductivity with frequency, which agrees with the impedance plots in Figure 7.13. Nonetheless, the impedance of the apple dropped 855.2 Ω, whereas the carrot dropped 660 Ω. This indicates that the apple object should be darker than the carrot (meaning a higher increase in conductivity), which was not the case (Figure 7.21). Although this result does not correctly reflects the impedance of the apple compared to the carrot, it supports the water/ion intake hypothesis discussed in the previous paragraph. Nevertheless, the possibility of measuring multiple objects with distinct conductivities was confirmed.

It is known that the use of flat cables in instrumentation circuits may result in interference, especially due to capacitive coupling and lack of shielding. To verify the robustness of the system, TDEIT images (10 kHz and 100 kHz) were obtained using a single carrot phantom with and without interference. Interference was produced using a metallic stripe (aluminum

Figure 7.21 – EIT images of a carrot phantom and a apple phantom, using TDEIT 10 kHz, TDEIT 100 kHz and FDEIT.

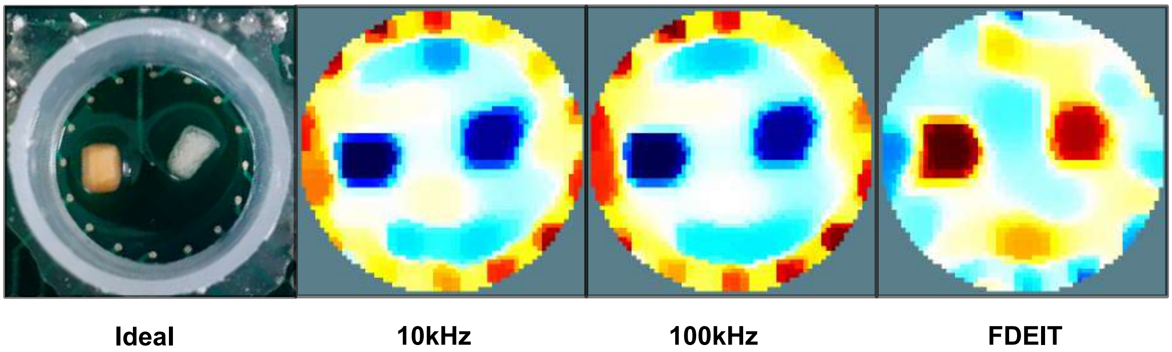

Source: Produced by the Author, 2021.

foil) excited with a white noise signal generated by the oscilloscope. The stripe was fixed near the cable. Furthermore, the cable was handled during the imaging process, to also account for possible capacitive coupling produced by the user's body. The results presented in Figure 7.22 show only a small increase in image artifacts (especially at 100 kHz), which confirms the robustness of the differential signaling implemented in the system.

Figure 7.22 – TDEIT images of a carrot phantom using 10 kHz and 100 kHz with and without interference.

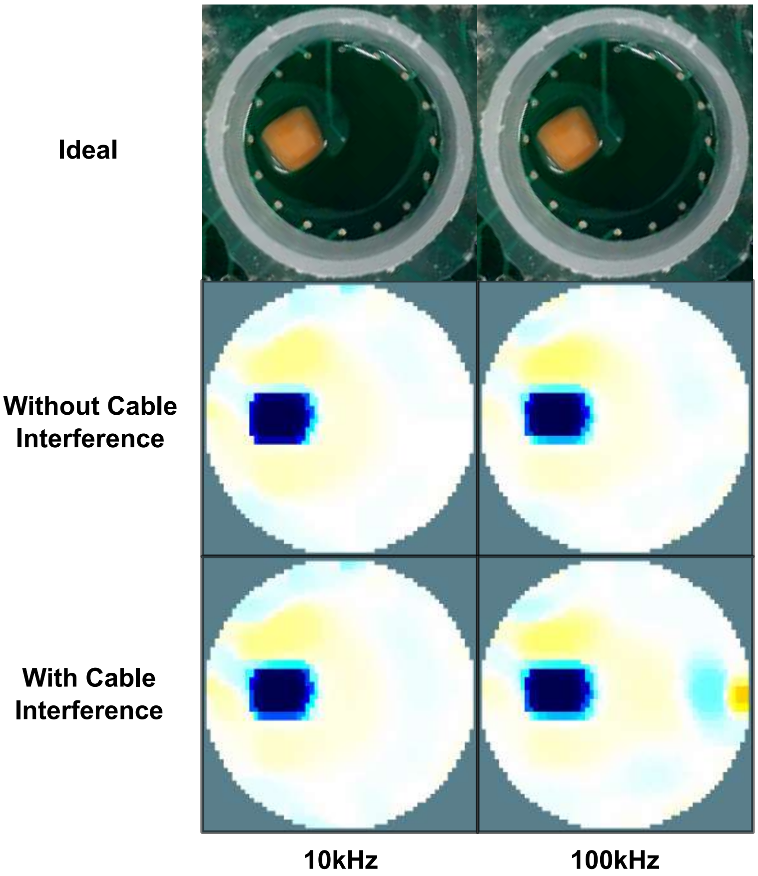

Source: Produced by the Author, 2021.

Finally, a small phantom cube (2 mm x 2 mm x 2 mm) was inserted inside a bioprinted phantom. The selected bioprinted structure was the hexagon presented in Figure 7.1. The ability to measure a biological structure inside a bioprinted scaffold is fundamental to apply EIT in bioprinted tissue monitoring. The ideal image in Figure 7.1 shows the measured structure with the carrot piece. This phantom was used to electrically simulate a cell agglomeration inside a scaffold. It can be seen that both TDEIT images failed to properly reconstruct the phantom piece. The conductivity increase presented in the TDEIT images is not expected to be caused by the phantom itself, as the presence of the carrot should drop the impedance. However, the insertion of the phantom caused a lump in the hydrogel, increasing the local volume and resulting in an increase in the apparent conductivity. The phantom was successfully detected using FDEIT. As discussed in Section 5.5 and confirmed in Figure 7.13, the use of FDEIT can help distinguish between biological and non-biological materials, so FDEIT should in fact provide better results than TDEIT in the presence of both bioprinted scaffold and cells. This result confirms the necessity of using FDEIT in cell tracking and further validates the use of EIT as a remote, non-invasive and real-time monitoring technique for bioprinted tissue.

Figure 7.23 – EIT images of a bioprinted construct containing a carrot phantom simulating localized formation of tissue using 10 kHz TDEIT, 100 kHz TDEIT and FDEIT.

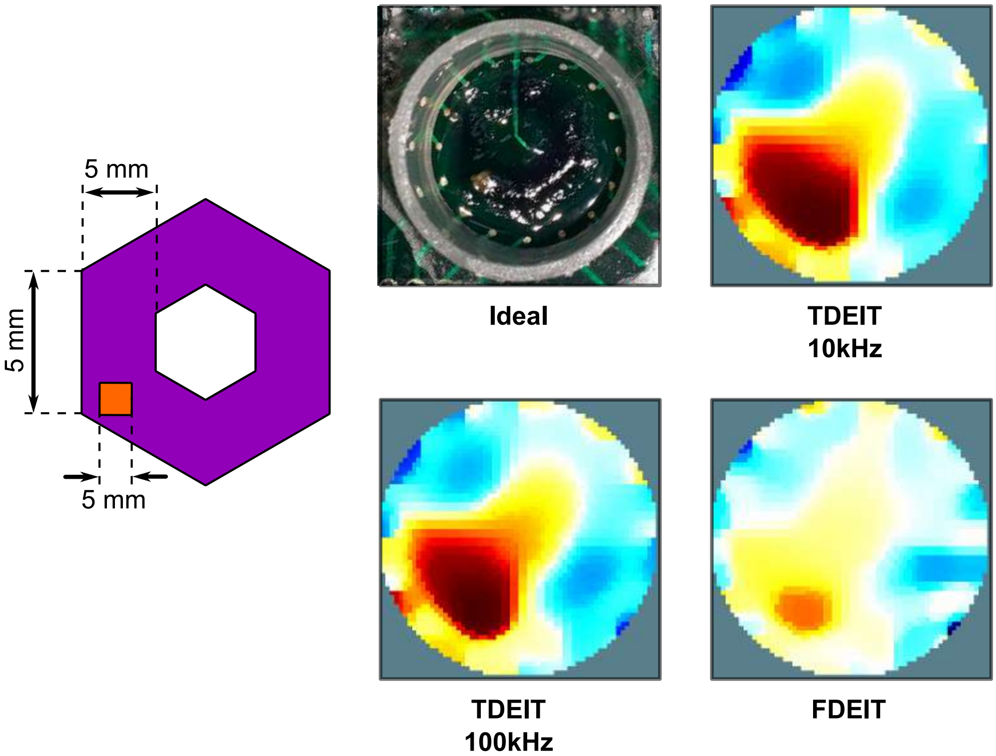

Source: Produced by the Author, 2021.

# 8 CONCLUSION

This thesis presented the development of an EIT measuring system for bioprinted constructs. The reduced sensor size (2 centimeters of diameter) and portability of the device allow its easy implementation in tissue engineering, either for fast experiments or for long term monitoring of the culture. The system can improve significantly the 4D bioprinting process, as each state of the three-dimensional culture can be tracked in real-time and non-invasively.

To design the circuit, an integrated simulation framework was developed. It combines the EIT simulation of EIDORS with the circuit simulation of PSPICE in an automatic process. The 2D Iterative Total Variation Regularization algorithm was able to capture both the position and conductivity of simulated cell spheroids, using 10 kHz TDEIT. However, the 2D reconstruction model caused significant distortion in the shape. Circuit characterization via PSPICE showed that the differential Howland source performance presented good agreement with theoretical equations, with a 150 $\mu S$ transconductance, maximum output impedance of 5.05 MΩ at 10 kHz and minimum common-mode voltage. At the voltage sensing side, the frequency response was completely defined by the antialiasing filter and remained independent of the VGA gain. Using the integrated simulation framework, it was possible to see that the introduction of circuit non-idealities caused significant position errors in the simulated images.

Three hydrogel structures were printed to validate the dedicated 3D bioprinter: an hexagon, a bone-shaped object and a porous mesh. All three objects maintained mechanical stability after crosslinking. The geometry fidelity was high in the horizontal plane, however the Z-axis fidelity was poor, with inhomogeneous distribution of height. This was attributed to the low performance of the bioink, and proper tuning of the rheological properties of the hydrogel can improve the results significantly. Nevertheless, the bioprinter served its purpose to deliver a usable phantom for the validation of the EIT system.

The excitation circuit was able to provide a symmetrical current of approximately 250 $\mu A$ of amplitude, using square waves at 10 kHz and 100 kHz. The differential topology provided a reduced amount of common-mode voltage at load while still keeping the current at the desired levels. The maximum output current error was equal to 4% for loads up to 3.3 kΩ, which is more than enough to operate with the designed electrodes (with total impedance of 409.4 Ω). However, the frequency response of the excitation circuit was significantly limited: the current error at 100 kHz was equal to 6.5% using the 470 Ω load and 32% using the 3.3 kΩ load. Nonetheless, all TDEIT and FDEIT images were obtained using a homogeneous phantom as reference, which eliminated the errors introduced by the circuit. The maximum current error between channels was less than 1% at 10 kHz and 2% at 100 kHz.

The voltage sensing stage improved significantly the flexibility of the design, as the gain could be controlled from 1 to 10000 V/V with minimum impact in the frequency response. Moreover, the fully-differential signaling approach improved significantly the interference immunity of the system, and the maximum input-referred noise PSD was equal to 173.7 $nV/\sqrt{Hz}$. The maximum inter-channel error was equal to 2.5% at 10 kHz and 70% at 100 kHz. To minimize the impact of this error, a calibration vector was implemented.

The maximum frame rate of the designed hardware was equal to 7.37 fps using 10 kHz and 23.8 fps using 100 kHz, which is enough for real-time monitoring in most cell culture experiments. However, the serial communication with the MATLAB interface introduced a delay of 0.02 s per measurement. Because of this, all EIT images were obtained offline. This can be solved by simply migrating to another development framework or language, such as Python.

Finally, EIT images were obtained using inorganic and biological phantoms. The optimum gain for EIT images was equal to 157.7 V/V (44 dB). TDEIT images of a silicone rod and a metallic rod showed that the system was capable of differentiating between insulating and conductive materials. To verify the performance of the system when imaging biological materials, vegetable-based (carrot and apple) phantoms were used. The EIT system was able to identify the correct position, size and orientation of the biological object using TDEIT. Furthermore, when multiple objects were present, the system provided the correct boundaries for each phantom and was able to differentiate between different materials using both TDEIT and FDEIT. However, the shape identification of the system is limited, due to the use of 2D image reconstruction instead of 3D. The system was also capable of identifying the position and size of a small carrot piece inside a bioprinted hydrogel scaffold, using FDEIT. These results validate the applicability of the system in tissue engineering experiments. However, all limitations here discussed should be resolved first.

## 8.1 FUTURE WORK

Firstly, the communication interface between the system and the host computer will be improved, to obtain true real-time operation. Both interface and image reconstruction algorithm will be developed in Python and/or C++. Secondly, a 3D reconstruction algorithm will be implemented, to reduce the shape distortion and other image errors. Finally, a battery power-supply and a WiFi communication module will be added, providing wireless operation to improve the device's flexibility. After all these upgrades, the device will be applied in actual bioprinting applications to validate its performance.

# BIBLIOGRAPHY

ABSHER, M. Hemocytometer counting. In: **Tissue culture**. [S.l.]: Elsevier, 1973. p. 395–397.

ADLER, A.; BOYLE, A. Electrical impedance tomography: Tissue properties to image measures. **IEEE Transactions on Biomedical Engineering**, 2017. v. 64, 2017. ISSN 15582531.

ADLER, A.; GUARDO, R. Electrical impedance tomography: regularized imaging and contrast detection. **IEEE transactions on medical imaging**, 1996. IEEE, v. 15, n. 2, p. 170–179, 1996.

ALEX, A.; REDDY, M. R. Application of meshless local petrov galerkin method (mlpg5) for eit forward problem. **Biomedical Physics & Engineering Express**, 2018. IOP Publishing, v. 4, n. 4, p. 045036, 2018.

ALEXANDER, F. A.; PRICE, D. T.; BHANSALI, S. From cellular cultures to cellular spheroids: is impedance spectroscopy a viable tool for monitoring multicellular spheroid (mcs) drug models? **IEEE reviews in biomedical engineering**, 2012. IEEE, v. 6, p. 63–76, 2012.

ANGSTMANN, M.; BRINKMANN, I.; BIEBACK, K.; BREITKREUTZ, D.; MAERCKER, C. Monitoring human mesenchymal stromal cell differentiation by electrochemical impedance sensing. **Cytotherapy**, 2011. Taylor & Francis, v. 13, n. 9, p. 1074–1089, 2011.

ARISTOVICH, K. Y.; PACKHAM, B. C.; KOO, H.; SANTOS, G. S. dos; MCEVOY, A.; HOLDER, D. S. Imaging fast electrical activity in the brain with electrical impedance tomography. **NeuroImage**, 2016. Elsevier, v. 124, p. 204–213, 2016.

ASAMI, K. Characterization of heterogeneous systems by dielectric spectroscopy. **Progress in polymer science**, 2002. Elsevier, v. 27, n. 8, p. 1617–1659, 2002.

BAYFORD, R.; GIBSON, A.; TIZZARD, A.; TIDSWELL, T.; HOLDER, D. S. Solving the forward problem in electrical impedance tomography for the human head using ideas (integrated design engineering analysis software), a finite element modelling tool. **Physiological measurement**, 2001. IOP Publishing, v. 22, n. 1, p. 55, 2001.

BAYFORD, R. H. Bioimpedance tomography (electrical impedance tomography). **Annu. Rev. Biomed. Eng.**, 2006. Annual Reviews, v. 8, p. 63–91, 2006.

BELLEGHEM, S. V.; JR, L. T.; SANTORO, M.; MAHADIK, B.; WOLFAND, A.; KOFINAS, P.; FISHER, J. P. Hybrid 3d printing of synthetic and cell-laden bioinks for shape retaining soft tissue grafts. **Advanced functional materials**, 2020. Wiley Online Library, v. 30, n. 3, p. 1907145, 2020.

BERA, T. K. Applications of electrical impedance tomography (eit): a short review. In: IOP PUBLISHING. **IOP Conference Series: Materials Science and Engineering**. [S.l.], 2018. v. 331, n. 1, p. 012004.

BERTEMES-FILHO, P. **Tissue Characterisation using an Impedance Spectroscopy Probe**. 27–35 p. Tese (Doutorado) — Sheffield, 2002.

BORSIC, A.; GRAHAM, B. M.; ADLER, A.; LIONHEART, W. R. Total variation regularization in electrical impedance tomography. 2007. Manchester Institute for Mathematical Sciences, University of Manchester, 2007.

BUCHWALOW, I. B.; BÖCKER, W. Immunohistochemistry. **Basics and Methods**, 2010. Springer, v. 1, p. 1–149, 2010.

CANALI, C.; ARISTOVICH, K.; CECCARELLI, L.; LARSEN, L. B.; MARTINSEN, Ø.; WOLFF, A.; DUFVA, M.; EMNÉUS, J.; HEISKANEN, A. Electrical impedance tomography methods for miniaturised 3d systems. **Journal of Electrical Bioimpedance**, 2016. Sciendo, v. 7, n. 1, p. 59–67, 2016.

CANALI, C.; HEISKANEN, A.; MUHAMMAD, H. B.; HØYUM, P.; PETTERSEN, F.-J.; HEMMINGSEN, M.; WOLFF, A.; DUFVA, M.; MARTINSEN, Ø. G.; EMNÉUS, J. Bioimpedance monitoring of 3d cell culturing—complementary electrode configurations for enhanced spatial sensitivity. **Biosensors and Bioelectronics**, 2015. Elsevier, v. 63, p. 72–79, 2015.

CHEONG, W.-F.; PRAHL, S. A.; WELCH, A. J. A review of the optical properties of biological tissues. **IEEE journal of quantum electronics**, 1990. IEEE, v. 26, n. 12, p. 2166–2185, 1990.

CHOUDHURY, D.; ANAND, S.; NAING, M. W. The arrival of commercial bioprinters–towards 3d bioprinting revolution. **Int J Bioprint**, 2018. v. 4, n. 2, p. 139, 2018.

CORBETT, D. C.; OLSZEWSKI, E.; STEVENS, K. A fresh take on resolution in 3d bioprinting. **Trends in biotechnology**, 2019. Elsevier, v. 37, n. 11, p. 1153–1155, 2019.

CURTO, V. F.; MARCHIORI, B.; HAMA, A.; PAPPA, A.-M.; FERRO, M. P.; BRAENDLEIN, M.; RIVNAY, J.; FIOCCHI, M.; MALLIARAS, G. G.; RAMUZ, M. et al. Organic transistor platform with integrated microfluidics for in-line multi-parametric in vitro cell monitoring. **Microsystems & nanoengineering**, 2017. Nature Publishing Group, v. 3, n. 1, p. 1–12, 2017.

DABABNEH, A. B.; OZBOLAT, I. T. Bioprinting technology: a current state-of-the-art review. **Journal of Manufacturing Science and Engineering**, 2014. American Society of Mechanical Engineers Digital Collection, v. 136, n. 6, 2014.

DANESHMAND, P. G.; JAFARI, R. A 3d hybrid be–fe solution to the forward problem of electrical impedance tomography. **Engineering Analysis with Boundary Elements**, 2013. Elsevier, v. 37, n. 4, p. 757–764, 2013.

DANG, C.; BELLIS, C.; DARNAJOU, M.; RICCIARDI, G.; MYLVAGANAM, S.; BOURENNANE, S. Practical comparisons of eit excitation protocols with applications in high-contrast imaging. **Measurement Science and Technology**, 2021. IOP Publishing, v. 32, n. 8, p. 085110, 2021.

DARLING, E. M.; ATHANASIOU, K. A. Articular cartilage bioreactors and bioprocesses. **Tissue engineering**, 2003. Mary Ann Liebert, Inc., v. 9, n. 1, p. 9–26, 2003.

DEMIRCI, U.; MONTESANO, G. Single cell epitaxy by acoustic picolitre droplets. **Lab on a Chip**, 2007. Royal Society of Chemistry, v. 7, n. 9, p. 1139–1145, 2007.

DONNALOJA, F.; JACCHETTI, E.; SONCINI, M.; RAIMONDI, M. T. Natural and synthetic polymers for bone scaffolds optimization. **Polymers**, 2020. Multidisciplinary Digital Publishing Institute, v. 12, n. 4, p. 905, 2020.

DU, X. 3d bio-printing review. In: IOP PUBLISHING. **IOP Conference Series: Materials Science and Engineering**. [S.l.], 2018. v. 301, n. 1, p. 012023.

EDMANS, A.; INTES, X. Mesh optimization for monte carlo-based optical tomography. In: MULTIDISCIPLINARY DIGITAL PUBLISHING INSTITUTE. **Photonics**. [S.l.], 2015. v. 2, n. 2, p. 375–391.

FRESHNEY, R. I. **Culture of Animal Cells**. [S.l.: s.n.], 2005. ISSN 0025-7753.

GAO, B.; YANG, Q.; ZHAO, X.; JIN, G.; MA, Y.; XU, F. 4d bioprinting for biomedical applications. **Trends in biotechnology**, 2016. Elsevier, v. 34, n. 9, p. 746–756, 2016.

GAO, G.; HUANG, Y.; SCHILLING, A. F.; HUBBELL, K.; CUI, X. Organ bioprinting: are we there yet? **Advanced healthcare materials**, 2018. Wiley Online Library, v. 7, n. 1, p. 1701018, 2018.

GAUVIN, R.; CHEN, Y.-C.; LEE, J. W.; SOMAN, P.; ZORLUTUNA, P.; NICHOL, J. W.; BAE, H.; CHEN, S.; KHADEMHOSSEINI, A. Microfabrication of complex porous tissue engineering scaffolds using 3d projection stereolithography. **Biomaterials**, 2012. Elsevier, v. 33, n. 15, p. 3824–3834, 2012.

GIAEVER, I.; KEESE, C. R. Use of electric fields to monitor the dynamical aspect of cell behavior in tissue culture. **IEEE Transactions on Biomedical Engineering**, 1986. IEEE, n. 2, p. 242–247, 1986.

GILLISPIE, G. J.; PARK, J.; COPUS, J. S.; KUMAR, A.; RAJAN, P.; YOO, J. J.; ATALA, A.; LEE, S. J. **Three-Dimensional Tissue and Organ Printing in Regenerative Medicine**. Elsevier Inc., 2019. 831–852 p. ISBN 9780128098806. Disponível em: <http://dx.doi.org/10.1016/B978-0-12-809880-6.00047-3>.

GOLDSTEIN, T. A.; EPSTEIN, C. J.; SCHWARTZ, J.; KRUSH, A.; LAGALANTE, D. J.; MERCADANTE, K. P.; ZELTSMAN, D.; SMITH, L. P.; GRANDE, D. A. Feasibility of bioprinting with a modified desktop 3d printer. **Tissue Engineering Part C: Methods**, 2016. Mary Ann Liebert, Inc. 140 Huguenot Street, 3rd Floor New Rochelle, NY 10801 USA, v. 22, n. 12, p. 1071–1076, 2016.

GOPINATHAN, J.; NOH, I. Recent trends in bioinks for 3d printing. **Biomaterials research**, 2018. Springer, v. 22, n. 1, p. 11, 2018.

GRIFFITHS, H.; TUCKER, M.; SAGE, J.; HERRENDEN-HARKER, W. An electrical impedance tomography microscope. **Physiological measurement**, 1996. IOP Publishing, v. 17, n. 4A, p. A15, 1996.

GRIMNES, S.; MARTINSEN, O. G. **Bioimpedance and bioelectricity basics**. [S.l.]: Academic press, 2011.

GUDAPATI, H.; DEY, M.; OZBOLAT, I. A comprehensive review on droplet-based bioprinting: past, present and future. **Biomaterials**, 2016. Elsevier, v. 102, p. 20–42, 2016.

GUILLOTIN, B.; SOUQUET, A.; CATROS, S.; DUOCASTELLA, M.; PIPPENGER, B.; BELLANCE, S.; BAREILLE, R.; RÉMY, M.; BORDENAVE, L.; AMÉDÉE, J. et al. Laser assisted bioprinting of engineered tissue with high cell density and microscale organization. **Biomaterials**, 2010. Elsevier, v. 31, n. 28, p. 7250–7256, 2010.

GUO, Y.; GILBERT-HONICK, J.; SOMERS, S. M.; MAO, H.-Q.; GRAYSON, W. L. Modified cell-electrospinning for 3d myogenesis of c2c12s in aligned fibrin microfiber bundles. **Biochemical and Biophysical Research Communications**, 2019. Elsevier, 2019.

HABIB, A.; SATHISH, V.; MALLIK, S.; KHODA, B. 3d printability of alginate-carboxymethyl cellulose hydrogel. **Materials**, 2018. Multidisciplinary Digital Publishing Institute, v. 11, n. 3, p. 454, 2018.

HALLAJI, M.; SEPPÄNEN, A.; POUR-GHAZ, M. Electrical impedance tomography-based sensing skin for quantitative imaging of damage in concrete. **Smart Materials and Structures**, 2014. IOP Publishing, v. 23, n. 8, p. 085001, 2014.

HAUGLAND, R. P.; MACCOUBREY, I. C.; MOORE, P. L. **Dual-fluorescence cell viability assay using ethidium homodimer and calcein AM**. [S.l.]: Google Patents, 1994. US Patent 5,314,805.

HAYCOCK, J. W. 3d cell culture: a review of current approaches and techniques. In: **3D cell culture**. [S.l.]: Springer, 2011. p. 1–15.

HELGASON, C. D.; MILLER, C. L. **Basic cell culture protocols**. [S.l.]: Springer, 2005.

HINTON, T. J.; JALLERAT, Q.; PALCHESKO, R. N.; PARK, J. H.; GRODZICKI, M. S.; SHUE, H.-J.; RAMADAN, M. H.; HUDSON, A. R.; FEINBERG, A. W. Three-dimensional printing of complex biological structures by freeform reversible embedding of suspended hydrogels. **Science advances**, 2015. American Association for the Advancement of Science, v. 1, n. 9, p. e1500758, 2015.

HOLDER, D. S. **Electrical impedance tomography: methods, history and applications**. [S.l.]: CRC Press, 2004.

HONG, N.; YANG, G.-H.; LEE, J.; KIM, G. 3d bioprinting and its in vivo applications. **Journal of Biomedical Materials Research Part B: Applied Biomaterials**, 2018. Wiley Online Library, v. 106, n. 1, p. 444–459, 2018.

HOSPODIUK, M.; DEY, M.; SOSNOSKI, D.; OZBOLAT, I. T. The bioink: A comprehensive review on bioprintable materials. **Biotechnology advances**, 2017. Elsevier, v. 35, n. 2, p. 217–239, 2017.

HUANG, Q.; ZENG, Z. A review on real-time 3d ultrasound imaging technology. **BioMed research international**, 2017. Hindawi, v. 2017, 2017.

IQBAL, N.; KHAN, A. S.; ASIF, A.; YAR, M.; HAYCOCK, J. W.; REHMAN, I. U. Recent concepts in biodegradable polymers for tissue engineering paradigms: A critical review. **International Materials Reviews**, 2019. Taylor & Francis, v. 64, n. 2, p. 91–126, 2019.

JAKAB, K.; NOROTTE, C.; MARGA, F.; MURPHY, K.; VUNJAK-NOVAKOVIC, G.; FORGACS, G. Tissue engineering by self-assembly and bio-printing of living cells. **Biofabrication**, 2010. IOP Publishing, v. 2, n. 2, p. 022001, 2010.

JIMBO, Y.; KAWANA, A. Electrical stimulation and recording from cultured neurons using a planar electrode array. **Bioelectrochemistry and Bioenergetics**, 1992. Elsevier, v. 29, n. 2, p. 193–204, 1992.

JIN, B.; KHAN, T.; MAASS, P. A reconstruction algorithm for electrical impedance tomography based on sparsity regularization. **International Journal for Numerical Methods in Engineering**, 2012. Wiley Online Library, v. 89, n. 3, p. 337–353, 2012.

KALLOS, M. S.; SEN, A.; BEHIE, L. A. Large-scale expansion of mammalian neural stem cells: A review. **Medical and Biological Engineering and Computing**, 2003. v. 41, n. 3, p. 271–282, 2003. ISSN 01400118.

KERIQUEL, V.; OLIVEIRA, H.; RÉMY, M.; ZIANE, S.; DELMOND, S.; ROUSSEAU, B.; REY, S.; CATROS, S.; AMÉDÉE, J.; GUILLEMOT, F. et al. In situ printing of mesenchymal stromal cells, by laser-assisted bioprinting, for in vivo bone regeneration applications. **Scientific reports**, 2017. Nature Publishing Group, v. 7, n. 1, p. 1778, 2017.

KOCH, L.; KUHN, S.; SORG, H.; GRUENE, M.; SCHLIE, S.; GAEBEL, R.; POLCHOW, B.; REIMERS, K.; STOELTING, S.; MA, N. et al. Laser printing of skin cells and human stem cells. **Tissue Engineering Part C: Methods**, 2010. Mary Ann Liebert, Inc. 140 Huguenot Street, 3rd Floor New Rochelle, NY 10801 USA, v. 16, n. 5, p. 847–854, 2010.

KOLESKY, D. B.; HOMAN, K. A.; SKYLAR-SCOTT, M. A.; LEWIS, J. A. Three-dimensional bioprinting of thick vascularized tissues. **Proceedings of the national academy of sciences**, 2016. National Acad Sciences, v. 113, n. 12, p. 3179–3184, 2016.

KOLESKY, D. B.; TRUBY, R. L.; GLADMAN, A. S.; BUSBEE, T. A.; HOMAN, K. A.; LEWIS, J. A. 3d bioprinting of vascularized, heterogeneous cell-laden tissue constructs. **Advanced materials**, 2014. Wiley Online Library, v. 26, n. 19, p. 3124–3130, 2014.

LEI, M.; WANG, X. Biodegradable polymers and stem cells for bioprinting. **Molecules**, 2016. Multidisciplinary Digital Publishing Institute, v. 21, n. 5, p. 539, 2016.

LEÓN, S. E. D.; PUPOVAC, A.; MCARTHUR, S. L. Three-dimensional (3d) cell culture monitoring: Opportunities and challenges for impedance spectroscopy. **Biotechnology and Bioengineering**, 2020. Wiley Online Library, v. 117, n. 4, p. 1230–1240, 2020.

LI, Z.; HUANG, S.; LIU, Y.; YAO, B.; HU, T.; SHI, H.; XIE, J.; FU, X. Tuning alginate-gelatin bioink properties by varying solvent and their impact on stem cell behavior. **Scientific reports**, 2018. Nature Publishing Group, v. 8, n. 1, p. 1–8, 2018.

LINDERHOLM, P.; MARESCOT, L.; LOKE, M. H.; RENAUD, P. Cell culture imaging using microimpedance tomography. **IEEE Transactions on Biomedical Engineering**, 2007. IEEE, v. 55, n. 1, p. 138–146, 2007.

LIONHEART, W. R. Eit reconstruction algorithms: pitfalls, challenges and recent developments. **Physiological measurement**, 2004. IOP Publishing, v. 25, n. 1, p. 125, 2004.

LIU, F.; WANG, X. Synthetic polymers for organ 3d printing. **Polymers**, 2020. Multidisciplinary Digital Publishing Institute, v. 12, n. 8, p. 1765, 2020.

LONGNECKER, D. S.; GORELICK, F.; THOMPSON, E. D. Anatomy, histology, and fine structure of the pancreas. **The Pancreas. Chichester, UK: John Wiley & Sons, Ltd**, 2018. p. 10–23, 2018.

LORENZO, A. D.; ANDREOLI, A.; MATTHIE, J.; WITHERS, P. Predicting body cell mass with bioimpedance by using theoretical methods: a technological review. **Journal of applied physiology**, 1997. American Physiological Society Bethesda, MD, v. 82, n. 5, p. 1542–1558, 1997.

LU, Y.; MAPILI, G.; SUHALI, G.; CHEN, S.; ROY, K. A digital micro-mirror device-based system for the microfabrication of complex, spatially patterned tissue engineering scaffolds. **Journal of Biomedical Materials Research Part A: An Official Journal of The Society for Biomaterials, The Japanese Society for Biomaterials, and The Australian Society for Biomaterials and the Korean Society for Biomaterials**, 2006. Wiley Online Library, v. 77, n. 2, p. 396–405, 2006.

MARTINS, T. de C.; SATO, A. K.; MOURA, F. S. de; CAMARGO, E. D. L. B. de; SILVA, O. L.; SANTOS, T. B. R.; ZHAO, Z.; MÖELLER, K.; AMATO, M. B. P.; MUELLER, J. L. et al. A review of electrical impedance tomography in lung applications: Theory and algorithms for absolute images. **Annual Reviews in Control**, 2019. Elsevier, v. 48, p. 442–471, 2019.

MARTINSEN, O. G.; GRIMNES, S. **Bioimpedance and bioelectricity basics**. [S.l.]: Academic press, 2011.

MATAI, I.; KAUR, G.; SEYEDSALEHI, A.; MCCLINTON, A.; LAURENCIN, C. T. Progress in 3d bioprinting technology for tissue/organ regenerative engineering. **Biomaterials**, 2020. Elsevier, v. 226, p. 119536, 2020.

MATTIMORE, J. P.; GROFF, R. E.; BURG, T.; PEPPER, M. E. A general purpose driver board for the hp26 ink-jet cartridge with applications to bioprinting. In: IEEE. **Proceedings of the IEEE SoutheastCon 2010 (SoutheastCon)**. [S.l.], 2010. p. 510–513.

MILLER, W. S. The structure of the lung. **Journal of Morphology**, 1893. Wiley Subscription Services, Inc., A Wiley Company Hoboken, v. 8, n. 1, p. 165–188, 1893.

MIRONOV, V.; KASYANOV, V.; MARKWALD, R. R. Organ printing: from bioprinter to organ biofabrication line. **Current opinion in biotechnology**, 2011. Elsevier, v. 22, n. 5, p. 667–673, 2011.

MITCHELL, H.; HAMILTON, T.; STEGGERDA, F.; BEAN, H. The chemical composition of the adult human body and its bearing on the biochemistry of growth. **Journal of Biological Chemistry**, 1945. Elsevier, v. 158, n. 3, p. 625–637, 1945.

MOBARAKI, M.; GHAFFARI, M.; YAZDANPANAH, A.; LUO, Y.; MILLS, D. Bioinks and bioprinting: A focused review. **Bioprinting**, 2020. Elsevier, v. 18, p. e00080, 2020.

MOFFAT, D. B. **The mammalian kidney**. [S.l.]: CUP Archive, 1975.

MORCELLES, K.; BERTEMES-FILHO, P. Hardware for cell culture electrical impedance tomography: A critical review. **Review of Scientific Instruments**, 2021. AIP Publishing LLC, v. 92, n. 10, p. 104704, 2021.

MORCELLES, K.; SIRTOLI, V.; BERTEMES-FILHO, P.; VINCENCE, V. Howland current source for high impedance load applications. **Review of Scientific Instruments**, 2017. AIP Publishing LLC, v. 88, n. 11, p. 114705, 2017.

MOROUÇO, P. Biofabrication in Tissue Engineering. 2017. n. December, 2017.

MUELLER, J. L.; SILTANEN, S.; ISAACSON, D. A direct reconstruction algorithm for electrical impedance tomography. **IEEE Transactions on medical imaging**, 2002. IEEE, v. 21, n. 6, p. 555–559, 2002.

MURPHY, S. V.; ATALA, A. 3d bioprinting of tissues and organs. **Nature biotechnology**, 2014. Nature Publishing Group, v. 32, n. 8, p. 773, 2014.

NOOEAID, P.; ROETHER, J. A.; WEBER, E.; SCHUBERT, D. W.; BOCCACCINI, A. R. Technologies for multilayered scaffolds suitable for interface tissue engineering. **Advanced Engineering Materials**, 2014. Wiley Online Library, v. 16, n. 3, p. 319–327, 2014.

OZBOLAT, I. T.; MONCAL, K. K.; GUDAPATI, H. Evaluation of bioprinter technologies. **Additive Manufacturing**, 2017. Elsevier, v. 13, p. 179–200, 2017.

PAMPALONI, F.; REYNAUD, E. G.; STELZER, E. H. The third dimension bridges the gap between cell culture and live tissue. **Nature reviews Molecular cell biology**, 2007. Nature Publishing Group, v. 8, n. 10, p. 839–845, 2007.

PATI, F.; GANTELIUS, J.; SVAHN, H. A. 3d bioprinting of tissue/organ models. **Angewandte Chemie International Edition**, 2016. Wiley Online Library, v. 55, n. 15, p. 4650–4665, 2016.

PATRA, S.; YOUNG, V. A review of 3d printing techniques and the future in biofabrication of bioprinted tissue. **Cell biochemistry and biophysics**, 2016. Springer, v. 74, n. 2, p. 93–98, 2016.

POGHOSSIAN, A.; INGEBRANDT, S.; OFFENHÄUSSER, A.; SCHÖNING, M. J. Field-effect devices for detecting cellular signals. In: ELSEVIER. **Seminars in cell & developmental biology**. [S.l.], 2009. v. 20, n. 1, p. 41–48.

POPPER, H.; SCHAFFNER, F. et al. Liver: structure and function. **Liver: structure and function.**, 1957. New York (Toronto & London): McGraw-Hill Book Company Inc., 1957.

PULLETZ, S.; KOTT, M.; ELKE, G.; SCHÄDLER, D.; VOGT, B.; WEILER, N.; FRERICHS, I. Dynamics of regional lung aeration determined by electrical impedance tomography in patients with acute respiratory distress syndrome. **Multidisciplinary respiratory medicine**, 2012. BioMed Central, v. 7, n. 1, p. 44, 2012.

RANADE, N. V.; GHARPURE, D. C. Enhancing sharp features by locally relaxing regularization for reconstructed images in electrical impedance tomography. **Journal of Electrical Bioimpedance**, 2019. De Gruyter Open, v. 10, n. 1, p. 2, 2019.

RICHARDS, D.; JIA, J.; YOST, M.; MARKWALD, R.; MEI, Y. 3d bioprinting for vascularized tissue fabrication. **Annals of biomedical engineering**, 2017. Springer, v. 45, n. 1, p. 132–147, 2017.

RISS, T. L.; MORAVEC, R. A.; NILES, A. L.; DUELLMAN, S.; BENINK, H. A.; WORZELLA, T. J.; MINOR, L. Cell viability assays. In: **Assay Guidance Manual [Internet]**. [S.l.]: Eli Lilly & Company and the National Center for Advancing Translational Sciences, 2016.

RUSSO, S.; NEFTI-MEZIANI, S.; CARBONARO, N.; TOGNETTI, A. A quantitative evaluation of drive pattern selection for optimizing eit-based stretchable sensors. **Sensors (Switzerland)**, 2017. v. 17, 2017. ISSN 14248220.

SAMPSON, S. L.; SARAIVA, L.; GUSTAFSSON, K.; JAYASINGHE, S. N.; ROBERTSON, B. D. Cell electrospinning: an in vitro and in vivo study. **Small**, 2014. Wiley Online Library, v. 10, n. 1, p. 78–82, 2014.

SAYGILI, E.; DOGAN-GURBUZ, A. A.; YESIL-CELIKTAS, O.; DRAZ, M. S. 3D Bioprinting : A Powerful Tool to Leverage Tissue Engineering and Microbial Systems. **Bioprinting**, 2019. Elsevier B.V., p. e00071, 2019. ISSN 2405-8866. Disponível em: <https://doi.org/10.1016/j.bprint.2019.e00071>.

SEO, J. K.; LEE, J.; KIM, S. W.; ZRIBI, H.; WOO, E. J. Frequency-difference electrical impedance tomography (fdeit): algorithm development and feasibility study. **Physiological measurement**, 2008. IOP Publishing, v. 29, n. 8, p. 929, 2008.

SHAO, L.; GAO, Q.; XIE, C.; FU, J.; XIANG, M.; HE, Y. Directly coaxial 3d bioprinting of large-scale vascularized tissue constructs. **Biofabrication**, 2020. IOP Publishing, v. 12, n. 3, p. 035014, 2020.

SIRTOLI, V. G.; MORCELLES, K. F.; VINCENCE, V. C. Design of current sources for load common mode optimization. **Journal of Electrical Bioimpedance**, 2018. Sciendo, v. 9, n. 1, p. 59–71, 2018.

SKRYABIN, I.; RADCHIK, A.; MOSES, P.; SMITH, G. The consistent application of maxwell–garnett effective medium theory to anisotropic composites. **Applied physics letters**, 1997. American Institute of Physics, v. 70, n. 17, p. 2221–2223, 1997.

SVENSSON, T.; SWARTLING, J.; TARONI, P.; TORRICELLI, A.; LINDBLOM, P.; INGVAR, C.; ANDERSSON-ENGELS, S. Characterization of normal breast tissue heterogeneity using time-resolved near-infrared spectroscopy. **Physics in Medicine & Biology**, 2005. IOP Publishing, v. 50, n. 11, p. 2559, 2005.

SZULCEK, R.; BOGAARD, H. J.; AMERONGEN, G. P. van N. Electric cell-substrate impedance sensing for the quantification of endothelial proliferation, barrier function, and motility. **JoVE (Journal of Visualized Experiments)**, 2014. n. 85, p. e51300, 2014.

TASOGLU, S.; DEMIRCI, U. Bioprinting for stem cell research. **Trends in biotechnology**, 2013. Elsevier, v. 31, n. 1, p. 10–19, 2013.

TEKIN, E.; SMITH, P. J.; SCHUBERT, U. S. Inkjet printing as a deposition and patterning tool for polymers and inorganic particles. **Soft Matter**, 2008. Royal Society of Chemistry, v. 4, n. 4, p. 703–713, 2008.

TIKHONOV, A. N. Solution of incorrectly formulated problems and the regularization method. **Doklady Akademii Nauk SSSR**, 1963. v. 151, 1963.

TUCKER, A. S.; FOX, R. M.; SADLEIR, R. J. Biocompatible, high precision, wideband, improved howland current source with lead-lag compensation. **IEEE Transactions on Biomedical Circuits and Systems**, 2012. IEEE, v. 7, n. 1, p. 63–70, 2012.

UNAGOLLA, J. M.; JAYASURIYA, A. C. Hydrogel-based 3d bioprinting: A comprehensive review on cell-laden hydrogels, bioink formulations, and future perspectives. **Applied materials today**, 2020. Elsevier, v. 18, p. 100479, 2020.

VANDERBURGH, J. P.; FERNANDO, S. J.; MERKEL, A. R.; STERLING, J. A.; GUELCHER, S. A. Fabrication of trabecular bone-templated tissue-engineered constructs by 3d inkjet printing. **Advanced healthcare materials**, 2017. Wiley Online Library, v. 6, n. 22, p. 1700369, 2017.

VLIERBERGHE, S. V.; DUBRUEL, P.; SCHACHT, E. Biopolymer-based hydrogels as scaffolds for tissue engineering applications: a review. **Biomacromolecules**, 2011. ACS Publications, v. 12, n. 5, p. 1387–1408, 2011.

WANG, Q.; POLANSKY, J.; KARKI, B.; WANG, M.; WEI, K.; QIU, C.; KENBAR, A.; MILLINGTON, D. Experimental tomographic methods for analysing flow dynamics of gas-oil-water flows in horizontal pipeline. **Journal of Hydrodynamics**, 2016. Springer, v. 28, n. 6, p. 1018–1021, 2016.

WILSON, R. H.; NADEAU, K. P.; JAWORSKI, F. B.; TROMBERG, B. J.; DURKIN, A. J. Review of short-wave infrared spectroscopy and imaging methods for biological tissue characterization. **Journal of biomedical optics**, 2015. International Society for Optics and Photonics, v. 20, n. 3, p. 030901, 2015.

WU, H. Electrical impedance tomography for real-time 3d tissue culture monitoring. 2020. The University of Edinburgh, 2020.

WU, H.; YANG, Y.; BAGNANINCHI, P.-O.; JIA, J. Calibrated frequency-difference electrical impedance tomography for 3d tissue culture monitoring. **IEEE Sensors Journal**, 2019. IEEE, v. 19, n. 18, p. 7813–7821, 2019.

WU, H.; YANG, Y.; LIU, S.; BAGNANINCHI, P. O.; JIA, J. Multi-plane electrode configuration for 3d cellular assay of electrical impedance tomography. **ELECTRICAL IMPEDANCE TOMOGRAPHY**, 2018. p. 19, 2018.

XIAO, C.; LUONG, J. H. On-line monitoring of cell growth and cytotoxicity using electric cell-substrate impedance sensing (ecis). **Biotechnology progress**, 2003. Wiley Online Library, v. 19, n. 3, p. 1000–1005, 2003.

XU, T.; JIN, J.; GREGORY, C.; HICKMAN, J. J.; BOLAND, T. Inkjet printing of viable mammalian cells. **Biomaterials**, 2005. Elsevier, v. 26, n. 1, p. 93–99, 2005.

YANG, Y.; JIA, J.; SMITH, S.; JAMIL, N.; GAMAL, W.; BAGNANINCHI, P.-O. A miniature electrical impedance tomography sensor and 3-d image reconstruction for cell imaging. **IEEE Sensors Journal**, 2016. IEEE, v. 17, n. 2, p. 514–523, 2016.

YORK, T.; SUN, L.; GREGORY, C.; HATFIELD, J. Silicon-based miniature sensor for electrical tomography. **Sensors and Actuators A: Physical**, 2004. Elsevier, v. 110, n. 1-3, p. 213–218, 2004.

Review of
Scientific Instruments

ARTICLE

scitation.org/journal/rsi

# Hardware for cell culture electrical impedance tomography: A critical review

Cite as: Rev. Sci. Instrum. 92, 104704 (2021); doi: 10.1063/5.0053707
Submitted: 9 April 2021 • Accepted: 20 September 2021 •
Published Online: 5 October 2021

**K. F. Morcelles**[a] and **P. Bertemes-Filho**

## AFFILIATIONS

Department of Electrical Engineering, Santa Catarina State University, Joinville 89219-710, Brazil

[a] **Author to whom correspondence should be addressed:** kaue.morcelles@edu.udesc.br

## ABSTRACT

Human cell cultures are powerful laboratory tools for biological models of diseases, drug development, and tissue engineering. However, the success of biological experiments often depends on real-time monitoring of the culture state. Conventional culture evaluation methods consist of end-point laborious techniques, not capable of real-time operation and not suitable for three-dimensional cultures. Electrical Impedance Tomography (EIT) is a non-invasive imaging technique with high potential to be used in cell culture monitoring due to its biocompatibility, non-invasiveness, high temporal resolution, compact hardware, automatic operation, and high throughput. This review approaches the different hardware strategies for cell culture EIT that are presented in the literature, discussing the main components of the measurement system: excitation circuit, voltage/current sensing, switching stage, signal specifications, electrode configurations, measurement protocols, and calibration strategies. The different approaches are qualitatively discussed and compared, and design guidelines are proposed.

## I. INTRODUCTION

Human cell cultures (HCCs) are the basis of cell cultivation *in vitro*, enabling the growth of different types of cells (neural, muscular, and epithelial) in artificial and controlled environments.[1] HCCs are used in several biomedical applications, such as biological models, stem cell manufacturing and differentiation, tissue engineering for regenerative medicine, and bio-syncretic robots.[1–4] The basic structure of HCCs can be either 2D or 3D.[5] Independent of the application, the success rate of HCC experiments depends on several external interventions, including replacement of media, mechanical and electrical stimulation using bioreactors, introduction of biological factors, and drug delivery.[3,6,7] Each of these actions should happen at specific stages of the HCC, and in order to achieve the best outcomes and to automate the protocols, the state of the HCC should be monitored in real-time.

The literature provides several culture assessment protocols to evaluate the state of cells, used to sample information about cell adhesion, viability, and proliferation.[3] LIVE/DEAD tests are able to verify cell viability using fluorescent dyes; hemocytomers[8] and flow cytometers[9] are used to count resuspended cells; and immunohistochemistry is applied to identify abnormal cells using antigen staining.[10] However, these conventional assay protocols usually require staining, slicing, and/or resuspension of cells, which are invasive and destructive to the HCC, leading to burdensome laboratory work and interruption of the experiment.[11] In addition, conventional cell culture protocols are optimized for 2D monolayers and thus not compatible with dense 3D cell constructs and tissues: e.g., optical techniques, such as confocal and fluorescent microscopy, cannot penetrate layers deeper than a few micrometers,[12] and electronic microscopy protocols usually require freezing, which is destructive to the cells.[13] Because 3D cultures have received great attention due to better modeling capabilities compared to 2D cultures and animal models,[14,15] and due to its fundamental application in tissue engineering and regenerative medicine,[16] monitoring techniques should be able to comply with the three-dimensional paradigm. Therefore, the field lacks non-destructive assessment protocols capable of real-time monitoring of the HCC state.

Real-time monitoring techniques, especially for tissue engineering and regenerative medicine, should be non-invasive and non-destructive at the commercial level, to minimize interference with the biological function and therapeutic potential of the HCC.[17] Biosensors capable of indirectly measuring the chemical properties of media can be used to non-invasively monitor the state of the culture. Field Effect Transistors (FETs), for example, can measure the ion concentration of the extracellular media and use this information to infer tissue activity and properties.[18,19] However, chemical analysis has limited applicability in 3D cultures as it lacks information about the spatial distribution of processes inside the spheroid and because ionic diffusion degrades the tracking of local events.[20] Nano-scale imaging modalities, such as atomic force microscopy and scanning impedance imaging, were also applied in cell culture, but the temporal resolution is limited by the probe travel speed, and the hardware required is bulky, complex, and not suitable for parallel experiments or complex 3D structures.[21,22] Therefore, techniques using image reconstruction are needed in order to infer properties occurring beyond the boundaries of the sensor with sufficient spatial resolution. One biologically compatible technique, capable of non-invasively characterizing the interior properties of biological samples, is the Electrical Impedance Tomography.

Electrical Impedance Tomography (EIT) is an imaging technique that creates 2D or 3D images of the electrical conductivity and permittivity distribution of a sample.[23,24] The method consists of measuring the electrical impedance between multiple electrodes placed on the external surface of the object and reconstructing the internal admittance distribution using the measured information.[25] Real-time EIT monitoring was applied in industrial processes, such as flow dynamics and concrete damage characterization,[26,27] and biomedical applications, such as lung ventilation, brain function, and gesture recognition.[28,29] Image reconstruction is a mathematical ill-posed problem, and several algorithms were proposed in the literature to prove and obtain a unique solution from a specific set of EIT measurements.[25,30–32] Compared to conventional real-time imaging techniques, such as x-ray and magnetic resonance, EIT has the advantages of being portable, less costly, non-invasive, safer, easily automated, fast, and providing high throughput.[24,25,33] However, low spatial resolution, electrode contact issues, and the inherent ill-posed problem are the major drawbacks that limit the application range of the technology. Although EIT is often applied in the meters/centimeters range, microscopic EIT is also possible, being first demonstrated by Griffiths *et al.* in 1996[34] and York *et al.* in 2004.[35]

The application of bioimpedance in cell cultures was first proposed by Giaever and Keese, where a gold electrode in the bottom of the culture measured the electrical impedance of cells and media, which was used as a label-free technique to evaluate cell proliferation, viability, toxicity, barrier function, and differentiation.[36–40] However, bioimpedance spectroscopy alone lacks the spatial resolution needed to track the culture state although impedance mapping techniques can provide spatial information to a limited degree.[20] Using the image reconstruction capabilities of EIT, one can evaluate the distribution of electrical properties (conductivity and permittivity) inside the culture well and, thereafter, predict the biological state of the cells.[41] This is because cells have significantly different electrical properties compared to the culture media, which creates a contrast in the EIT image that depends on the frequency.[24,42] That way, HCCs can be non-invasively monitored in real time by the user, as the application of electric signals to measure bioimpedance does not interfere with the state of the culture. Compared to conventional cell culture assays, EIT has lower cost, portability, automated functionality, and real time operation and, most importantly, is non-invasive and non-destructive and therefore able to analyze different time points of the same HCC.[43]

EIT systems are composed of an analog front-end, a signal pre-processing module, and an image generation software. The software consists of the forward problem modeling, which describes how the internal properties of the sample object affect the boundary electrode measurements, and the image reconstruction algorithm, which calculates the internal properties of the object based on experimental measurements.[25,32] The pre-processing module is responsible for the filtering, gain adjusting, demodulation, analog-to-digital signal conversion, and communication with the host computer, being implemented using microcontrollers and/or an FPGA (Field Programmable Gate Array).[25,44,45] The analog front-end is usually composed of (i) an excitation circuit that delivers current or voltage to the sample; (ii) a voltage/current sensing stage that measures the electrical response to the excitation; (iii) a switching system that controls which electrodes are being used; and (iv) the electrode configuration itself.[24,25,46,47] The generalized EIT system is described by the block diagram shown in Fig. 1, which contains the main blocks of the signal chain.

The analog front-end plays a major role in EIT performance, affecting parameters such as resolution, noise, maximum load, speed, sensitivity, and safety.[23,25] The literature provides different implementations.[24,25,46,47] However, HCCs have several particularities and limitations that must be taken into account when designing the front-end: (i) the reduced size of the electrodes increases the current density at the vicinity of injection, which may lead to cell harming, spike noise near electrodes, and high contact impedance;[24,48–51] (ii) the DC signal drift due to the high conductive electrolytes presented in culture media;[52] (iii) the simultaneous biochemical processes occurring during HCC experiments, such as drug response assays, masking each other in the net conductivity change;[53] and (iv) the small voltage variation in the sensing electrodes due to cell dynamics, which can be easily overwhelmed by noise and artifacts.[52,53] The objective of this review is to analyze the different hardware systems presented in the literature and use the obtained information to propose design guidelines. This work is focused on the analog front-end, approaching excitation circuits, voltage/current measuring systems, switching stage, electrode configuration, and types of signals applied.

## II. EXCITATION CIRCUIT

Electrical excitation can be applied to tissue samples using either voltage or current signals. Voltage sources are usually easier to design and provide higher bandwidth,[54,55] but they lack current control. Current sources, on the other hand, can precisely control the current injected, making it independent of the conductivity and electrode impedance of the sample. This control is important in cell culture applications because the small size of the electrodes leads to high current densities, which may cause local damage to cells. In addition, because current sources can generate output currents fixed at the maximum recommended level, they provide better sensitivity fields and image distinguishability than voltage sources.[24,56] On the other hand, voltage excitation is conventional in most commercial impedance analyzers; therefore, its use is still fairly common in EIT applications.[41,57] This chapter explores the different excitation sources proposed in the literature for cell culture EIT.

### A. Dedicated current sources

The EIT system proposed by Yang and Jia,[58] called mfEIT, is a multi-frequency current source, with adjustable amplitudes up to 5 mA and bandwidth from 10 kHz to 1 MHz. The source is based

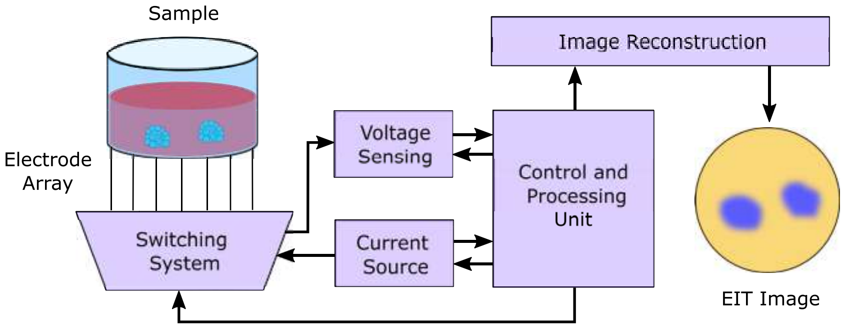

**FIG. 1.** Generalized EIT system for cell culture monitoring.

on the enhanced Howland source topology (Fig. 2), with an output impedance of 10 MΩ at 10 kHz. The input voltage was generated by two Numerically Controlled Oscillators (NCOs) and a Digital-to-Analog Converter (DAC) with adjustable external reference, followed by an adjustable Low Pass Filter (LPF) to smooth the voltage. The external reference controls the amplitude using an 8-bit resolution DAC, and the NCOs superimpose two sine functions with controlled frequencies. The superimposed frequencies are used to generate frequency-difference EIT (FDEIT) measurements simultaneously.[58] They also designed a shut-down stage to turn-off the source if current reaches non-safe amplitudes.[58] This excitation circuit was applied in several experiments reported by the Agile Tomography Group (University of Edinburgh), including cell-drug response, long-term monitoring, and 3D imaging of MCF-7 cancer cells.[48,49,52,53,59–62]

A single-ended Howland source was also implemented in the design of the KHU Mark2 EIT system.[63] The simultaneous frequency approach (similar to the one used by Yang and Jia[58]) was performed using two DACs (16 bits AD9783) with different sinusoidal signals (up to three frequencies each), which were summed and fed to the Howland source input. It also incorporates two 10-bit DACs to remove DC components from the excitation current.[63] The source was designed to operate from 10 to 500 kHz, using 10 kHz as default frequency. The KHU Mark2 system was applied in the multi-plane micro EIT sensors proposed by the Impedance Imaging Research Center at Kyung Hee University.[64–66]

Single-ended current sources generate high common-mode voltages at sensing sites,[67] which is problematic for the voltage sensing stage, especially at high frequencies. The issue can be reduced using symmetrical current sources. Liu *et al.* addressed this problem by implementing a symmetrical current source to drive the lateral injection electrodes of the KHU Mark2 system, using two single-ended Howland circuits as source and sink.[65] However, this approach is risky, because any mismatch between the current sources can lead to large common mode values, and common-mode feedback should be implemented.[67] Symmetrical current injection is important because the Common Mode Rejection Ratio (CMRR) of the measuring system is not infinity, especially at high frequencies: Liu *et al.* reported a CMRR drop from 98 dB at 1 kHz to only 60 dB at 50 kHz, caused by the switching network capacitances and amplifier non-idealities.[65]

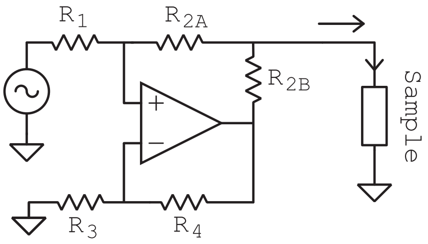

**FIG. 2.** Enhanced Howland current source.

The output impedance of current sources is significantly degraded by stray capacitances, introduced by the instrumentation amplifier, cables, electrodes, and switching stage. This capacitance can be compensated by the addition of an active component in parallel with the current source output, behaving as an inductor in the desired frequency interval.[68] Oh *et al.* implemented generalized impedance converters (GICs) (Fig. 3) to increase the output impedance of the current sources.[63] Although being able to nulling the stray capacitance at a certain frequency using resonance, it is difficult to design the circuit for multi-frequency operation. The solution proposed in this work was the implementation of four GICs (one for each frequency interval, selected using MAX4545 switches) and digital potentiometers (DS1267) as calibration elements to fine tune the resonance point.[63] The GICs were able to achieve impedances higher than 1.0 MΩ at the whole frequency range, with an average value of 4.57 MΩ after calibration.

The Howland current source is the most common choice for cell culture assays, probably due to its flexibility and easy application using discrete components.[42,69] However, other circuits, such as discrete Operational Transconductance Amplifiers (OTAs) and integrated CMOS current sources,[70,71] may also be suitable for cell-culture EIT applications.

## B. Commercial impedance analyzers

Although voltage sources are not the ideal choice for medical bioimpedance applications, they are the conventional approach on commercial impedance analyzers. This is because most impedance analyzers are of general purpose, and non-biological materials usually have higher tolerances to current amplitudes than biological tissues. Therefore, voltage excitation was usually applied in experiments that focused on the electrode configuration rather than the electronic hardware validation. Commercial impedance analyzers also provide ready-to-use built-in sensing hardware, which reduces design complexity. The advantage of using commercial systems is the wide range of frequencies provided and the robustness. However, the bulky size, lack of flexibility, and higher cost are major

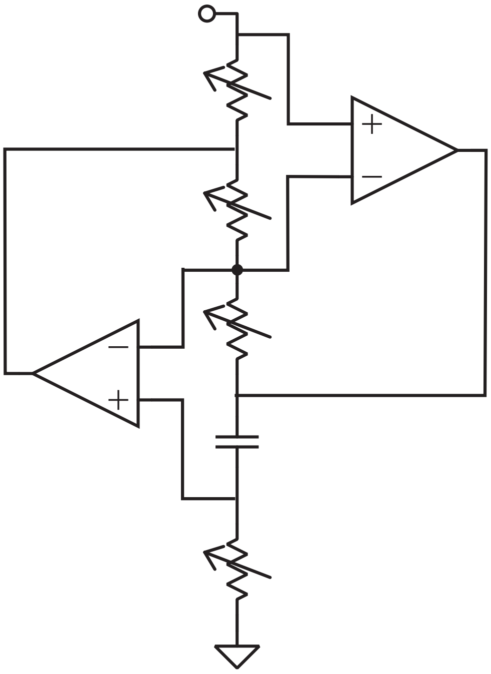

**FIG. 3.** Generalized Impedance Converter (GIC) simulating an inductor.

drawbacks. In addition, commercial impedance analyzers are not optimized for EIT, needing external switching and synchronization systems, as well as depending on native communication protocols. This extra circuitry combined with design inflexibility can limit the EIT frame rate and, consequently, the applicability on real-time EIT monitoring. Table I displays the papers that implemented commercial impedance analyzers, the models of the instruments, the excitation amplitude, and the frequency range.

## III. VOLTAGE/CURRENT MEASUREMENT AND DIGITALIZATION

Any bioimpedance system is composed of an excitation module and a signal sensing circuit. Conventionally, if current is used as excitation, voltages should be sensed and vice versa. This chapter summarizes the signal sensing circuits found in the literature for cell culture EIT. Similar to the excitation circuits, some particular aspects of cell cultures require specific design rules, which are discussed in Subsections III A and III B.

**TABLE I.** Commercial impedance analyzers applied in cell culture EIT for both voltage excitation and signal sensing.

| Paper | Impedance analyzer | Amplitude | Signal frequency |
|---|---|---|---|
| 57 | Solartron SI1260 + SI1294 | 0.5 mA | 10 Hz–100 kHz |
| 41 | Agilent 4294A | 141 mV | 10 kHz |
| 89 | Agilent 4294A | . . . | 12.5 kHz–500 kHz |
| 78 | Autolab PGSTAT 30 | 10 mV | 25 Hz to 1 MHz |
| 73 | Tektronix AFG320 | . . . | . . . |
| 96 | Alpha-A Novocontrol | 100 mV | 200 kHz |
| 51 | HIOKI IM3570 | 0.1 mA | 10 kHz–1 MHz |

### A. Voltage measurement

The voltage sensing stage is responsible for reading and amplifying the potential difference generated by the excitation signal, filtering noise, and DC components and digitizing the measurements to allow processing by the digital unit. In cell culture EIT, conductivity changes are subtle; thus, voltage variation is significantly small.[43] The circuit diagram in Fig. 4 exemplifies a voltage measurement system using lock-in demodulation.

The first stage of the sensing circuit amplifies the differential signal, while rejecting the common-mode voltage and noise. Yang and Jia implemented an instrumentation amplifier,[58] whereas Oh *et al.* used two input buffers and a differential amplifier (AD8130) with unity gain as the first stage of the KHU Mark2 system.[63] To reject DC components and out-of-band noise, a band-pass filter followed the differential amplifier.[63] In addition, to increase both noise and cross-talk immunity, the KHU Mark2 system implemented triaxial cables with driving shield in both excitation and sensing I/Os.[63] Similarly, Linderholm *et al.* implemented two buffers followed by a differential amplifier (AD8065) as a pre-amplifier stage in the Agilent 4294A impedance analyzer.[41,72] An alternative approach is presented by Dharia *et al.*: a reference impedance is placed in series with the excitation system and the sample electrode pair, forming a voltage divider that is sensed by a single buffer (OPA356).[73] This approach, however, only works with bipolar measurements and, thus, is not suitable for most EIT protocols.

The second stage of the circuit amplifies and adjusts the signal, sometimes also providing level shifting to comply with single-supply Analog-to-Digital Converters (ADCs). In EIT, the potential differences at the electrodes pairs present wide ranges of amplitude due to the different pair combinations in each measurement.[52,59] Hence, a fixed gain is not the optimal choice, as ADC resolution would be poor for small signals. Therefore, Programmable Gain Amplifiers (PGAs) are usually applied in the second stage to adapt the gain accordingly.[58,63] Yang and Jia implemented a PGA with adjustable gain from 0.56 to 70 V/V, providing best resolution and avoiding signal saturation.[58] The KHU Mark2 system designed a dedicated PGA using the AD8039 high frequency operational amplifier (OPAMP) and external digipots (DS1267) to set the closed-loop gain.[63]

The third sensing stage is responsible for digitizing the signal and further filtering it to be processed by the software. Lock-in demodulators are often used in this stage, because of its significantly narrow passing band, that can be finely tuned to match the excitation signal and provide a high signal-to-noise ratio (SNR) and fast extraction of the real and imaginary parts of the voltage.[24,58,63] The lock-in demodulator can be implemented in the analog domain, as in Dharia *et al.*,[73] that implemented the SR844 lock-in amplifier (Stanford Research). Its output was sampled by a 1 kS/s ADC (ITC 1600, InstruTECH).[73] In this approach, ADCs with low sampling rate can be used, as the output of the analog lock-in demodulator have low frequency content. However, with the evolution of high speed/high resolution ADCs, digital lock-in demodulators are typically used because of their flexibility and easy implementation. Yang and Jia digitized the signal from the PGA using a 16 bit/10 MS/s ADC followed by two parallel simultaneous multi-frequency digital quadrature demodulators (SMFDQD), which were

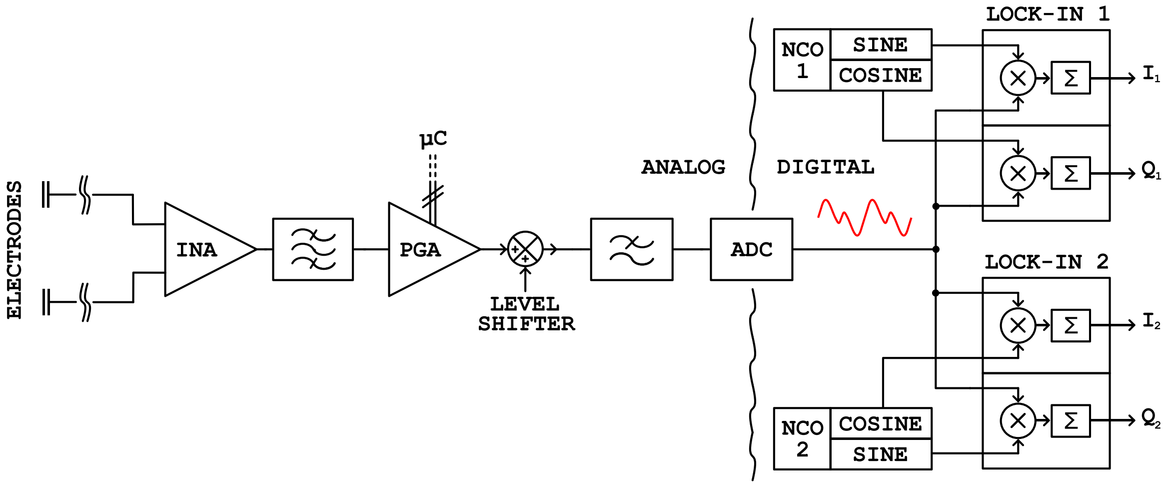

**FIG. 4.** Example of the measurement system using an instrumentation amplifier, a programmable gain amplifier, filters, level shifting, and the simultaneous multi-frequency digital quadrature demodulation (SMFDQD) based on Yang and Jia.[58]

implemented using the Multiply-Accumulator (MAC) cores of an FPGA.[58] Figure 4 describes a measuring system based on this idea. To maintain a constant number of points per period of signal, the sampling frequency of the ADC was dynamically modified, according to the signal input.[58] The KHU Mark2 system implemented a similar approach, using the AD9235 ADC (12 bits/65 MS/s) and collecting 1000 samples per signal period, followed by a digital lock-in demodulator also implemented inside the FPGA.[63]

Using averaging, the KHU Mark2 system achieved SNR of 75 dB up to 84.5 dB.[63] The CMRR was 96.5 dB in the entire band when using ideal electrodes. To predict the effective CMRR, impedance of electrode-skin contact was modeled using RC circuits. The resulting CMRR was then 85.8 dB for electrodes in both inputs and 68.2 dB for one electrode in only one input.[63] These results show the effects of common-mode electrode impedance and mismatches in the total CMRR of the circuit.

To increase the speed of EIT measurements, the mfEIT system, proposed by Yang and Jia,[58] implemented two identical voltage measuring channels, which almost doubled the frame rate.

## B. Current measurement

Current measurement is essential in EIT systems that apply voltage excitation and may be performed by measuring the current in the sensing electrodes (solving the Neumann conditions[33]) or by measuring the current from the excitation source and the voltages from the sensing electrodes. The second is most conventional and easily implemented in EIT, being often applied when using commercial impedance analyzers.[41,50,72] Current measurements are also used to trigger protection stages in micro EIT, shutting down measurements with unsafe values.[58]

The current measurement is also important for correct image reconstruction, as leakage current may lead to errors in EIT images. This is particularly significant in frequency-difference EIT, as parasitic impedances vary with frequency.[43,53] One way of dealing with the problem is measuring the current. The KHU Mark2 system provides current measuring via shunt resistors and instrumentation amplifiers.[63,66] This approach is effective; however, current sensing depends on the resistor value, which may degrade the current source load capability. In addition, large resistors combined with the input capacitances of the instrumentation amplifier may generate current leakage in high frequency. Another approach is the use of transimpedance amplifiers, which combines high current-to-voltage gain and low input impedance, reducing the current leakage. This method is typically implemented in voltage excitation systems[74–77] but can be applied in current excitation as well.

Current sensing is most common in microelectrode arrays, usually applied to obtain impedance mapping of 2D cell monolayers. Manickam *et al.* presented a dedicated microelectrode array system for culture monitoring.[74] The electrodes were embedded in a CMOS chip, and each one was connected to a CMOS transimpedance amplifier followed by a lock-in stage.[74] A similar technique was proposed by Chi *et al.* and Viswam *et al.*[75–77] Because current is being measured, voltage is used as the excitation source and can be applied by a common large electrode[76] or by another microelectrode from the array.[77] Although cell mapping is not strictly EIT, the arrays and chips could be easily adapted to perform tomography.

## IV. SWITCHING STAGE

EIT systems can be composed of many electrodes, with applications usually ranging from 16 to 360 sensing electrodes placed in a small area.[52,66] Therefore, having one circuit for each electrode pair is often impractical. The common approach is to use a switching stage to connect specific electrode combinations to the excitation source and sensing circuit.[25] The correct design of the switching system is important in EIT, as system speed and measurement protocols are affected by its architecture. In addition, switches introduce stray capacitances, causing current leakages and, consequently, high frequency errors.[53]

Yang and Jia proposed a configurable multiplexing system, designed for arbitrary current patterning and sensing, capable of switching up to 32 electrodes. Each electrode can be connected to any terminal of the current source, via 32 dual switches, or any voltage sensing channel, using cascaded 8 × 16 crosspoint-switch arrays.[58] The switching system is capable of working in a semi-parallel mode (using two voltage measuring channels), which doubles the frame-rate capability.[58] The introduction of more measurement channels can further improve the speed at the cost of system complexity.

Fast switching systems are needed for high frame rates. However, high frame rates may introduce errors in the measuring system due to delays in the channel selection. At 100 fps, Yang and Jia switching array[58] introduced 25 mV spikes at the sensing circuit output, which was almost two times the actual signal.[43] A threshold filter managed to eliminate the noise, and the system was able to push the frame rate up to 1014 fps.[58]

Lee *et al.* implemented low-voltage T-switches to allow bidirectional signals in the KHU Mark2 system.[66] The modular topology of the KHU Mark2 allows application of specific switching configurations, depending on the number of electrodes and measurement protocol.[63] For instance, Liu *et al.* implemented ADG708 multiplexers, controlled by an EPM3064A, which is a complex programmable logic device (CPLD).[64,65] This switching network connected 360 electrodes to the 15 Mark2 native voltage sensing channels. As switch capacitance greatly influences the performance of the current excitation, a large number of electrodes may require limited measurement combinations to reduce the number of required switches.[64] Liu *et al.* reduced the number of switches by restricting voltage sensing to only horizontally adjacent electrode rows, although not restricting it in the vertical direction.[64]

The most effective method to reduce the parasitic effects caused by the switching stage is to simply remove the stage from the design, using parallel systems. The major drawback of parallel EIT systems is the hardware complexity, as it requires multiple analog channels (one for each electrode pair) containing a dedicated current source and voltage sensing circuit. Oh *et al.* used a modular approach to design the parallel KHU Mark2 EIT system.[63] Parallel operation is obtained using impedance measurement modules (IMMs), which are standardized channels in the KHU Mark2. The author presented a 16 electrode parallel system, but 32 or 64 electrodes can be achieved by adding more IMMs.[63] To control each IMM, an intra-channel network was designed using LVDS (low-voltage differential signaling) serial communication, controlled by a high-capacity FPGA. The FPGA triggers and receives measurements from all IMMs using a pipeline structure.[63] In addition to eliminating the parasitic elements and the cross-talk noise introduced by switches, this approach allows the use of any measurement protocol (adjacent, opposite, and optimum) and increases the speed of the EIT system. Using 16 electrodes and the pipeline structure, the KHU Mark2 system achieved 100 scans/s.[63]

Most of the reviewed papers described applications using commercial multiplexing modules or did not specify the switching system. Table II summarizes the switching modules implemented by each paper, as well as the number of electrodes in the system.

**TABLE II.** Switching system models and number of electrodes of each reviewed system.

| Paper | Switch model | Number of electrodes |
|---|---|---|
| Canali *et al.*[57] | Keithley 7001/7012 | 16 |
| Linderholm *et al.*[41] | AD75019 | 16 |
| Liu *et al.*[51] | Agilent 34970A | 80 |
| Dharia *et al.*[73] | MAX451 | 8 |
| Sun *et al.*[50] | CD22M3494 | 16 |
| Rahman *et al.*[78] | Reed relays | 8 |
| Yang and Jia[58] | SPST/cross-point arrays | 16 |
| Lee *et al.*[66] | MAX4529 | 360 |
| Liu *et al.*[65] | ADG708 | 360 |
| Oh *et al.*[63] | No switches | 16 |

## V. SIGNAL FREQUENCY AND MEASUREMENT PROTOCOLS

There are two major imaging paradigms in EIT: absolute impedance imaging and difference impedance imaging.[25] Absolute imaging can represent the actual conductivity distribution of the sample, thus leading to accurate predictions and correlations with biological information. However, the difficulty of accurately predicting the contact impedance, electrode position, current leakages, and other circuit parasitic effects makes the absolute imaging complicated and often impractical.[24,25,53] Difference imaging (DEIT), on the other hand, maps the variation of conductivity distribution relative to a reference point, which is more feasible. Depending on the parameter used for DEIT (frequency or time), single-frequency or multi-frequency signals are required.

### A. Single-frequency excitation

Single-frequency signals are usually applied in Time-Difference EIT (TDEIT). TDEIT measures how conductivity changes in time from an initial point and regions with sufficient variation contrast with the static background. The conductivity changes can be then correlated with biological transients, such as cell growth, drug response, and electroporation.[25,33,57,59,79] Single-frequency applications with TDEIT are the most common approaches in cell culture EIT due to its easy generation and processing. Applications reported in the literature include both 2D and 3D cultures, with frequencies ranging from 10 kHz to 1 MHz.[50,51,57,59,61,62,66,80] In addition to the simple implementation process, parasitic components and systematic error sources are usually time invariant for short periods of time, and they can be easily eliminated by difference imaging. However, this is not true for long-term cell culture applications, as the background media changes its properties due to evaporation and cell metabolism, losing the initial reference of the TDEIT.[43]

### B. Multi-frequency excitation

Multi-frequency signals are required in Frequency Difference EIT (FDEIT). FDEIT images the conductivity variations between two or more frequencies, therefore eliminating frequency independent anomalies. Hence, this technique can distinguish regions with different types of frequency behavior, such as cells and electrolytes, or different types of tissue in a co-culture.[25,33,57,59] For instance, TDEIT cannot distinguish if changes in conductivity are caused by ionic diffusion or cell apoptosis, as both may increase the conductivity at the same frequency. However, FDEIT can detect the region with cell death because the cell membrane is tightly related to the

$\beta$-dispersion, whereas the electrolyte alone does not present dispersion below MHz.[24,43] This type of strategy is preferable for long-term monitoring because it can distinguish between conductivity variations caused by cell grow and cell metabolism.[48,59]

The simplest multi-frequency excitation method consists of applying one frequency at a time. However, this approach can significantly reduce the frame rate due to the increase in the measurement time of each channel. One way of overcoming this problem is to apply multiple frequencies in the same signal, which can be done by simply adding two sines with different frequencies.[43] Although this method works for two frequencies, it is difficult to add large numbers of harmonics without degrading signal quality.[81] Therefore, if several harmonics are needed, optimized broadband-signals should be considered. Broadband signals are periodic signals that contain several harmonics with pre-defined amplitudes. Some broad-band signals, such as the multisine and the discrete interval binary sequences (DIBS), can be optimized to provide the selected harmonics while maintaining signal quality in terms of SNR and resolution, which are important in EIT.[81]

To select the desired frequencies, one must understand how the components of the cell culture change with frequency. In single-cell imaging, for instance, low frequencies can give information about the shape, middle frequencies about the membrane, and high frequencies about the intra-cellular content,[73] as illustrated in Fig. 5. This occurs because the impedance dependence on frequency is governed by three main dielectric dispersion regions: $\alpha$-, $\beta$-, and $\gamma$-dispersions, each one providing different biological information.[24] The most important dispersion mechanism is the $\beta$-dispersion, which characterizes the cell membrane. Lower and higher frequencies usually yield information about the cell media distribution and cytoplasm, respectively.[24]

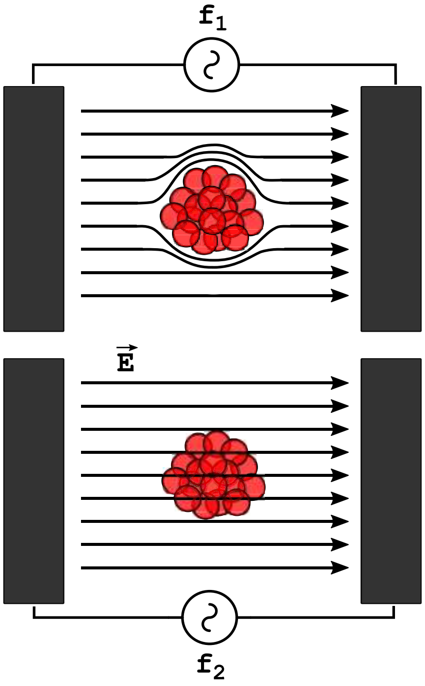

**FIG. 5.** Current paths using low frequency ($f_1$) and using high frequency ($f_2$) in the presence of cells.

## C. Frequency selection

In both single-frequency and multi-frequency EIT, frequency values should be carefully selected to provide the desired information about the culture. Depending on the cell culture geometry (2D or 3D), the frequency value may lead to different interpretations. In 2D cultures, cells usually grow on top of the electrodes, which correspond electrically to a series equivalent between contact impedance, tissue, and culture media.[20] This leads to a tissue impedance dominance in low frequency measurements (<1 kHz). This situation is ideal to characterize the contact impedance in electric cell-substrate impedance sensing (ECIS), yielding information about cell spreading, barrier function, and adhesion.[36] However, the high interface impedance can generate spike noises in EIT images, due to the high local sensitivity of microelectrodes,[49] as well as reduce the maximum excitation current due to the limited voltage compliance of the excitation circuit. Therefore, low frequencies are usually not recommended for 2D microelectrode applications.

On the other hand, the electrodes are usually not in contact with the tissue sample in 3D cultures, which results in a parallel equivalent circuit between tissue and media.[20] Therefore, low frequencies measurements are dominated by the media impedance, which is low enough to be driven by the current source. In this case, low frequency measurement can yield information about tissue size and distribution,[82] as the electric field will avoid the regions covered by the tissue.

Middle frequencies (10 kHz–MHz range) characterize cell membrane properties and can differentiate between cell types using the $\beta$-dispersion, whereas high frequencies (>MHz) provide better information about cell interior, i.e., the cytoplasm.[20,24,48] Compared to low frequencies, middle and high frequencies are less affected by the contact impedance, but the conductivity contrast between cell and media is lower. Therefore, an optimum frequency should exist. Frequencies in the range of 10–100 kHz, with calibration and compensation techniques (see Sec. VI), are usually implemented in single-frequency EIT, as sufficient image contrast can be achieved avoiding the high contact impedance. However, the best frequency range is often application-dependent, and small microelectrodes can suffer from high impedance even at the MHz range.[83]

## D. Measurement protocols

The input parameters for EIT image reconstruction are the voltage measured using different excitation/sensing electrode combinations.[33] The ill-posed problem suggests that all excitation/sensing combinations should be executed in order to increase the accuracy. However, this approach is unpractical, as it significantly increases the scan time and hardware/software complexity. Therefore, different measurement protocols were developed in EIT, each one with characteristics suitable for a specific range of applications.[25,33] This subsection discusses these protocols and their applicability in cell culture EIT.

Because of the contact impedance, which is more significant in microelectrodes (see Sec. VII), tetrapolar measurements are the basis of measurement protocols. This scheme uses one pair of electrodes to inject current and another pair to measure voltage, and because ideally no current flows through the sensing electrodes, contact impedance is mitigated.[24] Moreover, half of the measurements in tetrapolar EIT can be considered redundant due to the reciprocity principle.[24,25] However, if leakage currents are significant, the reciprocity principle is invalid,[43] and the whole set of measurements is needed to generate an image.

The most common measurement protocol is the adjacent injection/sensing. The strategy consists of injecting and sensing signals only in adjacent pairs of electrodes.[25,84] The adjacent protocol favors the boundary regions, with resolution dropping significantly at the center of the sample.[52,59,66] Several of the reviewed systems implemented the adjacent protocol in cell culture imaging.[48,50,52,59,60,85–87]

The counterpart of the adjacent strategy is the opposite protocol. In this case, current is injected via opposite electrodes and voltage is sensed at the remaining pairs.[25,84] Different from the adjacent, the sensitivity of the opposite protocol is focused to the center of the sensing region.[4,43,84] This method is usually called the Sheffield scheme.[88] In the cell culture context, Rahman *et al.* implemented bipolar opposite measurements to obtain spatial-wise impedance information of 2D monolayers.[78,89] One variation of the opposite protocol is the polar-offset, which injects current through opposite electrodes and measures voltages differences between each electrode and a center (Ref. 57). This method was applied by Canali *et al.* and can achieve better central information than the conventional opposite scheme.[57] Other advantages of this method is the uniformity of the field and higher sensitivity to insulating anomalies.[57] This strategy was also implemented by Liu *et al.*, Lee *et al.*, and Yao *et al.*[65,66,80]

Finally, Adaptative Current Tomography (ACT) applies current excitation to several electrodes at the same time to create arbitrary spatial patterns of current, while the voltages of each electrodes are measured.[85,90] Compared to the other protocols, ACT has higher sensitivity, distinguishability, and capability of measuring absolute impedance.[85,91,92] However, these advantages come at the cost of hardware complexity because each electrode requires its own measurement channel. To the date of this review, no cell culture EIT device applied ACT, although the KHU Mark2 system has the parallel operation capability to perform the strategy using 16 electrodes.[63]

Measurement protocols can be highly constrained by the hardware, especially by the switching stage. For instance, Lee *et al.* implemented different electrode arrays for current injection and voltage sensing (refer to Sec. VII).[66] In this case, the current electrodes are only on the left and right walls of the testing chamber. The injection protocol consists of one primary and two secondary currents: the first is a uniform density field in the x direction, created using all injection electrodes at the same time, whereas the second currents are diagonal, implemented to obtain information of the y and z directions.[66] On the other extreme of the spectrum, the Yang and Jia mfEIT system allows for arbitrary protocols, with the switching system capable of connecting any electrode to either a voltage or current terminal.[58]

## VI. ERROR SOURCES AND CALIBRATION STRATEGIES

EIT image reconstruction is an ill-posed problem; therefore, even small errors in the voltage measurement can generate large errors in the calculated conductivity.[33] Therefore, error sources are major concerns that should be identified and calibrated. This section describes the main systematic errors in cell cultures and the calibration strategies proposed in the literature.

### A. Error sources

The electrode array is one of the main sources of errors in cell culture EIT, including contact impedance and position errors. Contact impedance is significantly higher in microelectrodes, and images may be completely degraded by it, especially at low frequencies (<10 kHz).[65] Liu *et al.* showed that not only the size contributes to the increase but the double-layer capacitance presents higher dominance when the contact surface is down-scaled.[51] Contact impedance effects can be reduced using higher frequencies and calibration methods.[51,53] In addition, coating techniques can increase the effective surface of the contact without changing the electrode geometry, and coating materials such as platinum-black have been described in the literature for this purpose.[73,76] Another non-ideality is the electrode position error, which may generate artifacts in the final image.[57] However, position errors are easy to calibrate in cell culture EIT because electrodes are always fixed in the well.

In addition to contact impedance, mismatches between the traces and cables that connect the electrodes to the electronic circuit can produce image errors due to impedance differences and pickup noise. Yang *et al.* minimized the problem using impedance matching to equalize the length of the printed circuit board (PCB) traces carrying the signal to the electrodes.[52]

Another error source is the background media. For instance, the volume increase caused by the insertion of cells, particularly in 3D cultures, is sufficient to cause measurement errors due to the small size of the chamber.[43,86] In order to keep a constant volume in the sensor, the displaced liquid can be pipetted out of the well.[43] Canali *et al.* also verified that slight tilts in chamber incubators displaced liquid to one side, creating an asymmetrical distribution of media.[93] Both cases generate mismatches between the finite-element model (FEM) and the experimental setup. In the first case, the cell media should be removed to maintain the total volume, and in the second case, the tilt can be mechanically compensated.[43,57]

Finally, the parasitic components of the measurement electronic circuit can generate artifacts in the EIT image, especially at high frequencies.[53] Stray capacitances generate current leakages that are frequency dependent. These stray capacitances are generated by cables, electrodes, switching system, sensing circuit, and excitation signal output. Leakage currents have three major implications in EIT systems: (i) the applied current is not equal to the one generated by the current source, (ii) current flows through the sensing electrodes, and (iii) the reciprocity principle is no longer valid.[24,43] The first results in mismatches between the model and experimental setup, the second makes the measurement dependent on electrode impedance, and the third eliminates the possibility of ignoring the redundant measurements. The problems generated by stray capacitances are reduced by proper circuit design, using driven triaxial cables and correctly selecting the electronics,[24,63] and calibrated using homogeneous medium (Ref. 53).

Stray capacitances and leakage currents can be reduced using voltage-driven triaxial cables. This cable configuration is composed of three layers: the center wire that carries the signal, a middle coaxial layer with voltage identical to the main line, and an external layer

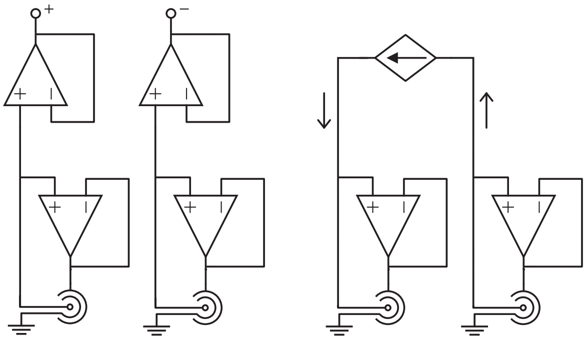

**FIG. 6.** Voltage-driven triaxial cables using buffers, providing shielding for both current and sensing channels.

connected to ground.[63] The external layer provides shielding from external noise, whereas the internal layer reduces the capacitance between the line and ground. The typically driven guard circuit is presented in Fig. 6, where buffers are used to drive the internal shield of both excitation and measuring lines.

Another error source arising from circuit elements is the common-mode voltage: the sensing stage should measure only differential voltages; however, the CMRR is finite and decreases with frequency, especially in the presence of stray capacitances and electrode mismatches.[25,63,65] If the CMRR is limited, common-mode voltages can be reduced using the symmetrical topologies of excitation circuit presented in the literature.

### B. Calibration strategies

Systematic errors can be minimized using calibration. Calibration in homogeneous medium is frequently used in micro-EIT systems.[41,53,63,66,73] It is a holistic approach that considers the systematic errors invariant and not dependent on the sample properties. In this method, a reference set of measurements are collected using a homogeneous medium (usually cell media or PBS) and the desired EIT measurement protocol. Calibration factors (sometimes referred to as cell constants[24,41]) are then calculated to adequate the real and imaginary parts to the expected values. These factors are then assumed to be invariant and are later applied to the actual measurements.

Multi-frequency calibration is particularly important in miniature EIT using FDEIT because systematic errors vary significantly with frequency, introducing differential errors in FDEIT that can easily overcome the small conductivity of the cells, creating large image anomalies at the background.[53] To solve this issue, Wu *et al.* proposed the calibrated frequency-difference EIT (CFDEIT) method.[53] CFDEIT uses a homogeneous reference media to perform a set of measurements with the frequencies of interest. Because the media conductivity is frequency independent, the difference between voltages at different frequencies will be solely defined by the systematic errors. CFDEIT is significantly more powerful than the conventional FDEIT, eliminating error anomalies and enhancing contrast.[53]

Calibration can also be automated and applied directly by hardware. Oh *et al.* proposed an automatic current source calibration method based on digipots.[63] The calibration routine triggers all the current sources simultaneously, reading the resulting voltages from a calibration load circuit. The values are then optimized for each frequency using the digipots, controlling both the Howland source equilibrium state and the output GICs.[63] Therefore, the system is capable of achieving the best output impedance at the implemented frequencies, reducing current errors, and relaxing software calibrations. Reciprocity errors using this method and further software calibration were less than 1%. Embedding the calibration circuit to the KHU Mark2 system can allow automatic self-calibration before every measurement.[63]

## VII. ELECTRODE CONFIGURATIONS

Electrodes are one of the most fundamental stages in bioimpedance measurements, as they are responsible for the interface between cells and electronics.[24] Electrodes should be optimized in terms of geometry and material, yielding adequate electrical characteristics while providing a biocompatible and stable surface for the cells. In terms of materials, gold is the most popular choice in cell culture bioimpedance due to its inertness.[24,36] Gold electrodes present high biocompatibility and stability, making them suitable for long-term monitoring. Yang *et al.* showed that gold electrodes in contact with cell cultures are stable for long periods of time, with less than 0.4% channel voltage deviation over 8 h.[61] Other noble metals, such as platinum and titanium, have similar properties and were also implemented in cell culture EIT.

The geometry, distribution, and number of electrodes greatly affect the sensitivity matrix, which in turn define the spatial resolution of the EIT setup.[24,25,33] Theoretically, reducing the electrode array size and spacing, as well as increasing electrodes number, improves spatial resolution.[25,33] For instance, Canali *et al.* showed that increasing the electrode number from 8 to 32, the position accuracy was significantly improved,[57] and Lee *et al.* demonstrated that shapes smaller than 300 $\mu$m could be detected if the electrode number was increased from 360 to 2400 and chamber size reduced ten times.[66] However, this approach leads to several drawbacks. Increasing the electrode number reduces the space between electrodes, which in turn decreases the measured signal and, consequently, the SNR.[66,94] For instance, the micro-EIT system proposed by Lee *et al.*, which uses 360 sensing electrodes, presented a decrease of 15 dB in the SNR compared to the conventional 16 channel EIT, using the same electronic platform (KHU Mark 2).[63,66] The small spacing between channels also increases stray capacitances and crosstalk,[65,66] and the same effect should be expected if the chamber size is reduced. In addition, a large number of electrodes leads to large conductive areas at the boundaries of the chamber. This creates a problem called the shunting effect that can passively deform the field distribution and interfere with the measurements.[57,65,95] Another problem caused by the large number of electrodes is the reduction in the contact area, which increases the contact impedance of small electrodes, generating imaging errors. Liu *et al.* demonstrated that both the real and imaginary parts of the contact impedance increase several orders of magnitude in microelectrodes, requiring higher frequencies perform the measurements.[51] Finally, increasing the number of electrodes reduces the frame rate, as the number of measurements in each scan will increase.[57] Therefore, the number of electrodes is highly limited by current technology.

Another way of improving the sensitivity matrix is to optimize the configuration of the electrode array. Different geometrical distributions, combined with adequate measuring protocols, provide higher or lower sensitivity at specific regions of interest. Subsections VII A–VII D present different electrode configurations proposed in the literature for cell culture EIT.

### A. Planar electrodes

Planar electrodes are usually distributed at the bottom of the cell chamber, providing three-dimensional sensitivity and allowing quasi-3D imaging reconstruction.[43,52] However, the sensitivity of the configuration decreases with the height, with maximum sensitivity at the bottom and zero sensitivity after a limit layer.[43,48,52]

Yang *et al.* proposed a miniature EIT electrode configuration consisting of 16 gold plated planar electrodes [Fig. 7(a)], in rectangular shape (1.2 × 0.6 mm$^2$), evenly distributed at the boundary of a circular well (15 mm in diameter).[52] Placing the electrodes at the boundary avoids direct contact with the scaffold, which reduces artifacts caused by contact impedance.[48,49] A circular ground electrode with 0.4 mm of diameter was placed at the center, to reduce DC drift caused by charge motion in the culture media.[52] The substrate was manufactured using a printed circuit board, and the well was made of quartz glass. Driven by the mfEIT system,[58] this configuration achieved maximum spatial sensitivity of 1.14%, which corresponded to 0.8 mm cell spheroids.[43,59] Although the configuration worked well with 2D bottom images, it presents significant limitations in 3D imaging in the vertical direction.[43] The proof of concept for real-time monitoring of drug-response was given, and conductivity images were correctly related to cell mortality.[59] This configuration was applied in both time-difference and frequency-difference EIT of MCF-7 cell spheroids and scaffolds, using 0.75 mA currents at 10 kHz.[43,52]

Yin *et al.* proposed a planar electrode configuration of 16 circular gold-plated electrodes (300 $\mu$m in radius), distributed along two concentric rings placed at the substrate, with a ground electrode in the middle [Fig. 7(b)].[48,49] The manufacturing process was similar to the PCB sensor proposed by Yang *et al.*[52] However, the electrodes were radially distributed through the substrate, therefore being in direct contact with the cell sample. The presence of spike artifacts was reported in the 3D image, resulting from the contact impedance.[48,49] The sensor was applied in breast cancer cell spheroid imaging to monitor the cell-drug response to Triton X-100.[48] TDEIT imaging was used (adjacent protocol, 0.5 mA–10 kHz), and spheroids were correctly reconstructed.[48] Quantitative analysis showed a position error smaller than 0.08 mm, using spheroids with 1.26% of the total volume. In addition, the proof of concept for real-time monitoring during drug-response tests was provided. The authors reported no cell damage due to heat or DC currents in this system.[48]

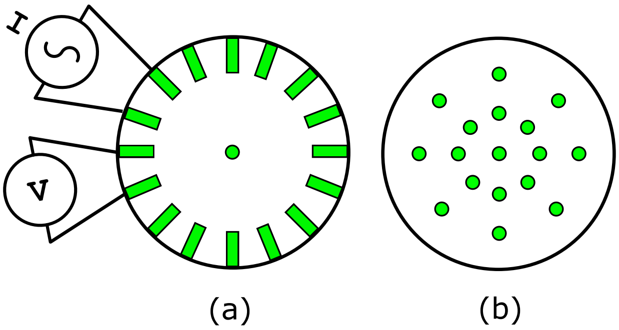

**FIG. 7.** Planar electrode arrays implemented by (a) Yang *et al.*[56] and (b) Yin *et al.*[48] Adapted with permission from Wu *et al.*, Analyst **143**(17), 4189–4198 (2018). Copyright 2018 The Royal Society of Chemistry.

Jamil *et al.* designed a planar array of platinum electrodes distributed in the substrate of a culture chamber.[86] The geometry consisted of 16 circular microelectrodes (250 $\mu$m radius) distributed in a ring, manufactured using photolithography in the glass substrate. A parylene C passivation layer was applied, exposing only the microelectrodes.[86] The work used time-difference EIT (adjacent protocol, 0.75 mA–20 kHz) to image MCF-7 breast cancer cell spheroids (0.71 mm in diameter). They used the mfEIT system designed by the Agile Tomography Group.[58] In addition to providing lower stray capacitance, the transparent glass substrate allowed the use of optical microscopy, which is important for cross-validation experiments.

### B. Cross-sectional electrodes

Cross-sectional electrode arrays are the most common electrode configuration in conventional EIT.[25] It distributes the electrodes in a ring around the biological sample, and it is used to image the cross-sectional plane. Therefore, this configuration is optimized for 2D images. In the cell culture context, the electrodes are usually distributed on the walls of the circular chambers, forming a ring around one of more cross-sectional layers.

Yang presented a cross-sectional electrode configuration, optimized for 2D cross-sectional images of 3D spheroids.[61,62] It used the half hole PCB process to create a ring of cross-sectional gold-plated electrodes. The electrodes faced the cross-sectional layer, maximizing the horizontal sensitivity. The sensing volume is 14 mm in diameter and 1.6 mm in height.[61,62] A glass substrate was fixed below the PCB sensing hole, enabling optical microscopy. The sensor was used to image MFC-7 cancer cells spheroids with excitation currents of 0.75 mA at 10 kHz.[61,62] Significant shape asymmetry was found but attributed to manufacture imperfections.

Another cross-sectional configuration was proposed by Canali *et al.*, consisting of a circular parallel configuration containing 8 gold plated needles (fabricated using thermal evaporation of gold),[4] vertically oriented around a cylindrical chamber with 10 mm in diameter (Fig. 8).[57] A platinum wire electrode was placed at the center of the chamber floor to act as a reference for polar-offset measurements. The chamber was manufactured using poly(methylmethacrylate) and biocompatible epoxy glue. The electrode distribution was designed to maximize the positive sensitivity based on previous studies.[4,93] They connected the electrodes to the multiplexer using crocodile clips.[57] This electrode array was able to detect anomalies down to 1% of the chamber size.[57] However, using a cylindrical geometry, vertical conductivity variations were not detected correctly.

Sun *et al.* implemented a circular array with 16 gold electrodes (area 2.06 mm$^2$) to measure a single cell of *Physarum polycephalum*.[50,96,97] The fabrication was based on PCB manufacturing and gold electroplating. A PDMS sheet with a 6 mm diameter hole was used as the chamber. The sensor was capable of imaging the *Physarum polycephalum* in 2D, with the maximum width and length error of 3.4% using the adjacent protocol.[50] Several noise artifacts were reported in early studies due to the direct contact between

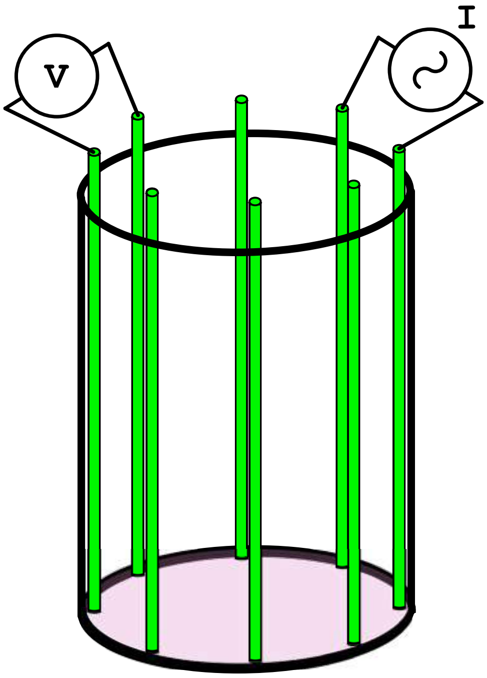

**FIG. 8.** Cross-sectional electrode array implemented by Canali *et al.*[57] Adapted with permission from Canali *et al.*, "Electrical impedance tomography methods for miniaturized 3D systems," J. Electr. Bioimpedance **7**, 59 (2016). Copyright 2016 Author(s), licensed under a Creative Commons Attribution (CC BY-NC-ND 3.0) license.

the electrode and cell, non-uniformity of the electrodes, and other noise sources.[96,97] To avoid the electrode–cell contact, a thin layer of agar was included on top of the electrodes.[50] Based on this configuration, the author estimated that sensors smaller than 30 $\mu$m would be needed to reproduce the single-cell imaging system for human cells.[50]

Meir and Rubinsky proposed a circular array composed of 32 round electrodes at the boundary of a sensing region, to monitor single-cell *Xenopus laevis* oocytes during electroporation.[79] The electrodes were manufactured using vias in PCB technology, and a hole exposed the electrodes to the sensing region. A glass slide and a test tube were glued to the PCB as the substrate and chamber, respectively.[79] The authors studied the effect of the electrode number using simulations, verifying significant improvement from 8 to 16 electrodes, but only marginal improvement from 16 to 32.[79] The SNR of the system was 42 dB, with injection of 0.35 mA at 5 kHz. Although the sensor was designed for oocytes, experimental tests were performed only on glass beads phantoms.[79]

To enhance 3D information about the conductivity distribution, Wu *et al.* proposed a multiplane cross-sectional electrode configuration.[60] The planar electrodes used in previous quasi-3D imaging systems[43,52,59] have limited height sensitivity, losing information above a certain layer depending on the penetration depth. The multiplane configuration was composed of 32 electrodes divided in 2 rings, placed on the walls of a circular chamber (15 mm diameter × 6 mm height). Each electrode was a $0.6 \times 0.8$ mm$^2$ rectangle, and the distance between the electrode rings was 2.5 mm.[60] Simulation results, applying the adjacent protocol, showed that the multiplane loses less than 33% of the maximum sensitivity at the top layers, whereas the conventional planar configuration sensitivity dropped four times.[60]

Rahman *et al.* proposed a ring electrode configuration with 16 gold microelectrode tips (10 $\mu$m) around a circular sensing region with 125 $\mu$m in diameter.[89] Gold was electroplated to fabricate the electrodes, and a glass substrate was used to reduce stray capacitances and enable optical microscopy. Ground rings were placed between electrode pads and around the sensing region, and ground tracks were implemented in parallel to the electrodes tracks, to reduce cross-talking and noise pickup.[89] It did not apply actual EIT but implemented spatial-wise impedance measurements of human umbilical vein endothelial cells (HUVECs) monolayers, using opposite bipolar measurements from 12.5 to 500 kHz.[89] The bipolar measurements showed dominance of contact impedance up to 100 kHz, agreeing with Liu *et al.* estimations for microelectrodes.[51] A similar system was proposed in a following work, but using eight gold microelectrodes ($2500 \times 50$ $\mu$m) and a common counter electrode on top, much larger than the others.[78] This reduced the contribution of the counter electrode impedance, making the system essentially monopolar, similar to ECIS measurements.[36,78] In this system, the deposition, adhesion, spreading, and drug response of OvCa429 cells in monolayers could be detected and monitored, with limited angular spatial information, using mainly the contact impedance variations at low frequencies.[78]

### C. Microelectrode arrays

Microelectrode arrays are the state of the art in electrode manufacturing, providing the smallest sensor sizes in EIT and cell mapping. Although achieving high spatial resolution, the large contact impedance and low SNR are major drawbacks that limit the application range of the technology.

Chai *et al.* proposed an imaging system using microelectrode arrays embedded on a microchip containing the whole impedance measuring circuit.[87,98] It implemented a $4 \times 4$ planar microelectrode (100 $\mu$m$^2$) array, using CMOS processing and the Electroless Gold Plating (EGP) technique to deposit gold. The entire circuit (including multiplexers, instrumentation amplifiers, and excitation source) was integrated on the same chip, creating a standalone micro-sensor for cell imaging.[87,98] Two-dimensional images were taken from cell monolayers, using adjacent protocol and excitation voltage of $100 mV_{rms}$ at 50 kHz.[87] Because the microelectrodes were planar, sensitivity reduces with the height.

Yao *et al.* proposed a microelectrode system to image cross sections of a microchannel used in flow cytometry.[51,99] The configuration consisted of five circular microelectrode arrays distributed equally through the channel, one for each cross section. Each array was composed of 16 multi-layered platinum electrodes, with 10 $\mu$m in thickness and 200 $\mu$m in width.[51,99] The microelectrodes were manufactured using MEMS techniques and photolithography.[80,99] In this setup, images were significantly affected by contact impedance in frequencies lower than 100 kHz, with completely erroneous reconstructions at 10 kHz.[51] Higher frequencies were able to image the cross sections, helping to visualize the sedimentation process in real-time.[51,80,99]

The microelectrode number was pushed to the limit by Viswam *et al.*[75,76] The authors designed a fully integrated and reconfigurable planar array with 59 760 platinum microelectrodes (7.5 × 3.0 $\mu$m each), achieving a spatial resolution of 13.5 $\mu$m with frequencies from 1 Hz to 1 MHz. However, the proposed system was applied in cell mapping rather than EIT, generating 2D maps of brain slices and cardiac cells.[75,76] One major limitation of this setup is the low time resolution due to the number of measurements: each image reconstruction takes up to 2 minutes to complete.[75,76] As EIT is significantly slower and more complex than cell mapping, this density of electrodes may not be feasibly in real-time EIT due to the computational cost. The system implemented voltage excitation in the range of mV without any cell harming.[76] To improve contact impedance, Viswam *et al.* coated the microelectrodes with rough platinum black, reducing the impedance from 2.4MΩ to 107 kΩ at 10 kHz.[76]

### D. Special configurations

Special electrode configurations and geometries can be implemented to solve specific application problems. For instance, Lee *et al.* proposed a microEIT sensor to reduce the effects of contact impedance on current excitation, as well as improving the uniformity of the excitation field.[66] High contact impedance limits the maximum allowed excitation current due to the finite voltage compliance. To reduce the problem, Lee *et al.* designed injection electrodes 15 times larger than the voltage sensing electrodes.[66] This system, based on the previous work by Liu *et al.*[64,65] implemented two opposite electrode arrays, each one composed of a 3 × 3 configuration of coplanar rectangular electrodes (Fig. 9). The gold injection electrodes were placed on the right and left walls of the culture chamber, creating different current patterns that can travel mainly through the x-direction.[66] The front, back, and bottom walls of the chamber were covered by 360 gold voltage sensing electrodes (24 × 15 arrays per wall), with 1 mm in diameter each.

This configuration was able to reduce contact impedance in the current injection path, while keeping high resolution in the voltage sensing path.[66] However, it is limited in terms of current injection protocols and presents an anisotropic sensitivity matrix: higher sensitivity in the x-direction compared to the y and z-directions. The injection protocol implemented in this work is described in Sec. V. This electrode configuration is an upgrade of the electrodes proposed by Liu *et al.*: in the first work, only one large pair of opposite injection electrodes was implemented, allowing one uniform current distribution,[64] and in the second work, a second pair of thin wire injecting electrodes was applied, placed in the front and back walls, to provide y-direction information.[65] The use of 3 × 3 injection electrode arrays instead of the lateral wire electrodes provided a sensitivity increase of 30%, with half the standard deviation.[65,66]

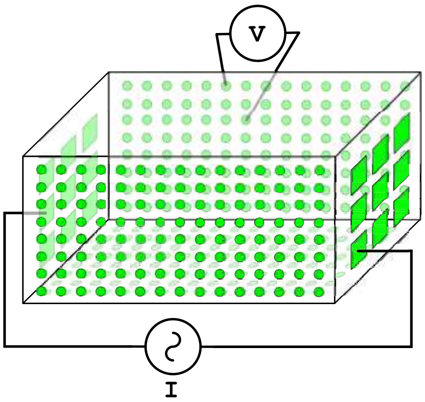

**FIG. 9.** Microscopic EIT sensor proposed by Lee *et al.*[66] The image shows current excitation arrays and highlights the spacing between voltage sensing electrodes. Adapted with permission from Lee *et al.*, "Design of a microscopic electrical impedance tomography system for 3D continuous non-destructive monitoring of tissue culture," BioMed. Eng. OnLine **13**, 142 (2014). Copyright 2014 Aurhor(s), licensed under a Creative Commons Attribution (CC BY 4.0) license.

Another special configuration was proposed by Linderholm *et al.*, to measure vertical cross-sectional images of cell monolayers.[41] In this configuration, 16 long planar electrodes (5 $\mu$m × 4 mm) were distributed in parallel at the bottom of a cell chamber. Different from conventional electrode geometries, this array allowed to sense conductivity gradients only in the orthogonal direction (relative to the electrodes), whereas parallel variations were averaged out.[41] Long electrodes provide higher penetration depth than point electrodes.[24] Using different tetrapolar combinations, the penetration depth could be controlled, and vertical cross-sectional images were reconstructed. Ti/Pt (titanium-platinum) electrodes were manufactured on top of a glass substrate, using photosensitive polyimide (PI 2731) as the passivation layer.[41] The circuit was first tested with human hair phantoms, showing the maximum penetration depth of 100 $\mu$m. Then, the system was used to monitor growth, drug response,[41] and migration[72] of human epithelial stem cell monolayers, with 100 $\mu$m thickness.

## VIII. DISCUSSIONS

Concerning excitation circuits, dedicated excitation stages are mainly implemented using current sources. This is because current sources are able to provide better control of the output current level than voltage sources. However, current sources are more complex to design and have limited high frequency performance due to stray capacitances and finite output impedance.[54,55] In critical cases, voltage sources with current limitation techniques may be applied. Nonetheless, the frequency range implemented in the devices here presented are within the acceptable range of current sources (<1 MHz), justifying its application.

From the current sources reviewed on this paper, the Howland source was the most applied in dedicated micro EIT circuits.[58,63] It offers flexibility and simple design rules, as well as providing stable currents in a wide range of frequencies. The implementation of GICs is a well known technique to increase output impedance; however, it also increases system complexity and requires constant calibration routines.[63] The mfEIT system implemented a Howland Current Source without output GICs, obtaining high quality 2D and 3D images.[52,58,60] Errors resulting from output impedance reduction can be mitigated using the CFDEIT method proposed by Wu *et al.*,[53] which is significantly easier to implement than the GIC circuits.[63] However, most current sources reported here were single-ended. As discussed in Sec. VI, the CMRR of the sensing stage decreases with frequency, and the common-mode voltage generated by a single-ended current source is not optimal, reaching half the amplitude of the signal.[67] Therefore, a symmetrical Howland source should be

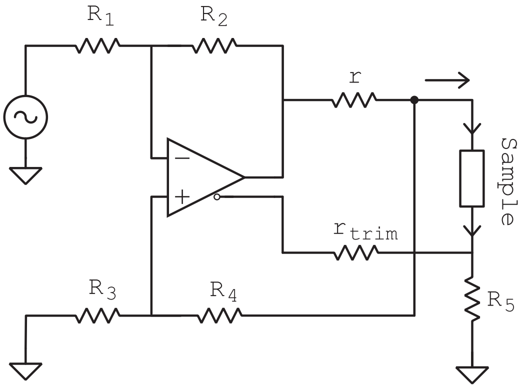

**FIG. 10.** Howland Current Source (MDEHCS) topology implemented with a differential amplifier. Circuit proposed by Sirtoli *et al.*[67] Adapted with permission from Sirtoli *et al.*, "Design of current sources for load common mode optimization," J. Electr. Bioimpedance **9**, 5971 (2018). Copyright 2018 Author(s) licensed under a Creative Commons Attribution (CC BY-NC-ND 3.0) license.

considered for the application, reducing the common-mode voltage at the sensing electrodes. Sirtoli *et al.* proposed the Modified Differential Enhanced Howland Current Source (MDEHCS) topology using a differential amplifier, with almost zero common-mode voltage and stable enough to be used in EIT measurements[67] (Fig. 10). The MDEHCS should be optimized for currents below 1 mA, to avoid cell harming, and frequencies between 10 kHz and 1 MHz. The feedback resistors of the Howland source should be maximized (within the limits of the differential amplifier) to reduce the feedback current. In addition, the value of the resistor *r* should be selected carefully because large resistances can reduce voltage compliance.[100] In addition, to obtain high output impedance, the open-loop gain of the operational amplifier should be high, and the resistor tolerances should be minimized.[69] For binary-signal excitation (such as square waves, pulse-width modulation, and DIBS), the slew rate should also be prioritized, to prevent signal distortion. To measure the current, if needed, shunt resistors are recommended, as conventional single-ended transimpedance amplifiers cannot be implemented with symmetrical current sources.

Although cell-culture EIT devices are not intended for *in vivo* applications, the level of output current should be selected carefully. This is because the small area of microelectrodes can increase the current density significantly, which may result in local heating that harms the cells and change the conductivity.[34] In addition, the large polarization impedance of microelectrodes,[101] combined with finite voltage compliance, further limits the maximum acceptable amplitude. Therefore, the design of excitation circuits should also take into account these limitations.

The voltage sensing basic circuit in most papers consisted of an instrumentation amplifier, a band-pass filter, a programmable gain amplifier (PGA), an analog-to-digital converter (ADC), and a lock-in demodulator. Digital lock-in demodulators using FPGAs are preferable, providing higher flexibility and stability than the analog counterparts, while maintaining the speed of hardware operation.[24] This circuit scheme yielded effective results in most circuits presented in the literature. Therefore, this review recommends the use of a similar structure. The PGA stage can be designed using either digipots or ready-to-use commercial PGAs with wide gain ranges, and the instrumentation amplifier selection should prioritize high bandwidth, high CMRR, high input resistance, and low input capacitances, as leakage currents are the major error sources in FDEIT.[53]

To reduce noise, stray capacitances, and leakage currents, the voltage-driven triaxial shielding, shown in Fig. 6, is recommended.[63] However, triaxial cables are typically bulky, which may not be suitable for very small sensors with large numbers of electrodes. In addition, the OPAMP buffers may reduce the final bandwidth of the system due to stability limitations in high frequencies. Micro-coaxial cables may be an alternative, but they introduce large stray capacitances that degrade the high frequency performance. GIC circuits can be used to compensate these capacitances at the cost of complexity. If allowed in the application, cables can be eliminated by directly connecting, via PCB, the analog front-end to the sensor. In these cases, the path length between circuit and electrodes should be minimized and matched, and shielding should be provided through ground and power planes. Differential signaling can also improve the SNR significantly.

Although parallel configuration provides the best channel switching performance,[63] the increase in hardware complexity is not beneficial for most systems using more than 16 electrodes. However, the use of arbitrary measurement protocols is desirable in cell culture EIT, as conductivity changes are very small and can occur at different regions of the chamber: for instance, the adjacent protocol can be used to measure the boundary region, while opposite measurements can better measure the center. Therefore, a switching scheme similar to the one designed by Yang and Jia[58] is a good choice. As recommended in the article, cascade cross-point and simple single-pole/single-throw (SPST) switches should be used for voltage and current commutation. However, multiplexers can also be implemented without significant penalization, if properly selected. The selection of switching components should prioritize low stray capacitances, low channel resistance, and fast settling time. If the desired measurement protocol is fixed, the number of switches should be minimized to reduce parasitic capacitances. In addition, multiplexers and switches should be selected according to the required frame rate. The frame rate of a cell-culture EIT system must be enough to capture the dynamics of the application. In addition, averaging samples to reduce noise will increase the required frame rate. Therefore, the minimum number of frames-per-second is application dependent and should be defined prior to circuit design.

Both TDEIT and FDEIT are important in cell culture EIT, as the first provides a transient analysis of cell experiments and the second allows long term monitoring of cultures. Therefore, multi-frequency operation is required. However, the generation of sinusoidal signals demands fast digital-to-analog signal converters. An easier way of implementing different frequencies is by using discrete interval binary sequence (DIBS).[81] DIBS are optimized binary signals composed of simultaneous harmonics. Because the signal is binary, different frequencies can be generated using a single digital I/O, eliminating the DAC stage. Therefore, this review recommends the exploration of DIBS as a broadband signal alternative for fast EIT imaging in cell-cultures. The technique should still be compatible with parallel lock-in approaches and other fast signal processing techniques and may improve significantly the frame rate of future devices. However, the designer should carefully consider some drawbacks of binary and broadband signals: digital signals require operational amplifiers with high slew rate in the excitation circuit, to avoid distortion of the square wave and introduction of unwanted harmonics. In addition, because broadband signal excitation introduces losses in accuracy and impedance sensitivity,[81] the imaging degradation may be too critical to justify the increase in speed.

The electrode configuration of an EIT system is usually application dependent, as discussed in Sec. VII. Therefore, it is difficult to select a general array geometry for cell cultures. However, because cell modeling and tissue engineering research are currently focusing on three-dimensional structures (due to the improved biological behavior[12]), electrode configuration should be designed to optimize 3D EIT. From the analyzed electrode arrays, the planar circular structure and the multiplane cross-sectional arrays proposed by Yang *et al.* and Wu *et al.*, respectively, presented the best potential for general 3D imaging of scaffolds.[52,60]

It is important to highlight that the gold plating process of electrodes must be biocompatible, and this includes other materials presented in the process. For instance, the selection of the intermediate layer material plays an important role in corrosion and biocompatibility: e.g., nickel is more cytotoxic for cells than bronze.[102] In terms of geometry, the multiplanar scheme is better for quasi-3D imaging, but it is not compatible with the simple PCB process, which in turn complicates manufacturing.[60] The electrode number can be based on the study performed by Meir and Rubinsky.[79] Some applications using small cell constructs may require sensor size reduction. In these cases, electrode surface coating using platinum black or conductive polymers is recommended for contact impedance reduction.[73,76]

A major consensus of the reviewed papers was that the main limitation of EIT systems is spatial resolution, which is mainly constrained by the number of electrodes. Moreover, spatial resolution is not uniform, decreasing from the borders to the center of the sample volume.[84] Several alternative electrical imaging techniques were proposed in the literature to improve spatial resolution, such as Magnetic Resonance EIT (MREIT), Magnetic Induction Tomography (MIT), and Scanning Impedance Imaging (SII).[22,25,103–105] However, compared to EIT, those techniques require a significant increase in the hardware cost, complexity, and size: MREIT needs a magnetic resonance machine and high current levels (in the order of 15 mA), MIT uses several bulky coils and SII needs a three-axial positioning system to control the probe. In addition, MIT presents low signal sensitivity and SII lacks temporal resolution due to motion and computational complexity.[22,25,104,105] Therefore, EIT still remains as the electrical technique with the best potential for real-time and spatial-wise conductivity measurements in cell cultures.

## IX. CONCLUSION

Electrical Impedance Tomography (EIT) is a non-invasive imaging technique with high potential for cell culture monitoring applications due to its high temporal resolution, biocompatibility, compact hardware, automatic operation, and high throughput. However, cell culture EIT presents particularities and challenges that should be considered when designing the system hardware. This paper reviews several analog front-end designs, all applied to cell culture imaging and characterization, analyzing the main components of the general system: excitation circuit, voltage/current sensing circuit, switching stage, signal specifications, and electrode configurations. It also reviews measurement protocols and calibration strategies. Finally, the different approaches were qualitatively compared and design guidelines were proposed in order to facilitate the design of future circuits. We hope that this review facilitates and improves the design of novel EIT devices and the scientific research in the field.

## ACKNOWLEDGMENTS

We thank the University of the State of Santa Catarina (UDESC) and the *Fundação de Amparo à Pesquisa e Inovação do Estado de Santa Catarina* (FAPESC) for funding and supporting this research (Grant Reference No. 2019TR652).

## AUTHOR DECLARATIONS

### Conflict of Interest

The authors have no conflicts to disclose.

### Author Contributions

All authors contributed equally to this work.

## DATA AVAILABLITY

Data sharing is not applicable to this article as no new data were created or analyzed in this study.

## REFERENCES

[1] R. I. Freshney, *Culture of Animal Cells* (John Wiley & Sons, 2005).

[2] M. S. Kallos, A. Sen, and L. A. Behie, "Large-scale expansion of mammalian neural stem cells: A review," Med. Biol. Eng. Comput. **41**, 271–282 (2003).

[3] C. D. Helgason and C. L. Miller, *Basic Cell Culture Protocols* (Springer, 2005), Vol. 1.

[4] C. Canali, A. Heiskanen, H. B. Muhammad, P. Høyum, F.-J. Pettersen, M. Hemmingsen, A. Wolff, M. Dufva, Ø. G. Martinsen, and J. Emnéus, "Bioimpedance monitoring of 3D cell culturing—Complementary electrode configurations for enhanced spatial sensitivity," Biosens. Bioelectron. **63**, 72–79 (2015).

[5] J. W. Haycock, "3D cell culture: A review of current approaches and techniques," in *3D Cell Culture* (Springer, 2011), pp. 1–15.

[6] E. M. Darling and K. A. Athanasiou, "Articular cartilage bioreactors and bioprocesses," Tissue Eng. **9**, 9–26 (2003).

[7] Y. Jimbo and A. Kawana, "Electrical stimulation and recording from cultured neurons using a planar electrode array," Bioelectrochem. Bioenerg. **29**, 193–204 (1992).

[8] R. P. Haugland, I. C. MacCoubrey, and P. L. Moore, "Dual-fluorescence cell viability assay using ethidium homodimer and calcein AM," U.S. patent US5314805 (24 May 1994).

[9] M. Absher, "Hemocytometer counting," in *Tissue Culture* (Elsevier, 1973), pp. 395–397.

[10] I. B. Buchwalow and W. Böcker, "Immunohistochemistry," Basics Methods **1**, 1–149 (2010).

[11] T. L. Riss, R. A. Moravec, A. L. Niles, S. Duellman, H. A. Benink, T. J. Worzella, and L. Minor, "Cell viability assays," in *Assay Guidance Manual [Internet]* (Eli Lilly & Company and The National Center for Advancing Translational Sciences, 2016).

[12] F. Pampaloni, E. G. Reynaud, and E. H. K. Stelzer, "The third dimension bridges the gap between cell culture and live tissue," Nat. Rev. Mol. Cell Biol. **8**, 839–845 (2007).

[13] L. E. Smith, R. Smallwood, and S. Macneil, "A comparison of imaging methodologies for 3D tissue engineering," Microsc. Res. Tech. **73**, 1123–1133 (2010).

[14] R. Edmondson, J. J. Broglie, A. F. Adcock, and L. Yang, "Three-dimensional cell culture systems and their applications in drug discovery and cell-based biosensors," Assay Drug Dev. Technol. **12**, 207–218 (2014).

[15] G. Tiscornia, E. L. Vivas, and J. C. I. Belmonte, "Diseases in a dish: Modeling human genetic disorders using induced pluripotent cells," Nat. Med. **17**, 1570–1576 (2011).

[16] T. Woodfield, K. Lim, P. Morouço, R. Levato, J. Malda, and F. Melchels, "Biofabrication in tissue engineering," Compr. Biomater. II **5**, 236–266 (2017).

[17] W. Gamal, H. Wu, I. Underwood, J. Jia, S. Smith, and P. O. Bagnaninchi, "Impedance-based cellular assays for regenerative medicine," Philos. Trans. R. Soc., B **373**, 20170226 (2018).

[18] A. Poghossian, S. Ingebrandt, A. Offenhäusser, and M. J. Schöning, "Field-effect devices for detecting cellular signals," in *Seminars in Cell and Developmental Biology* (Elsevier, 2009), Vol. 20, pp. 41–48.

[19] V. F. Curto, B. Marchiori, A. Hama, A.-M. Pappa, M. P. Ferro, M. Braendlein, J. Rivnay, M. Fiocchi, G. G. Malliaras, M. Ramuz *et al.*, "Organic transistor platform with integrated microfluidics for in-line multi-parametric *in vitro* cell monitoring," Microsyst. Nanoeng. **3**, 17028 (2017).

[20] S. E. De León, A. Pupovac, and S. L. McArthur, "Three-dimensional (3D) cell culture monitoring: Opportunities and challenges for impedance spectroscopy," Biotechnol. Bioeng. **117**, 1230–1240 (2020).

[21] L. Udpa, V. M. Ayres, Y. Fan, Q. Chen, and S. A. Kumar, "Deconvolution of atomic force microscopy data for cellular and molecular imaging," IEEE Signal Process. Mag. **23**, 73–83 (2006).

[22] H. Liu, "A high-resolution microscopic electrical impedance imaging modality: Scanning impedance imaging," Ph.D. thesis Brigham Young University Repository, 2007.

[23] D. Holder, *Electrical Impedance Tomography: Methods, History and Applications* (CRC Press, 2004).

[24] O. G. Martinsen and S. Grimnes, *Bioimpedance and Bioelectricity Basics* (Academic Press, 2011).

[25] R. H. Bayford, "Bioimpedance tomography (electrical impedance tomography)," Annu. Rev. Biomed. Eng. **8**, 63–91 (2006).

[26] Q. Wang, J. Polansky, B. Karki, M. Wang, K. Wei, C. Qiu, A. Kenbar, and D. Millington, "Experimental tomographic methods for analysing flow dynamics of gas-oil-water flows in horizontal pipeline," J. Hydrodyn. **28**, 1018–1021 (2016).

[27] M. Hallaji, A. Seppänen, and M. Pour-Ghaz, "Electrical impedance tomography-based sensing skin for quantitative imaging of damage in concrete," Smart Mater. Struct. **23**, 085001 (2014).

[28] K. Y. Aristovich, B. C. Packham, H. Koo, G. S. dos Santos, A. McEvoy, and D. S. Holder, "Imaging fast electrical activity in the brain with electrical impedance tomography," NeuroImage **124**, 204–213 (2016).

[29] S. Pulletz, M. Kott, G. Elke, D. Schädler, B. Vogt, N. Weiler, and I. Frerichs, "Dynamics of regional lung aeration determined by electrical impedance tomography in patients with acute respiratory distress syndrome," Multidiscip. Respir. Med. **7**, 44 (2012).

[30] J. K. Seo, J. Lee, S. W. Kim, H. Zribi, and E. J. Woo, "Frequency-difference electrical impedance tomography (fdEIT): Algorithm development and feasibility study," Physiol. Meas. **29**, 929 (2008).

[31] J. L. Mueller, S. Siltanen, and D. Isaacson, "A direct reconstruction algorithm for electrical impedance tomography," IEEE Trans. Med. Imaging **21**, 555–559 (2002).

[32] B. Jin, T. Khan, and P. Maass, "A reconstruction algorithm for electrical impedance tomography based on sparsity regularization," Int. J. Numer. Methods Eng. **89**, 337–353 (2012).

[33] W. R. B. Lionheart, "EIT reconstruction algorithms: Pitfalls, challenges and recent developments," Physiol. Meas. **25**, 125 (2004).

[34] H. Griffiths, M. G. Tucker, J. Sage, and W. G. Herrenden-Harker, "An electrical impedance tomography microscope," Physiol. Meas. **17**, A15 (1996).

[35] T. York, L. Sun, C. Gregory, and J. Hatfield, "Silicon-based miniature sensor for electrical tomography," Sens. Actuators, A **110**, 213–218 (2004).

[36] I. Giaever and C. R. Keese, "Use of electric fields to monitor the dynamical aspect of cell behavior in tissue culture," IEEE Trans. Biomed. Eng. **33**, 242–247 (1986).

[37] C. Xiao and J. H. T. Luong, "On-line monitoring of cell growth and cytotoxicity using electric cell-substrate impedance sensing (ECIS)," Biotechnol. Prog. **19**, 1000–1005 (2003).

[38] R. Szulcek, H. J. Bogaard, and G. P. van Nieuw Amerongen, "Electric cell-substrate impedance sensing for the quantification of endothelial proliferation, barrier function, and motility," J. Visualized Exp. **85**, e51300 (2014).

[39] M. Angstmann, I. Brinkmann, K. Bieback, D. Breitkreutz, and C. Maercker, "Monitoring human mesenchymal stromal cell differentiation by electrochemical impedance sensing," Cytotherapy **13**, 1074–1089 (2011).

[40] F. A. Alexander, D. T. Price, and S. Bhansali, "From cellular cultures to cellular spheroids: Is impedance spectroscopy a viable tool for monitoring multicellular spheroid (MCS) drug models?," IEEE Rev. Biomed. Eng. **6**, 63–76 (2012).

[41] P. Linderholm, L. Marescot, M. H. Loke, and P. Renaud, "Cell culture imaging using microimpedance tomography," IEEE Trans. Biomed. Eng. **55**, 138–146 (2007).

[42] P. Bertemes-Filho, "Medical physics," Ph.D. thesis, University of Sheffield Repository, Sheffield, 2002.

[43] H. Wu, "Electrical impedance tomography for real-time 3D tissue culture monitoring," Ph.D. thesis Edinburgh Research Archive, 2020.

[44] B. Brown, "Electrical impedance tomography (EIT): A review," J. Med. Eng. Technol. **27**, 97–108 (2003).

[45] X. Yue and C. McLeod, "FPGA design and implementation for EIT data acquisition," Physiol. Meas. **29**, 1233 (2008).

[46] D. Jennings and I. D. Schneider, "Front-end architecture for a multifrequency electrical impedance tomography system," Med. Biol. Eng. Comput. **39**, 368–374 (2001).

[47] M. Takhti, Y.-C. Teng, and K. Odame, "A high frequency, high frame rate front end for electrical impedance tomography," in *2017 IEEE Biomedical Circuits and Systems Conference (BioCAS)* (IEEE, 2017), pp. 1–4.

[48] X. Yin, H. Wu, J. Jia, and Y. Yang, "A micro EIT sensor for real-time and non-destructive 3-D cultivated cell imaging," IEEE Sens. J. **18**, 5402–5412 (2018).

[49] X. Yin, Y. Yang, J. Jia, and C. Tan, "3D image reconstruction on a miniature planar EIT sensor using sparsity with median filter," in *2017 IEEE Sensors* (IEEE, 2017), pp. 1–3.

[50] T. Sun, S. Tsuda, K.-P. Zauner, and H. Morgan, "On-chip electrical impedance tomography for imaging biological cells," Biosens. Bioelectron. **25**, 1109–1115 (2010).

[51] X. Liu, J. Yao, T. Zhao, H. Obara, Y. Cui, and M. Takei, "Image reconstruction under contact impedance effect in micro electrical impedance tomography sensors," IEEE Trans. Biomed. Circuits Syst. **12**, 623–631 (2018).

[52] Y. Yang, J. Jia, S. Smith, N. Jamil, W. Gamal, and P.-O. Bagnaninchi, "A miniature electrical impedance tomography sensor and 3-D image reconstruction for cell imaging," IEEE Sens. J. **17**, 514–523 (2016).

[53] H. Wu, Y. Yang, P.-O. Bagnaninchi, and J. Jia, "Calibrated frequency-difference electrical impedance tomography for 3D tissue culture monitoring," IEEE Sens. J. **19**, 7813–7821 (2019).

[54] W. Sansen, B. Geeraerts, W. Van Petegem, W. Dehaene, and M. Steyaert, "Voltage versus current driven high frequency EIT systems," in *Proceedings of the 1992 International Biomedical Engineering Days* (IEEE, 1992), pp. 102–106.

[55] Y. Mohamadou, T. I. Oh, H. Wi, H. Sohal, A. Farooq, E. J. Woo, and A. L. McEwan, "Performance evaluation of wideband bio-impedance spectroscopy using constant voltage source and constant current source," Meas. Sci. Technol. **23**, 105703 (2012).

[56] M. H. Choi, T.-J. Kao, D. Isaacson, G. J. Saulnier, and J. C. Newell, "An algorithm for applying multiple currents using voltage sources in electrical impedance tomography," Int. J. Control Autom. Syst. **6**, 613 (2008).

[57] C. Canali, K. Aristovich, L. Ceccarelli, L. B. Larsen, Ø. G. Martinsen, A. Wolff, M. Dufva, J. Emnéus, and A. Heiskanen, "Electrical impedance tomography methods for miniaturised 3D systems," J. Electr. Bioimpedance **7**, 59–67 (2016).

[58] Y. Yang and J. Jia, "A multi-frequency electrical impedance tomography system for real-time 2D and 3D imaging," Rev. Sci. Instrum. **88**, 085110 (2017).

[59] H. Wu, Y. Yang, P. O. Bagnaninchi, and J. Jia, "Electrical impedance tomography for real-time and label-free cellular viability assays of 3D tumour spheroids," Analyst **143**, 4189–4198 (2018).

[60] H. Wu, Y. Yang, S. Liu, P. O. Bagnaninchi, and J. Jia, "Multi-plane electrode configuration for 3D cellular assay of electrical impedance tomography," in Electrical Impedance Tomography 19, 2018.

[61] Y. Yang, "Advanced digital electrical impedance tomography system for biomedical imaging," Ph.D. thesis, Edinburgh Research Archive, 2018.

[62] Y. Yang, H. Wu, and J. Jia, "Quasi-2D EIT-optical dual modality sensor for cellular imaging," in *Electrical Impedance Tomography* (Zenodo, 2018), p. 47.

[63] T. I. Oh, H. Wi, D. Y. Kim, P. J. Yoo, and E. J. Woo, "A fully parallel multi-frequency EIT system with flexible electrode configuration: KHU Mark2," Physiol. Meas. **32**, 835 (2011).

[64] Q. Liu, H. Wi, T. I. Oh, E. J. Woo, and J. K. Seo, "Development of a prototype micro-EIT system using three sets of 15 × 8 array electrodes," J. Phys.: Conf. Ser. **224**, 012161 (2010).

[65] Q. Liu, T. I. Oh, H. Wi, E. J. Lee, J. K. Seo, and E. J. Woo, "Design of a microscopic electrical impedance tomography system using two current injections," Physiol. Meas. **32**, 1505 (2011).

[66] E. J. Lee, H. Wi, A. L. McEwan, A. Farooq, H. Sohal, E. J. Woo, J. K. Seo, and T. I. Oh, "Design of a microscopic electrical impedance tomography system for 3D continuous non-destructive monitoring of tissue culture," Biomed. Eng. OnLine **13**, 142 (2014).

[67] V. G. Sirtoli, K. F. Morcelles, and V. C. Vincence, "Design of current sources for load common mode optimization," J. Electr. Bioimpedance **9**, 59–71 (2018).

[68] A. S. Ross, G. J. Saulnier, J. C. Newell, and D. Isaacson, "Current source design for electrical impedance tomography," Physiol. Meas. **24**, 509 (2003).

[69] A. S. Tucker, R. M. Fox, and R. J. Sadleir, "Biocompatible, high precision, wideband, improved Howland current source with lead-lag compensation," IEEE Trans. Biomed. Circuits Syst. **7**, 63–70 (2012).

[70] S. Hong, K. Lee, U. Ha, H. Kim, Y. Lee, Y. Kim, and H.-J. Yoo, "A 4.9 m$\omega$-sensitivity mobile electrical impedance tomography IC for early breast-cancer detection system," IEEE J. Solid-State Circuits **50**, 245–257 (2014).

[71] Y. Wu, D. Jiang, A. Bardill, S. De Gelidi, R. Bayford, and A. Demosthenous, "A high frame rate wearable EIT system using active electrode ASICS for lung respiration and heart rate monitoring," IEEE Trans. Circuits Syst. I: Regular Papers **65**, 3810–3820 (2018).

[72] P. Linderholm, T. Braschler, J. Vannod, Y. Barrandon, M. Brouard, and P. Renaud, "Two-dimensional impedance imaging of cell migration and epithelial stratification," Lab Chip **6**, 1155–1162 (2006).

[73] S. Dharia, H. E. Ayliffe, and R. D. Rabbitt, "Single cell electric impedance topography: Mapping membrane capacitance," Lab Chip **9**, 3370–3377 (2009).

[74] A. Manickam, A. Chevalier, M. McDermott, A. D. Ellington, and A. Hassibi, "A CMOS electrochemical impedance spectroscopy (EIS) biosensor array," IEEE Trans. Biomed. Circuits Syst. **4**, 379–390 (2010).

[75] V. Viswam, R. Bounik, A. Shadmani, J. Dragas, M. Obien, J. Müller, Y. Chen, and A. Hierlemann, "High-density mapping of brain slices using a large multi-functional high-density CMOS microelectrode array system," in *2017 19th International Conference on Solid-State Sensors, Actuators and Microsystems (TRANSDUCERS)* (IEEE, 2017), pp. 135–138.

[76] V. Viswam, R. Bounik, A. Shadmani, J. Dragas, C. Urwyler, J. A. Boos, M. E. J. Obien, J. Müller, Y. Chen, and A. Hierlemann, "Impedance spectroscopy and electrophysiological imaging of cells with a high-density CMOS microelectrode array system," IEEE Trans. Biomed. Circuits Syst. **12**, 1356–1368 (2018).

[77] T. Chi, J. S. Park, J. C. Butts, T. A. Hookway, A. Su, C. Zhu, M. P. Styczynski, T. C. McDevitt, and H. Wang, "A multi-modality CMOS sensor array for cell-based assay and drug screening," IEEE Trans. Biomed. Circuits Syst. **9**, 801–814 (2015).

[78] A. R. A. Rahman, J. Register, G. Vuppala, and S. Bhansali, "Cell culture monitoring by impedance mapping using a multielectrode scanning impedance spectroscopy system (CellMap)," Physiol. Meas. **29**, S227 (2008).

[79] A. Meir and B. Rubinsky, "Electrical impedance tomographic imaging of a single cell electroporation," Biomed. Microdevices **16**, 427–437 (2014).

[80] J. Yao, H. Obara, A. Sapkota, and M. Takei, "Development of three-dimensional integrated microchannel-electrode system to understand the particles' movement with electrokinetics," Biomicrofluidics **10**, 024105 (2016).

[81] B. Sanchez, G. Vandersteen, R. Bragos, and J. Schoukens, "Basics of broadband impedance spectroscopy measurements using periodic excitations," Meas. Sci. Technol. **23**, 105501 (2012).

[82] F. Caselli, P. Bisegna, and F. Maceri, "EIT-inspired microfluidic cytometer for single-cell dielectric spectroscopy," J. Microelectromech. Syst. **19**, 1029–1040 (2010).

[83] S. Gawad, K. Cheung, U. Seger, A. Bertsch, and P. Renaud, "Dielectric spectroscopy in a micromachined flow cytometer: Theoretical and practical considerations," Lab Chip **4**, 241–251 (2004).

[84] J. G. Webster, *English Electrical Impedance Tomography* (Hilger, Bristol, 1990), man. Diagnosis. Tomography (BNB/PRECIS).

[85] D. G. Gisser, D. Isaacson, and J. C. Newell, "Theory and performance of an adaptive current tomography system," Clin. Phys. Physiol. Meas. **9**, 35 (1988).

[86] N. Jamil, S. Smith, Y. Yang, J. Jia, P. Bagnaninchi, and E. González-Fernández, "Design and fabrication of microelectrodes for electrical impedance tomography of cell spheroids," in *2016 IEEE EMBS Conference on Biomedical Engineering and Sciences (IECBES)* (IEEE, 2016), pp. 426–431.

[87] K. Chai, J. Davies, and D. Cumming, "Electrical impedance tomography for sensing with integrated microelectrodes on a CMOS microchip," Sens. Actuators, B **127**, 97–101 (2007).

[88] B. H. Brown and A. D. Seagar, "The Sheffield data collection system," Clin. Phys. Physiol. Meas. **8**, 91 (1987).

[89] A. R. A. Rahman, C.-M. Lo, and S. Bhansali, "A micro-electrode array biosensor for impedance spectroscopy of human umbilical vein endothelial cells," Sens. Actuators, B **118**, 115–120 (2006).

[90] R. D. Cook, G. J. Saulnier, D. G. Gisser, J. C. Goble, J. C. Newell, and D. Isaacson, "ACT3: A high-speed, high-precision electrical impedance tomograph," IEEE Trans. Biomed. Eng. **41**, 713–722 (1994).

[91] D. Isaacson, "Distinguishability of conductivities by electric current computed tomography," IEEE Trans. Med. Imaging **5**, 91–95 (1986).

[92] M. Cheney and D. Isaacson, "Distinguishability in impedance imaging," IEEE Trans. Biomed. Eng. **39**, 852–860 (1992).

[93] C. Canali, C. Mazzoni, L. B. Larsen, A. Heiskanen, Ø. G. Martinsen, A. Wolff, M. Dufva, and J. Emnéus, "An impedance method for spatial sensing of 3D cell constructs–towards applications in tissue engineering," Analyst **140**, 6079–6088 (2015).

[94] J. K. Seo and E. J. Woo, *Nonlinear Inverse Problems in Imaging* (John Wiley & Sons, 2012).

[95] E. Somersalo, M. Cheney, and D. Isaacson, "Existence and uniqueness for electrode models for electric current computed tomography," SIAM J. Appl. Math. **52**, 1023–1040 (1992).

[96] T. Sun, S. Tsuda, N. G. Green, K. P. Zauner, and H. Morgan, "On-chip electrical impedance tomography for monitoring the kinetics in the cell culture," in *12th International Conference on Miniaturized Systems for Chemistry and Life Sciences - The Proceedings of MicroTAS 2008 Conference* (Royal Society of Chemistry, 2008), pp. 973–975.

[97] T. Sun, S. Tsuda, K.-P. Zauner, and H. Morgan, "Single cell imaging using electrical impedance tomography," in *2009 4th IEEE International Conference on Nano/Micro Engineered and Molecular Systems* (IEEE, 2009), pp. 858–863.

[98] K. T. C. Chai, P. A. Hammond, and D. R. S. Cumming, "Modification of a CMOS microelectrode array for a bioimpedance imaging system," Sens. Actuators, B **111**, 305–309 (2005).

[99] J. Yao, H. Obara, M. Sugawara, and M. Takei, "Development of micro electrical impedance tomography system for cell distribution visualization in electrode-multilayered microchannel," in *8th World Congress on Industrial Process Tomography* (IPT, 2016), pp. 350–353.

[100] K. F. Morcelles, V. G. Sirtoli, P. Bertemes-Filho, and V. C. Vincence, "Howland current source for high impedance load applications," Rev. Sci. Instrum. **88**, 114705 (2017).

[101] A. Abdurrahman, D. Price, and S. Bhansali, "Effect of electrode geometry on the impedance evaluation of tissue and cell culture," Sens. Actuators, B **127**, 89–96 (2007).

[102] W. A. T. dos Santos, S. L. Assis, S. O. Rogero, M. Terada, and I. Costa, "Evaluation of corrosion resistance and cytotoxicity of electrodeposited gold on various types of intermediate layers," Surf. Eng. **28**, 108–112 (2012).

[103] M. Schwarz, M. Jendrusch, and I. Constantinou, "Spatially resolved electrical impedance methods for cell and particle characterization," Electrophoresis **41**, 65–80 (2020).

[104] B. Lee, S. Oh, T.-S. Kim, E. Woo, S. Lee, O. Kwon, and J. Seo, "Magnetic resonance electrical impedance tomography of the breast: A simulation study on basic imaging setup," in *2005 IEEE Engineering in Medicine and Biology 27th Annual Conference* (IEEE, 2006), pp. 4377–4380.

[105] H. Scharfetter, R. Merwa, and K. Pilz, "A new type of gradiometer for the receiving circuit of magnetic induction tomography (MIT)," Physiol. Meas. **26**, S307 (2005).